UNIVERSITÀ DEGLI STUDI DI PADOVA
DIPARTIMENTO DI INGEGNERIA INDUSTRIALE
CORSO DI LAUREA MAGISTRALE IN INGEGNERIA AEROSPAZIALE

**Tesi di Laurea Magistrale in**
**Ingegneria Aerospaziale**

# DEVELOPMENT OF AN UNSTEADY BOUNDARY-LAYER METHOD

***Relatore:*** **Prof. Enresto Benini**
***Correlatore:*** **Ing. Dominik Schicker**

***Laureando:*** **ENRICO PANDIN**

ANNO ACCADEMICO 2014/2015

# Abstract

The development of an unsteady boundary-layer method by using a finite difference scheme is presented. The Falkner-Skan transformation is adopted to simplify the computational process and the Cebeci-Smith zero equations model is implemented for turbulent regime. The Keller box scheme has been used and the Flügge-Lotz approximation is adopted for the steady flow. Steady code results are used as starting conditions for the unsteady simulations and a quasi-steady approach is applied for the starting conditions near the leading edge stagnation point. A low-pass filtering function is applied to eliminate numerical instability near the wall. Boundary-layer thickness, displacement thickness, velocity profiles through the boundary-layer and drag coefficient at no angle of attack are calculated. Comparisons between this method, reliable analytical models for flat plates, CFD simulations and experimental results for steady and unsteady flow along aerodynamic profiles show quite good agreement.

# Contents

# Introduction

Capability to predict boundary-layer behavior and, eventually, boundary-layer separation is of fundamental importance when talking about aerodynamical design and performance prediction of helicopters rotor blades, aircraft wings and every other kind of airfoil. Boundary-layer thickness affects viscous drag and, consequently, fuel consumption, while its separation triggers the profile aerodynamic stall.

Nowadays the only way to obtain good results in this field is to perform sophisticated CFD simulations. Unfortunately they need big computational powers and they are very time consuming. If these issues are not a big deal for research purposes, they become a real problem when talking about industrial needings, such as preliminary design analysis. In this context, in fact, it's necessary to have a quick and reliable instrument in order to know as soon as possible which is the best among different choices.

In order to realize a computational tool having the characteristics previously highlightened, viscous/inviscid interaction methods developed during the '70s and '80s[5, 6] seem to be a good starting point. In this kind of methods an "external" inviscid solution (computed by, for example, a panel code) provides the pressure distribution over the airfoil, which is used to calculate the boundary-layer. Once the boundary-layer and its thickness have been calculated the displacement effect of viscous layers is taken into account for a new, improved inviscid calculation. This cycle is repeated until convergence is reached. The computational advantages of this approach are that, on one hand, inviscid solution is carried out with very quick and practical methods. On the other hand, for what concerns the viscous part only the boundary-layer equations have to be solved, which are a reduced Navier-Stokes equations, resulting in considerable savings of computing time.

The following work will outline a numerical unsteady, laminar and turbulent boundary-layer method that, in future developments, will be coupled with an inviscid flow solver. This represent the first attempt to make a numerical instrument to predict viscous behaviors suitable for preliminary design analysis.

At first a theoretical introduction to boundary-layer is provided in Chapter 1. Here all its characteristics (such as its different thicknesses) are defined, boundary-layer equations are derived and some basic concepts of fluid dynamics, such as difference between laminar ant turbulent flow, are recalled. There's also the numerical explanation of how to implement some basic but reliable boundary-layer analytical models, such as the one provided by Pohlhausen for the laminar flow over a flat plate[1]. In the first chapter some numerical issues are described too, like the turbulence model and the variables transformation adopted for the boundary-layer method discussed here.

In Chapter 2 we have the actual numerical formulation of the present method: how the computational grid is defined and how the boundary-layer equations are discretized and solved, at first for steady and then for unsteady flows.

In the end results obtained by the boundary-layer method discussed in this work are compared with those calculated by reliable analytical models, CFD simulations and some experimental data in Chapter 3. The first simulations are carried out for flow over a flat plate, for both completely laminar and turbulent flow, and are compared with the two different analytical models explained in Chaper 1. Then a steady simulation of a NLF-0416 profile has been runned, values of velocity external to the boundary-layer are used as input for the present method, and the results compared. Then the same procedure has been applied to the unsteady simulation of a NACA-0012 profile performing a pitching motion. Experimental data are used to validate drag prediction capability of the present method and understand if its results are better or worse than those obtained by CFD simulations.

# Chapter 1

# Boundary-Layer Methods

The first theoretical investigations about fluid dynamics were based on the assumption of perfect fluids. Perfect fluids are considered to be incompressible and frictionless, so that two contacting layers experience no tangential forces (shear stresses) but act on each other with normal forces (pressures) only. Perfect fluids theory is mathematically very far developed and it brought to very good results in the study of important phenomena such as the motion of surface waves or the formation of liquid jets in air. On the other hand, this theoretical assumption brings to some paradoxes when we want to take into account the drag of a body. In this connexion it leads to the statement that a body which moves uniformly through a fluid which extends to infinity experiences no drag (d'Alembert's paradox).

The origin of these problems is the assumption of no shearing stress transmission through contacting layers, which in real fluid actually happens and is connected with a property called viscosity of the fluid.

Because of the absence of tangential forces, on the boundary between a perfect fluid and a solid wall there exists a difference in relative tangential velocities, i.e., there is slip. In real fluids, on the contrary, the existence of intermolecular attractions causes the fluid to adhere to a solid wall and this gives rise to shear stresses.

## 1.1 Boundary-Layer Theory Outline

A good way to understand the nature of viscosity is to consider the following experiment.[1] We have a fluid between two very long parallel plates, one of which is at rest, the other moving with a constant velocity parallel to itself, as shown in Fig. 1.1.1.

It can be observed that the fluid adheres to both walls so that at $y = 0$ it's at rest, while at $y = h$ it has a velocity $U$ equal to the velocity of the upper plate.

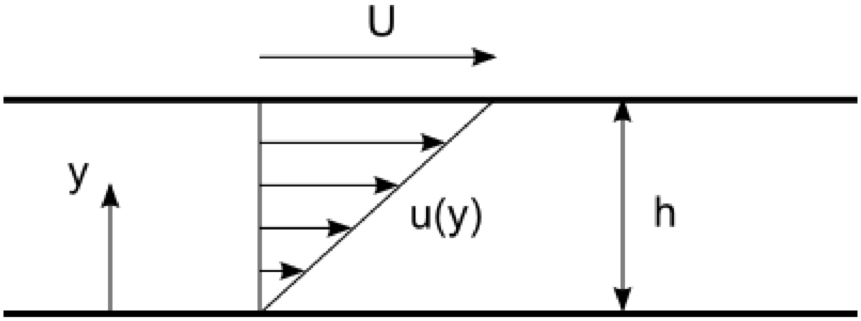

Figure 1.1.1: Velocity distribution in a viscous fluid between two parallel flat walls (Couette flow)

Furthermore, the velocity distribution in the fluid between the plates is linear, so that the fluid velocity is proportional to the distance $y$ from the lower plate and we have:

$$u(y) = \frac{y}{h}U. \tag{1.1.1}$$

In order to keep the plate moving a tangential force must be applied, which has to be in equilibrium with the frictional forces of the fluid. The experiment teaches that this force is proportional to the upper plate velocity $U$, and reversely proportional to the distance $h$ between the two walls. If we consider parallel force per unit area $\tau_0$ (shearing stress due to friction) this will be proportional to $U/h$, for which in general we may also substitute $du/dy$. The proportionality factor between $\tau_0$ and $du/dy$ it is called viscosity and it will be denoted with $\mu$, viscosity is a property of the fluid and it depends on a great extend on its temperature:

$$\tau_0 = \mu \frac{du}{dy}. \tag{1.1.2}$$

Dimensions of viscosity can be easily deduced if we consider that $\tau_0$ is a force per unit area and $\mu = \tau_0 \cdot dy/du$, so:

$$[\mu] = \left[\frac{N}{m^2}\frac{m \cdot s}{m}\right] = \left[\frac{N}{m^2}s\right] = [Pa \cdot s] \,.$$

Furthermore, when frictional and inertia forces interact it is important to consider the ratio between viscosity, $\mu$, and density, $\rho$, known as kinematic viscosity and denoted by $\nu$ :

$$\nu = \frac{\mu}{\rho}. \tag{1.1.3}$$

The presence of tangential (shearing) stresses and the condition of no slip at solid walls are the main differences between a perfect and a real fluids. Since a lot of fluids of great practical importance (such as air or water) have small viscosity coefficients, in most cases shear stresses can be neglected and the perfect fluid theory brings to satisfactory results.

Before going on it's better to define a very important dimensionless number: the Reynolds number. The Reynolds number is defined as the ratio between inertia and friction forces of a fluid in motion[1]:

$$Re = \frac{Inertia\, force}{Friction\, force} = \frac{\rho u {}^{\partial u}/_{\partial x}}{\mu {}^{\partial^2 u}/_{\partial y^2}} = \frac{\rho {}^{V^2}/_{d}}{\mu {}^{V}/_{d^2}} = \frac{\rho V d}{\mu} = \frac{V d}{\nu}. \tag{1.1.4}$$

This number is the main parameter to take into account when talking about incompressible fluids motion. In particular if we have two geometrically similar situations, for example motion around two geometrically similar objects, these situations are dynamically similar or have similar flows (geometrically similar streamlines, at all geometrically similar points the force acting on a fluid particle must bear a fixed ratio at every instant of time) only if their Reynolds numbers are identical.

As already said, the perfect fluid theory fails in evaluating the drag force experienced by an object in a fluid flow[1]. In Fig. 1.1.2 we can see a picture of the motion of water along a thin flat plate in which the streamlines were made visible by the sprinkling of particles on the surface of the water. The traces left by the particles are proportional to the flow velocity.

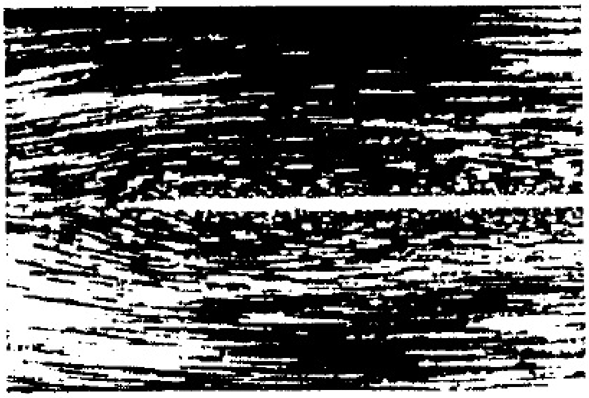

Figure 1.1.2: Motion along a thin flat plate

It can be seen that there is a thin layer, near the plate, where velocity is considerably smaller than at a larger distance from it. On this experimental evidence Prandtl built his boundary-layer theory, for this theory the thin layer near the wall can be considered as the only part of the flow field which experiences viscous effects (friction and shearing

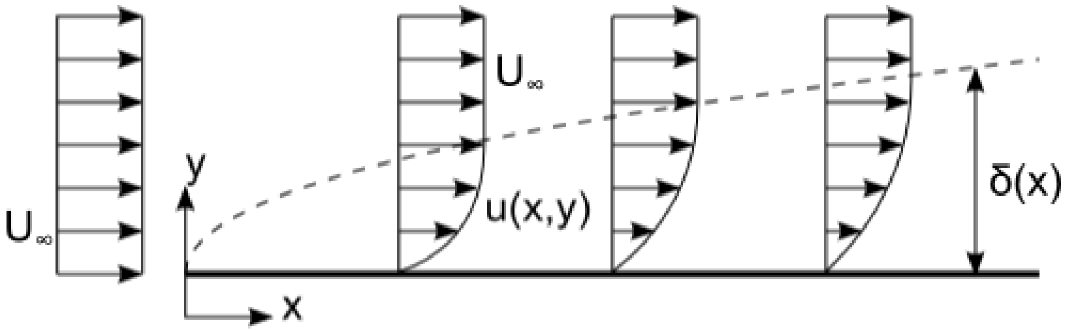

Figure 1.1.3: Sketch of boundary-layer on a flat plate in parallel flow at zero incidence

stress transmission through contacting layers) while the external flow can be studied adopting the perfect fluid theory. The thickness ($\delta(x)$) of this boundary-layer increases in downstream direction. Fig. 1.1.3 represents schematically the velocity distributions along a flat plate. Before the leading edge the velocity distribution is uniform, while proceeding along the plate the portion of retarded fluid becomes larger. Fluids having large viscosity will present also a greater boundary-layer thickness. On the contrary, a small value of viscosity won't bring to small values of shearing stress near the wall because of the presence of great velocity gradient (Eq. (1.1.2)). Since velocity in the boundary-layer tends asymptotically to the external velocity value $U$ it's impossible to define $\delta(x)$ in an unambiguous way, but in general it's considered to be the point where the parallel component $u$ of the velocity vector is $u = 0.99U$. It is also useful to define some other values which have a real physical meaning [1]. The displacement thickness $\delta_1(x)$ is that distance by which the external potential field of flow is displaced outwards as a consequence of the decrease in velocity in the boundary-layer and is defined as

$$\delta_1(x) = \frac{1}{U(x)} \int_{y=0}^{\infty} (U(x) - u(x))\, dy. \tag{1.1.5}$$

On the other hand the momentum thickness $\delta_2(x)$ symbolizes the loss of momentum due to the presence of boundary-layer, its definition is:

$$\delta_2(x) = \frac{1}{U^2(x)} \int_{y=0}^{\infty} u(u)\, (U(x) - u(x))\, dy. \tag{1.1.6}$$

## 1.2 Derivation of Boundary-Layer Equations

The governing equations of fluid motion are the Navier-Stokes equations. These equations express the two principles of conservation of mass and momentum. For incompressible flows they are:

$$\nabla \cdot \mathbf{v} = 0, \tag{1.2.1}$$

$$\rho \left( \frac{\partial \mathbf{v}}{\partial t} + \mathbf{v} \cdot \nabla \mathbf{v} \right) = -\nabla p + \mu \nabla^2 \mathbf{v} + \mathbf{f}. \tag{1.2.2}$$

Where Eq. (1.2.1) is the continuity equation while Eq. (1.2.2) is the momentum equation. The left side of the momentum equation evaluates the inertia per volume of the fluid, where $\frac{\partial \mathbf{v}}{\partial t}$ is the unsteady acceleration and $\mathbf{v} \cdot \nabla \mathbf{v}$ is the convective one. Convective acceleration is due to a change in velocity over position, think for example to a steady flow through a converging nozzle. On the right side we have all the amount of stress and forces acting on our fluid: $-\nabla p + \mu \nabla^2 \mathbf{v}$ is the divergence stress, where $-\nabla p$ is the pressure gradient and $\mu \nabla^2 \mathbf{v}$ the stress induced by viscosity, and $\mathbf{f}$ are the other body forces per volume (gravity for example). Considering $\mathbf{v} = \langle u, v \rangle$ Eq. (1.2.1) - (1.2.2), in a two dimensional flow with no relevant body forces, which is the case of an air flow passing around a thin airfoil, become respectively:

$$\frac{\partial u}{\partial x} + \frac{\partial v}{\partial y} = 0, \tag{1.2.3}$$

$$\rho \left( \frac{\partial u}{\partial t} + u \frac{\partial u}{\partial x} + v \frac{\partial u}{\partial y} \right) = -\frac{\partial p}{\partial x} + \mu \left( \frac{\partial^2 u}{\partial x^2} + \frac{\partial^2 u}{\partial y^2} \right), \tag{1.2.4a}$$

$$\rho \left( \frac{\partial v}{\partial t} + u \frac{\partial v}{\partial x} + v \frac{\partial v}{\partial y} \right) = -\frac{\partial p}{\partial y} + \mu \left( \frac{\partial^2 v}{\partial x^2} + \frac{\partial^2 v}{\partial y^2} \right). \tag{1.2.4b}$$

In general it is possible to state that the thickness of boundary-layer increases with viscosity or, more generally, that it decreases as the Reynolds number increases.[1] In particular it has been seen that the boundary-layer thickness is proportional to the square root of kinematic viscosity:

$$\delta = \sqrt{\nu}.$$

We can also assume that this thickness is very small compared to a linear still unspecified dimension, $L$, of the body

$$\delta \ll L.$$

This means that the solutions obtained from the boundary-layer equations will apply to very large Reynolds numbers.

In order to simplify the Navier-Stokes equations we have to estimate the order of magnitude of every term. If we consider the two dimensional problem shown in Fig. 1.2.1 we can assume the wall to be flat and coincident with the $x$-direction, the $y$-direction being perpendicular to it. Lets now rewrite the Navier-Stokes equations by

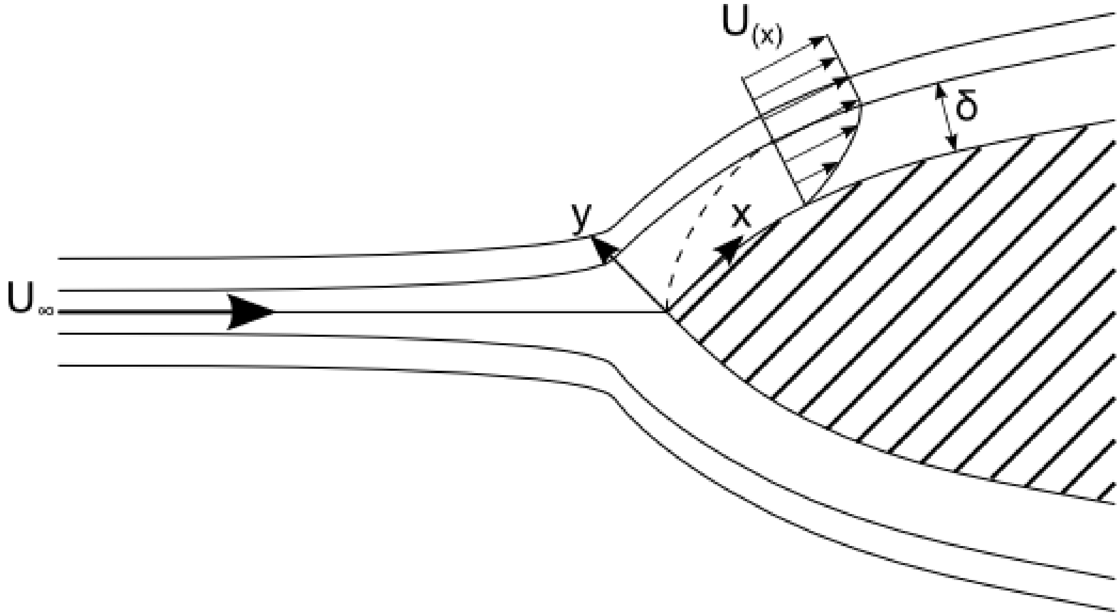

Figure 1.2.1: Boundary-layer flow along a wall

referring all velocities to the free stream velocity, $U_\infty$, and all the linear dimensions to a characteristic length of the body, $L$, which is so selected as to ensure that the dimensionless derivative, $\partial u/\partial x$, does not exceed unity in the region under consideration. The pressure is made dimensionless by $\rho U_\infty^2$, while time is divided by $L/U_\infty$. Under these assumptions, and retaining the same symbols for dimensionless quantities as for their dimensional counterparts, the Navier-Stokes equations become:

$$\frac{\partial u}{\partial x} + \frac{\partial v}{\partial y} = 0, \tag{1.2.5}$$

$$\frac{\partial u}{\partial t} + u\frac{\partial u}{\partial x} + v\frac{\partial u}{\partial y} = -\frac{\partial p}{\partial x} + \frac{1}{Re}\left(\frac{\partial^2 u}{\partial x^2} + \frac{\partial^2 u}{\partial y^2}\right), \tag{1.2.6a}$$

$$\frac{\partial v}{\partial t} + u\frac{\partial v}{\partial x} + v\frac{\partial v}{\partial y} = -\frac{\partial p}{\partial y} + \frac{1}{Re}\left(\frac{\partial^2 v}{\partial x^2} + \frac{\partial^2 v}{\partial y^2}\right). \tag{1.2.6b}$$

With boundary conditions which are the absence of slip between fluid and the wall, i.e. $u = v = 0$ for $y = 0$, $u = U$ for $y = \infty$, and $Re = \frac{U_\infty L}{\nu}$.

With these assumptions the dimensionless boundary-layer, for which we will retain the symbol $\delta$, is very small compared to unity ($\delta \ll 1$). We will now estimate the order of magnitude of every term in order to be able to drop smaller terms and simplify the equations. We can see that $\partial u/\partial x$ is of the order 1, like $\partial^2 u/\partial x^2$, further, since $v$ at the wall is 0, $v$ in the boundary-layer is of the order of $\delta$, thus $\partial v/\partial y$ is of the order of $1 (= \delta/\delta)$. Further, $\partial v/\partial x$ and $\partial^2 v/\partial x^2$ are also of the order of $\delta$, while $\partial^2 u/\partial y^2$ is of the order of $\frac{1}{\delta^2}$ and

${}^{\partial^2 v}\!/\!{}_{\partial y^2}$ is of the order of $\frac{1}{\delta}$. We shall also assume that the unsteady acceleration ${}^{\partial u}\!/\!{}_{\partial t}$ is of the same order of magnitude of the convective term $u{}^{\partial u}\!/\!{}_{\partial x}$, this will exclude very sudden accelerations, such as occur in very large pressure waves. Since we said that in boundary-layer viscous forces are comparable to inertial ones, we will have at least one viscous term of the same order of magnitude of the inertial terms and this can happen only if:

$$\frac{1}{Re} = \delta^2.$$

So, as it was already said before, we are talking about very large Reynolds numbers.

It's now possible to simplify the equations by neglecting elements which are of an order of magnitude smaller than 1, so these three new equations are obtained:

$$\frac{\partial u}{\partial x} + \frac{\partial v}{\partial y} = 0, \tag{1.2.7}$$

$$\frac{\partial u}{\partial t} + u\frac{\partial u}{\partial x} + v\frac{\partial u}{\partial y} = -\frac{\partial p}{\partial x} + \frac{1}{Re}\frac{\partial^2 u}{\partial y^2}, \tag{1.2.8a}$$

$$\delta = -\frac{\partial p}{\partial y}. \tag{1.2.8b}$$

The pressure variation through the boundary-layer, obtained by integrating Eq. (1.2.8b), results to be of the order $\delta^2$, which is very small. Thus, it is possible to state that the pressure in a direction normal to the boundary-layer is practically constant. It can be assumed to take the pressure value at the outer edge of boundary-layer, determined by the frictionless flow. The pressure is said to be "impressed" on the boundary-layer by the outer flow[1].

Going back to dimensional values, it is now possible to write down the simplified Navier-Stokes equations, also known as Prandtl's boundary-layer equations:

$$\frac{\partial u}{\partial x} + \frac{\partial v}{\partial y} = 0, \tag{1.2.9a}$$

$$\frac{\partial u}{\partial t} + u\frac{\partial u}{\partial x} + v\frac{\partial u}{\partial y} = -\frac{1}{\rho}\frac{\partial p}{\partial x} + \nu\frac{\partial^2 u}{\partial y^2}. \tag{1.2.9b}$$

With boundary conditions

$$y = 0: \quad u = v = 0; \qquad y = \infty: \quad u = U\left(x, t\right). \tag{1.2.10}$$

At the outer edge of boundary-layer the parallel component of the flow, $u$, is equal to the outer velocity, $U\left(x,t\right)$. Since there is no large velocity gradient the viscous term in Eq. (1.2.9b) vanishes for big Reynolds numbers. Thus for the outer region we obtain:

$$\frac{\partial U}{\partial t} + U\frac{\partial U}{\partial x} = -\frac{1}{\rho}\frac{\partial p}{\partial x}. \tag{1.2.11}$$

It's now possible to substitute the pressure term in Eq. (1.2.9b), obtaining the boundary-layer equations that will be used from now on:

$$\frac{\partial u}{\partial x} + \frac{\partial v}{\partial y} = 0, \tag{1.2.12a}$$

$$\frac{\partial u}{\partial t} + u\frac{\partial u}{\partial x} + v\frac{\partial u}{\partial y} = \frac{\partial U}{\partial t} + U\frac{\partial U}{\partial x} + \nu\frac{\partial^2 u}{\partial y^2}. \tag{1.2.12b}$$

With the same boundary conditions of Eq. (1.2.10).

## 1.3 Boundary-Layer on a Plate

The analysis of a fluid flow can be carried on considering a steady or unsteady approach. Steady state occurs when values of all the fluid properties are unchanging in time, so that, considering a property $x$ of the system, its partial derivative with respect to time is zero:

$$\frac{\partial x}{\partial t} = 0.$$

Hence in a steady state analysis it is possible to not taking into account the time variable, since the only variations of properties concern space derivatives.

On the other hand the unsteady state (or transient state) is the most general situation in which properties change in space and time, and it is necessary to deal also with the time variable.

### 1.3.1 Laminar Flow

Laminar flow generally occurs at lower velocities, which means that we have laminar boundary-layer, for example, near the leading edge of a rotor blade. In laminar regime the fluid flows in parallel layers, with no disruption between them[2]. Adjacent layers slide past one on the other without lateral mixing, just like playing cards.

Historically, the first example illustrating the application of Prandtl's boundary-layer theory was the flow along a flat plate at zero incidence.

Let the leading edge of the plate be at $x = 0$, the plate being parallel to the $x$-axis and infinitely long downstream (Fig. 1.3.1). Since there are no pressure gradients,

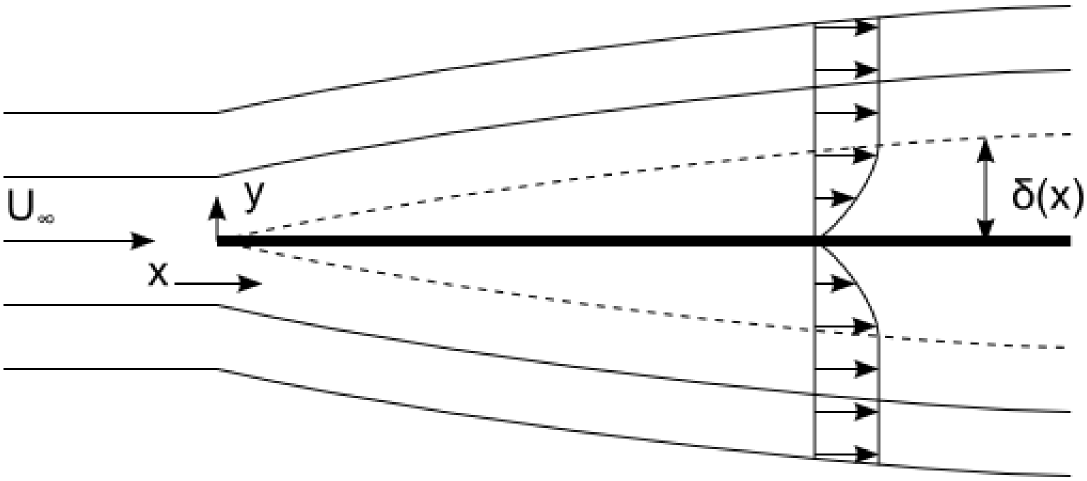

Figure 1.3.1: The boundary-layer along a flat plate at zero incidence

which means also no external velocity variations, the boundary-layer equations become:

$$\frac{\partial u}{\partial x}+\frac{\partial v}{\partial y}=0, \tag{1.3.1}$$

$$u\frac{\partial u}{\partial x}+v\frac{\partial u}{\partial y}=\nu\frac{\partial^2 u}{\partial y^2} \tag{1.3.2}$$

with boundary conditions written in Eq. (1.2.10). Since there isn't a preferred length it seems reasonable to suppose that the velocity profiles at varying distances from the leading edge are similar to each other, which means that the velocity curves $u(y)$ at different distances from the leading edge can be made identical by selecting suitable scale factors for $u$ and $y$. The two selected scaling factors are $U_\infty$ for $u$ and the boundary-layer thickness $\delta(x)$ for $y$. Hence the principle of similarity of velocity profiles through the boundary-layer can be written as $u/U_\infty = f(\eta)$, where $\eta = y/\delta$ and the function $f$ must be the same at all distances $x$ from the leading edge.

In order to solve this problem the momentum Eq. (1.3.2) is applied to the case of a flat plate at zero incidence, considering the control surface shown in Fig. 1.3.2.

We can say that the flux of momentum through the control surface, considered fixed in space, is equal to the skin friction on the plate $D(x)$ from the leading edge ($x = 0$) to the current section at $x$. Hence, the drag of a plate wetted on one side is given by:

$$D(x)=b\rho\int_{y=0}^{\infty}u(U_\infty-u)dy, \tag{1.3.3}$$

where the integral has to be taken at the section $x$ and $b$ is the width of the flat plate. On the other hand the drag can be expressed as an integral of the shearing stress $\tau_0$ at the wall, taken along the plate:

$$\tau_0(x) = \rho \frac{d}{dx} \int_{y=0}^{\infty} u(U_\infty - u)dy. \tag{1.3.4}$$

Comparing the last two equations we obtain:

$$D(x) = b \int_0^x \tau_0(x)dx. \tag{1.3.5}$$

If we now introduce momentum thickness $\delta_2$, defined by Eq. (1.1.6), we have:

$$U_\infty^2 \frac{d\delta_2}{dx} = \frac{\tau_0}{\rho}. \tag{1.3.6}$$

Considering Eq. (1.3.4) and (1.3.6) we can now obtain an approximate solution of our problem. The essence of the approximate solution is to assume a suitable velocity profile $u(y)$ within the boundary-layer, which means a suitable function $f(\eta)$ taking care that it satisfies the boundary conditions. So the function must vanish at the wall ($\eta = 0$ means $y = 0$) and tend to 1 for large values of $\eta$. It's useful to consider that the transition between boundary-layer and external flow occurs at a finite distance from the wall. In other words, we assume a finite boundary-layer thickness, in spite of the fact that exact solutions tend asymptotically to the potential flow of the particular problem. In this connexion the boundary-layer thickness has no physical significance, being only a useful quantity for computation.

Having assumed the function $f(\eta)$ the momentum integral becomes:

$$\int_{y=0}^{\infty} u(U_\infty - u)dy = U_\infty^2 \delta(x) \int_{\eta=0}^{1} f(1-f)d\eta, \tag{1.3.7}$$

where the last integral can be evaluated provided that a specific assumption is made

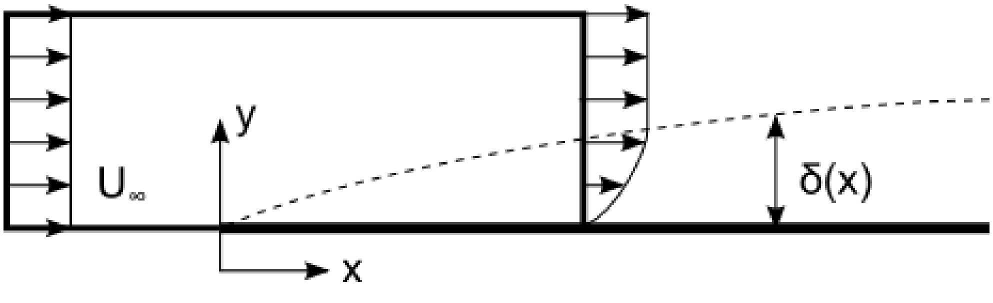

Figure 1.3.2: Application of the momentum equation to the flow past a flat plate at zero incidence.

for $f(\eta)$. Putting

$$\alpha_1 = \int_{\eta=0}^{1} f(1-f)d\eta \tag{1.3.8}$$

we have

$$\int_{y=0}^{\infty} u(U_\infty - u)dy = U_\infty^2 \delta_2 = \alpha_1 \delta U_\infty^2 \tag{1.3.9}$$

which means that

$$\delta_2 = \alpha_1 \delta\left(x\right). \tag{1.3.10}$$

While the displacement thickness $\delta_1$, defined by Eq. (1.1.5), becomes

$$\delta_1 = \alpha_2 \delta\left(x\right) \tag{1.3.11}$$

by putting

$$\alpha_2 = \int_{\eta=0}^{1} (1-f)d\eta. \tag{1.3.12}$$

While $\tau_0$ is given by

$$\frac{\tau_0}{\rho} = \nu \left(\frac{\partial u}{\partial y}\right)_{y=0} = \frac{\nu U_\infty}{\delta} f'(0) = \beta_1 \frac{\nu U_\infty}{\delta}. \tag{1.3.13}$$

So the momentum Eq. (1.3.6), introducing these values, becomes

$$\delta \frac{d\delta}{dx} = \frac{\beta_1}{\alpha_1} \frac{\nu}{U_\infty} \tag{1.3.14}$$

and integrating it from $\delta = 0$ for $x = 0$ we obtain

$$\delta(x) = \sqrt{\frac{2\beta_1}{\alpha_1} \frac{\nu x}{U_\infty}} \tag{1.3.15}$$

and

$$\tau_0 = \mu U_\infty \sqrt{\frac{\alpha_1 \beta_1}{2} \frac{U_\infty}{\nu x}}, \tag{1.3.16}$$

while $\delta_1\left(x\right)$ and $\delta_2\left(x\right)$ are obtained by Eq. (1.3.11) and (1.3.10).

The function $f$ which was chosen is the von Karman-Pohlhausen function for a flat plate at zero incidence[1]:

$$\frac{u}{U} = f(\eta) = 2\eta - 2\eta^3 + \eta^4. \tag{1.3.17}$$

| Velocity distribution $u/U = f(\eta)$ | $\alpha_1$ | $\alpha_2$ | $\beta_1$ | $\delta_1\sqrt{\frac{U_\infty}{\nu x}}$ | $\frac{\tau_0}{\mu U_\infty}\sqrt{\frac{\nu x}{U_\infty}}$ | $\frac{\delta_1}{\delta_2}$ |
|---|---|---|---|---|---|---|
| $f(\eta) = 2\eta - 2\eta^3 + \eta^4$ | $\frac{37}{315}$ | $\frac{3}{10}$ | 2 | 1.754 | 0.343 | 2.52 |
| exact | - | - | - | 1.721 | 0.332 | 2.59 |

Table 1.3.1: Results of the calculation of the boundary-layer for a flat plate at zero incidence based on approximate theory

Assuming this velocity distribution within the boundary-layer we have

$$\alpha_1 = \frac{37}{315},$$

$$\alpha_2 = \frac{3}{10}$$

and

$$\beta_1 = 2.$$

Obtained results are reported in Table 1.3.1, compared with those of the exact solution. In Fig. 1.3.3 boundary-layer thickness $\delta$, displacement thickness $\delta_1$ and momentum thickness $\delta_2$ along the flat plate are plotted. In Fig. 1.3.4 it's possible to see how the main part of viscous shearing stress occurs at the beginning of the flat plate, where the boundary-layer is thinner and this brings to a greater velocity gradient through it. Finally Fig. 1.3.5 shows how two velocity profiles taken at different $x$ coordinates are similar, scaled with boundary-layer thickness $\delta(x)$. The good accordance with the exact solution and the simple calculations involved in this method make it a valid solution.

The next step has been to apply the preceding method to the general case of a two-dimensional laminar boundary-layer with pressure gradient. In this case $x$ denotes the arc on the wet surface and $y$ the distance from it. With this new coordinate system the momentum equation, obtained by integrating the equation of motion with respect to $y$ from the wall at $y = 0$ to a certain distance $h(x)$, which is assumed to be outside of the boundary-layer for all values of $x$, becomes

$$U^2\frac{d\delta_2}{dx} + (2\delta_2 + \delta_1)\,U\frac{dU}{dx} = \frac{\tau_0}{\rho}. \tag{1.3.18}$$

This gives us, as before, a differential equation to integrate once we have assumed a suitable velocity function. The function we decided to assume is the von Karman-

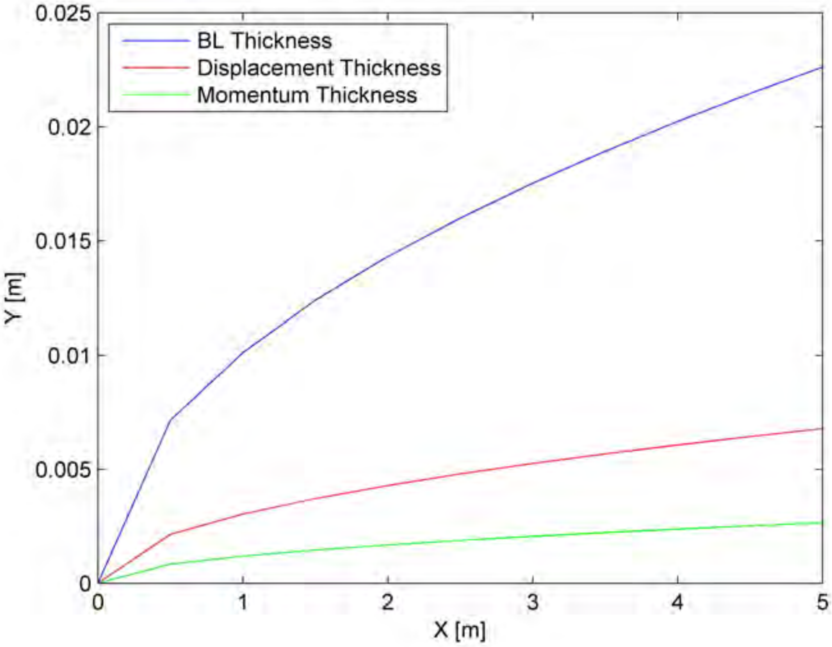

Figure 1.3.3: Boundary-layer thickness (blue), displacement thickness (red) and momentum thickness (green) along a flat plate with fully laminar flow

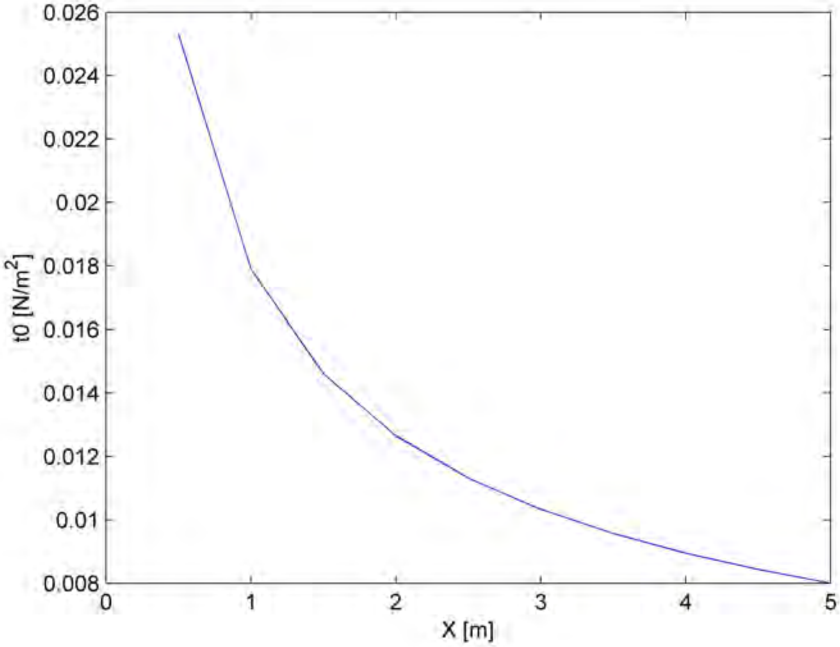

Figure 1.3.4: Viscous shearing stress at the wall of a flat plate with fully laminar flow

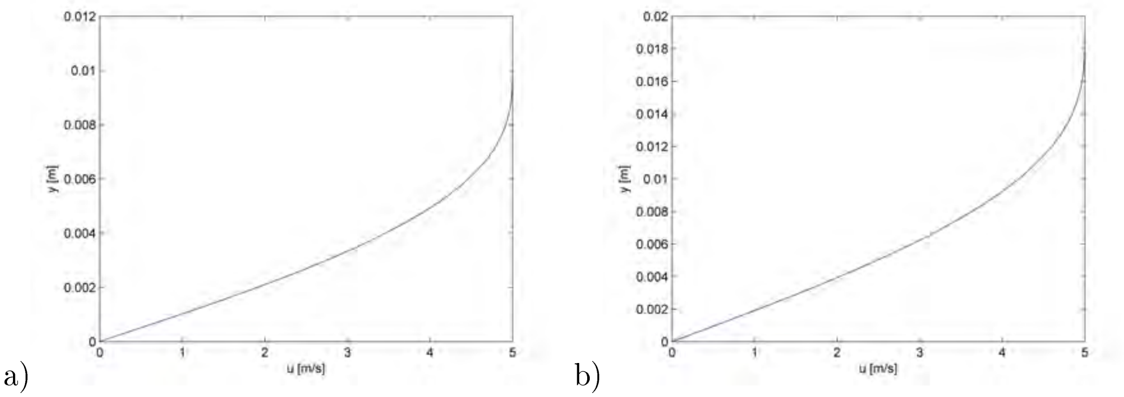

Figure 1.3.5: Velocity profiles through the boundary-layer at $x = 1\,\mathrm{m}$ a) and $x = 3.5\,\mathrm{m}$ b) on a flat plate of total length $L = 5\,\mathrm{m}$ with fully laminar flow

Pohlhausen function[3]:

$$\frac{u}{U} = f(\eta) = \left(2 + \frac{\Lambda}{6}\right)\eta - \frac{\Lambda}{2}\eta^2 + \left(-2 + \frac{\Lambda}{2}\right)\eta^3 + \left(1 - \frac{\Lambda}{6}\right)\eta^4 \tag{1.3.19}$$

where $\Lambda$ is a shape factor defined by

$$\Lambda = \frac{\delta^2}{\nu}\frac{dU}{dx}. \tag{1.3.20}$$

In this case $\alpha_1$, $\alpha_2$ and $\beta_1$ become respectively

$$\frac{37}{315} - \frac{\Lambda}{945} - \frac{\Lambda^2}{9072}, \quad \frac{3}{10} - \frac{\Lambda}{120}, \quad 2 + \frac{\Lambda}{6}. \tag{1.3.21}$$

Values of $\Lambda$ go from $-12$ to 12[1]. At $-12$ we have be boundary-layer separation, we can observe indeed a inflection point in the velocity profile[3], while the value of $\Lambda$ for the stagnation point at the leading edge it's 7.052[1]. It can be useful to notice that, as we already said, the flat plate at zero incidence is a particular case of this model which has $\Lambda = 0$. In order to bring the momentum equation to a dimensionless form, it is possible to multiply it by $\delta_2/(\nu U)$ and we obtain

$$\frac{U}{\nu}\delta_2\frac{d\delta_2}{dx} + \frac{\delta_2^2}{\nu}\frac{dU}{dx}\left(2 + \frac{\delta_1}{\delta_2}\right) = \frac{\delta_2}{U}\frac{\tau_0}{\rho}. \tag{1.3.22}$$

Introducing the new shape factor

$$K(x) = \frac{\delta_2^2}{\nu}\frac{dU}{dx} = \left(\frac{37}{315} - \frac{\Lambda}{945} - \frac{\Lambda^2}{9072}\right)^2\Lambda \tag{1.3.23}$$

we obtain

$$U\frac{d}{dx}\left(\frac{K}{dU/dx}\right)=2\left(\frac{37}{315}-\frac{\Lambda}{945}-\frac{\Lambda^2}{9072}\right)\left(2-\frac{116}{315}\Lambda+\frac{79}{7560}\Lambda^2+\frac{1}{4536}\Lambda^3\right). \tag{1.3.24}$$

It is now necessary to integrate Eq. (1.3.24) from the stagnation point at the leading edge, where $\Lambda = 7.052$, until the current section $x$ to evaluate $\Lambda$. Thus, from the definition of the shape factor (Eq. (1.3.20)), evaluate the boundary-layer thickness, so that it's possible to calculate also the displacement and momentum thickness and the viscous shear stress at the wall.

### 1.3.2 Turbulent Flow

The turbulent flow is a chaotic flow where properties like velocity and pressure change very quickly in space and time. Turbulent flow occurs at higher velocities and Reynolds numbers, it means that viscous forces are not strong enough to overwhelm inertial forces, the resultant motion is ruled by the chaos theory laws. Hence, knowing the precise starting condition of every particle we will be able to predict exactly the development of the whole flow field, but the minimum difference from the actual starting set up will lead us to a completely different final solution. For these reasons the turbulent flow is normally treated statistically rather than deterministically. From previous considerations it could seem impossible to talk about steady state for a turbulent flow, in fact experimental investigations highlightened that a turbulent flow can be considered steady when its properties present a mean value (unchanging in time) with superimposed fluctuations. This assumption leads to the Reynolds decomposition: a mathematical technique to separate the average and fluctuating parts of a quantity, and which allows us to deal with steady turbulent flows. For example, for a quantity $u$ the decomposition would be

$$u(x,y,z,t)=\overline{u(x,y,z)}+u'(x,y,z,t)$$

and, averaging on time:

$$\frac{1}{T}\int_0^T u(x,y,z,t)dt=\frac{1}{T}\left(\int_0^T\overline{u(x,y,z)}dt+\int_0^T u'(x,y,z,t)dt\right)=\overline{u(x,y,z)}.$$

On the other hand, if we multiply two different quantities (i.e. $u$ and $v$) the result will be:

$$\overline{u\cdot v}=\overline{u}\cdot\overline{v}+\overline{u'v'}.$$

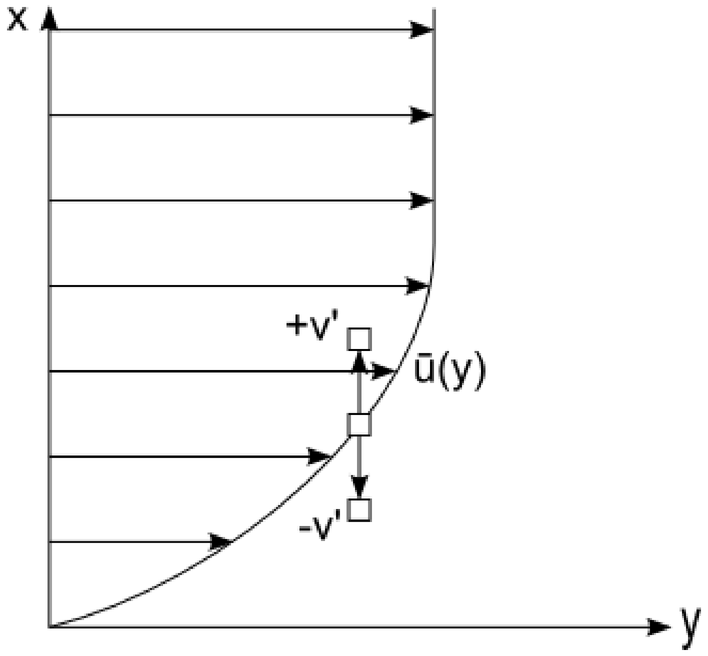

Figure 1.3.6: Transport of momentum due to turbulent velocity fluctuation

So the two-dimensional incompressible steady turbulent boundary-layer equations are[1]:

$$\frac{\partial \overline{u}}{\partial x} + \frac{\partial \overline{v}}{\partial y} = 0, \tag{1.3.25a}$$

$$\overline{u}\frac{\partial \overline{u}}{\partial x} + \overline{v}\frac{\partial \overline{u}}{\partial y} = \overline{U}\frac{\partial \overline{U}}{\partial x} + \frac{\partial}{\partial y}\left(\nu\frac{\partial \overline{u}}{\partial y} - \overline{u'v'}\right). \tag{1.3.25b}$$

Hence, the main difference between the laminar and turbulent boundary-layer equations is the presence of the term $-\frac{\partial \overline{u'v'}}{\partial y}$ which is called apparent turbulent stress or Reynolds shear stress[1]. It can be interpreted as the transport of momentum in the $x$ direction through a surface normal to the $y$-axis. Considering, for example, the mean flow given in Fig. 1.3.6 we can see that the mean product $\overline{u'v'}$ is different from zero: for example, the particles which travel upwards in view of the turbulent fluctuation ($v' > 0$) arrive to a layer $y$ where a greater mean velocity $\overline{u}$ prevails. Since they preserve their original velocity, they give rise to a negative component $u'$. Conversely, a positive $u'$ will rise in a lower $y$ layer if we have a negative $v'$.

To show the development of a turbulent boundary-layer along a flat plate we'll refer to the same situation considered for the laminar flow and an approximate solution, true for moderate Reynolds numbers, is adopted[1].

The skin-friction drag on a flat plate at zero incidence, as already seen in Eq. (1.3.3) and (1.3.5), satisfies this relation:

$$D\left(x\right)=b\rho\int_{y=0}^{\infty}u(U_{\infty}-u)dy=D(x)=b\int_{0}^{x}\tau_{0}(x)dx \tag{1.3.26}$$

which, introducing the momentum thickness $\delta_2$ defined by Eq. (1.1.6), becomes

$$D\left(x\right)=b\rho U_{\infty}^{2}\delta_{2}\left(x\right) \tag{1.3.27}$$

and substituting the definition of momentum thickness (Eq. (1.1.6)) we have

$$\frac{1}{b}\frac{dD}{dx}=\tau_{0}\left(x\right)=\rho U_{\infty}^{2}\frac{d\delta_{2}}{dx}. \tag{1.3.28}$$

We now consider again a self similar solution, with velocity profiles, defined by:

$$\frac{u}{U_{\infty}}=\left(\frac{y}{\delta}\right)^{\frac{1}{7}} \tag{1.3.29}$$

with $\delta\left(x\right)$ which is to be determined in the course of calculation. Shearing stress at the wall is also assumed as[1]:

$$\frac{\tau_{0}}{\rho U_{\infty}^{2}}=0.0225\left(\frac{\nu}{U_{\infty}\delta}\right)^{\frac{1}{4}}. \tag{1.3.30}$$

From Eq. (1.1.5)-(1.1.6) and from Eq. (1.3.29) we obtain:

$$\delta_{1}=\frac{\delta}{8};\qquad\delta_{2}=\frac{7}{72}\delta. \tag{1.3.31}$$

Considering Eq. (1.3.28) and (1.3.31) we have

$$\frac{\tau_{0}}{\rho U_{\infty}^{2}}=\frac{7}{72}\frac{d\delta}{dx} \tag{1.3.32}$$

and, comparing last equation with Eq. (1.3.30), the result is

$$\frac{7}{72}\frac{d\delta}{dx}=0.0225\left(\frac{\nu}{U_{\infty}\delta}\right)^{\frac{1}{4}}. \tag{1.3.33}$$

Integrating Eq. (1.3.33) with $\delta=0$ at $x=0$ we have that the boundary-layer thickness is:

$$\delta\left(x\right)=0.37x\left(\frac{U_{\infty}x}{\nu}\right)^{-\frac{1}{5}}. \tag{1.3.34}$$

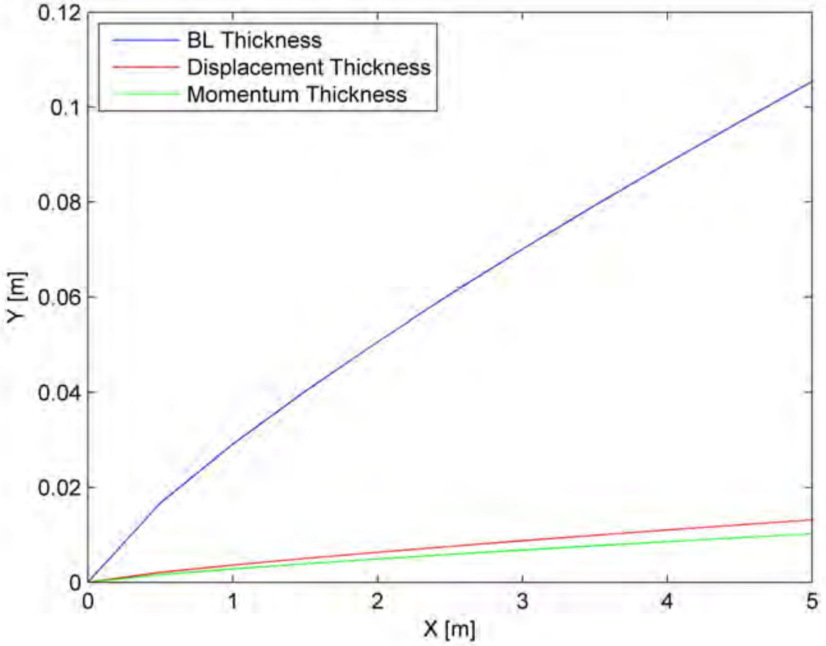

Figure 1.3.7: Boundary-layer thickness (blue), displacement thickness (green) and momentum thickness (red) along a flat plate with fully turbulent flow

The obtained boundary-layer thickness, displacement thickness and momentum thickness are plotted in Fig. 1.3.7. Again, like for the laminar flow, we have a peak of shearing stress at the wall near the leading edge, as it can be seen in Fig. 1.3.8 while in Fig. 1.3.9 are shown two velocity profiles, taken at different $x$ coordinates, and they're clearly similar.

It's interesting to make some comparisons between laminar and turbulent boundary-layer. In Fig. 1.3.10 it can be seen how the turbulent boundary-layer is way thicker than the laminar one and, with turbulent boundary-layer, we have also greater shear stresses at the wall (Fig. 1.3.11). This last evidence seems to be absurd. Indeed if we think about the definition of shear stress $\left(\tau = \mu \frac{du}{dy}\right)$ it seems to suggest that a thicker boundary-layer determines a smaller value of shear stress (and that's actually why we always have a peak of shear stress at the wall near the leading edge, where the boundary-layer is thinner). However the reason of this phenomenon is the different velocity profile through a laminar or turbulent boundary-layer. Looking at Fig. 1.3.12, indeed, it's possible to notice that for the turbulent boundary-layer we have a steep increase in velocity very close to the wall, and that's why in this case we have a greater wall shear stress.

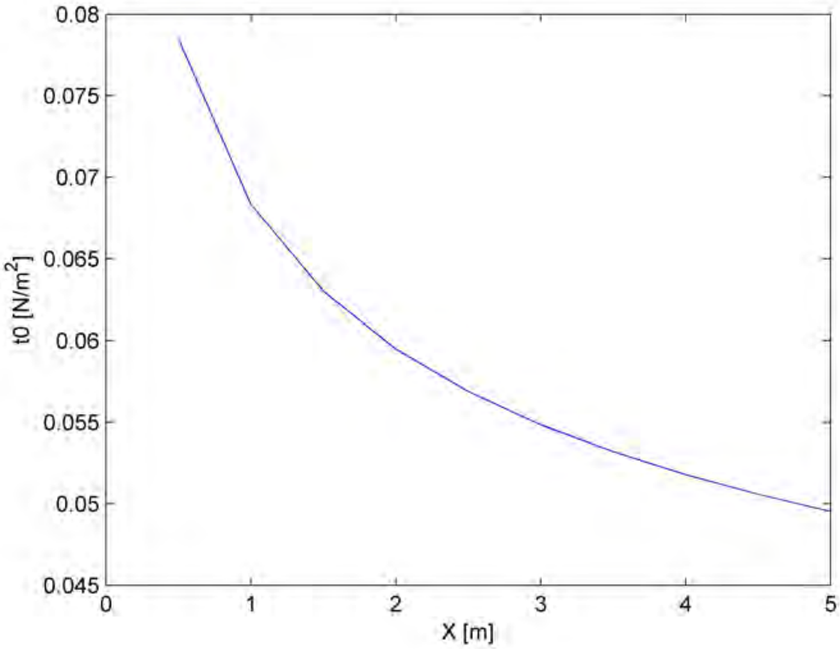

Figure 1.3.8: Viscous shearing stress at the wall of a flat plate with fully turbulent flow

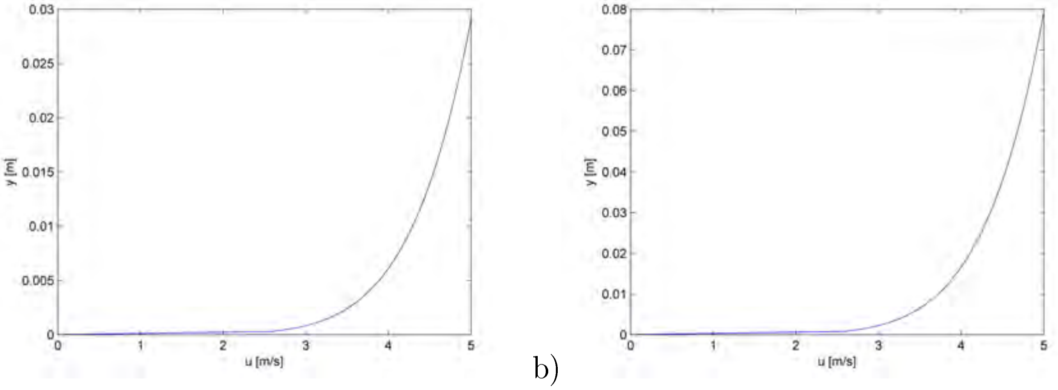

a) b)

Figure 1.3.9: Velocity profiles through the boundary-layer at $x = 1\,\mathrm{m}$ a) and $x = 3.5\,\mathrm{m}$ b) on a flat plate of total length $L = 5\,\mathrm{m}$ with fully turbulent flow

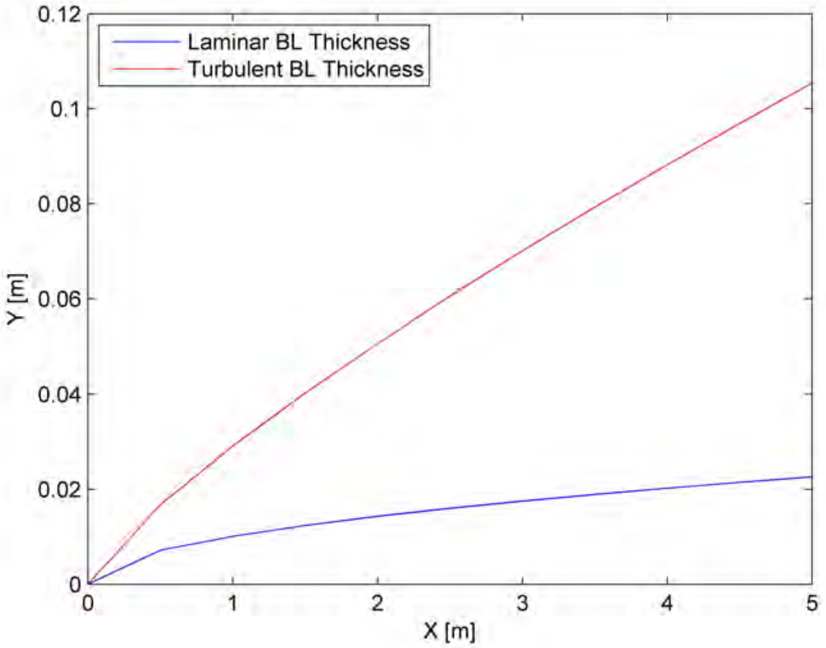

Figure 1.3.10: Comparison between laminar (blue) and turbulent (red) boundary-layer thickness on a flat plate

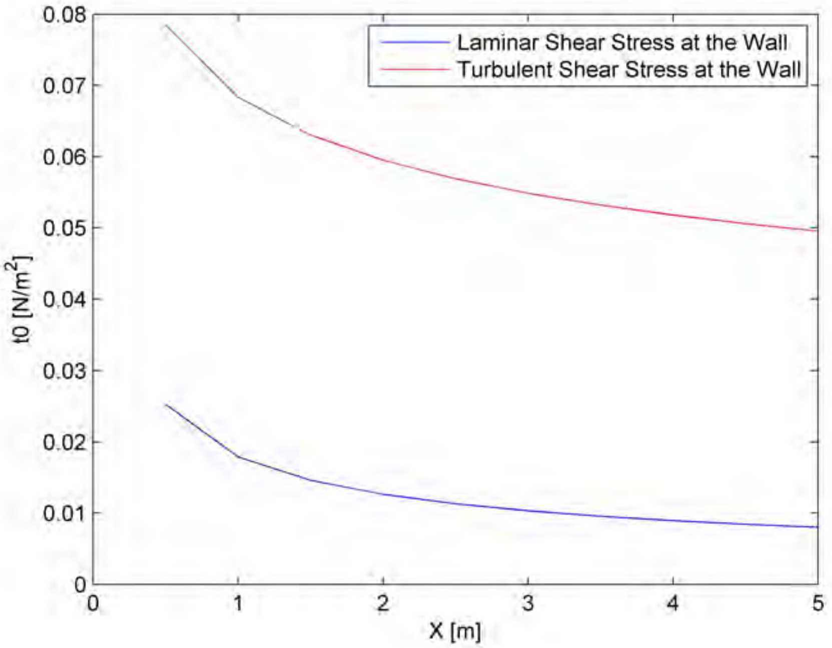

Figure 1.3.11: Comparison between laminar (blue) and turbulent (red) viscous shear stress at the wall on a flat plate

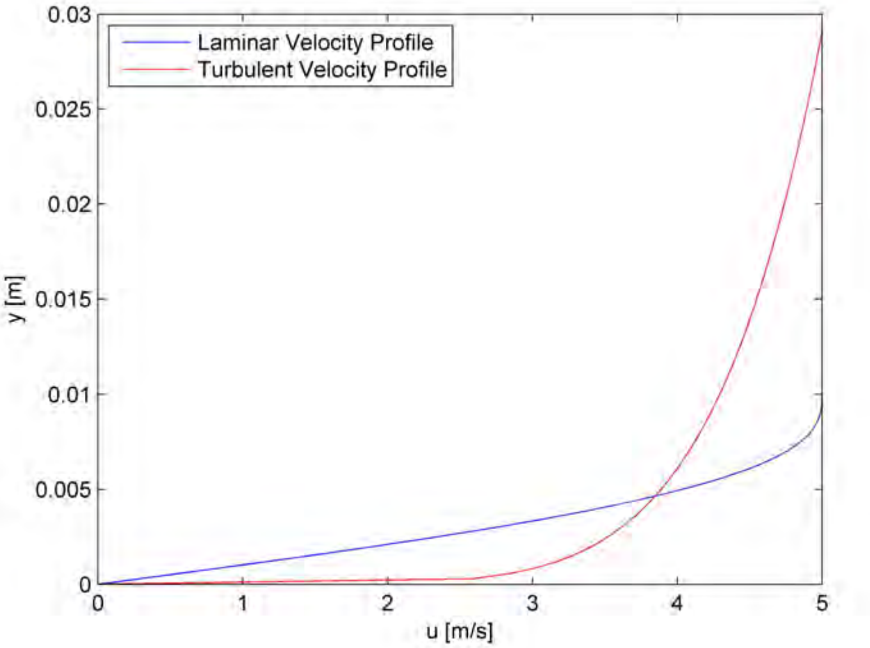

Figure 1.3.12: Comparison between laminar (blue) and turbulent (red) velocity profile through the boundary-layer at $x = 1\,\mathrm{m}$ on a flat plate of total length $L = 5\,\mathrm{m}$

## 1.4 Unsteady Boundary-Layer Theory

The unsteady state (or transient state) is the most general situation in which properties change in space and time, and it is necessary to deal also with the time variable. Unsteady motion occurs quite often in helicopter rotors, where the periodic pitching movement is a fundamental movement of the blade, or during start-up and shut-down processes.

In laminar flow the unsteady boundary-layer equations are exactly Eq. (1.2.12) with boundary conditions of Eq. (1.2.10).

On the other hand turbulent flows are, in fact, by definition unsteady, so it is necessary to explain what is meant with “unsteady turbulent flow”. With Reynolds decomposition turbulent flows were divided into the time averaged flow (which is time independent) and the random fluctuations which varied in time. Now, also the “mean” motion will be time dependent. So the Reynolds decomposition is slightly modified and the velocity component in the $x$ direction can be written as:

$$u\left(x,y,z,t\right) = \overline{u}\left(x,y,z\right) + \widetilde{u}\left(x,y,z,t\right) + u'\left(x,y,z,t\right) \tag{1.4.1}$$

where $\overline{u}$ is the time independent component of mean motion, $\tilde{u}$ its time dependent component and $u'$, again, the disordered turbulent fluctuation.

Using this new formulation we can define:

$$u = \overline{u} + \widetilde{u}, \qquad v = \overline{v} + \widetilde{v}. \tag{1.4.2}$$

And the boundary-layer equations become[4]:

$$\frac{\partial u}{\partial x} + \frac{\partial v}{\partial y} = 0, \tag{1.4.3a}$$

$$\frac{\partial u}{\partial t} + u\frac{\partial u}{\partial x} + v\frac{\partial u}{\partial y} = \frac{\partial U}{\partial t} + U\frac{\partial\ U}{\partial x} + \frac{\partial}{\partial y}\left(\nu\frac{\partial u}{\partial y} - \overline{u'v'}\right). \tag{1.4.3b}$$

$$y = 0: \quad u = v = 0; \qquad y = \delta: \quad u = U\left(x\right). \tag{1.4.4}$$

Such a complex flow field must be solved with a numerical method and, in order to do this, a turbulence model has to be applied.

### 1.4.1 Turbulence Model

The most common approach to the problem of calculating the Reynolds stresses is to define an eddy viscosity, $\nu_t$, in the same form as the laminar viscosity[5]. Thus, for a two-dimensional incompressible flow, we have:

$$-\overline{u'v'} = \nu_t\frac{\partial u}{\partial y}. \tag{1.4.5}$$

On the other hand, using the mixing length, $l$, concept we can also write:

$$-\overline{u'v'} = l^2\left(\frac{\partial u}{\partial y}\right)^2. \tag{1.4.6}$$

And, from the last two equations, we obtain the well-known Prandtl mixing length formula:

$$\nu_t = l^2\left|\frac{\partial u}{\partial y}\right|. \tag{1.4.7}$$

In this work the Cebeci-Smith method will be applied[6]. In this method the boundary-layer is separated in two sub-layers with two different formulations for the eddy viscosity $\nu_t$. For the inner region the Prandtl mixing length hypothesis is maintained, and the eddy viscosity is:

$$\left(\nu_t\right)_i = l^2\left|\frac{\partial u}{\partial y}\right|\gamma_{tr}, \qquad 0 \leq y \leq y_c. \tag{1.4.8}$$

Here $\gamma_{tr}$ is an intermittency factor, while $y_c$ is the wall-normal distance where the outer region for the turbulent viscosity starts. The mixing length $l$ is given by:

$$l = ky\left[1 - exp\left(-\frac{y}{A}\right)\right] \tag{1.4.9}$$

where $k = 0.4$. $A$ is a damping length constant which is expressed as:

$$A = 26\frac{\nu}{Nu_\tau}, \qquad N = \sqrt{1 - 11.8p^+}, \qquad p^+ = \frac{\nu U}{u_\tau^3}\frac{dU}{dx} \tag{1.4.10}$$

where $u_\tau$ is the friction velocity, defined by:

$$u_\tau = \sqrt{\frac{\tau_0}{\rho}}. \tag{1.4.11}$$

The intermittency factor $\gamma_{tr}$ ensures a smooth transition between laminar and turbulent flow and it is given by:

$$\gamma_{tr} = 1 - exp\left[-G\left(x - x_{tr}\right)\int_{x_{tr}}^{x}\frac{dx}{U}\right] \tag{1.4.12}$$

where $x_{tr}$ is the point where transition starts and

$$G = \left(\frac{3}{C^2}\right)\left(\frac{U^3}{\nu^2}\right)Re_{x_{tr}}^{-1.34} \tag{1.4.13}$$

where $Re_{x_{tr}}$is the Reynolds number with $x_{tr}$ and $U$ at that point. $C^2$ is constant and its value is

$$C^2 = 213\left(\log Re_{x_{tr}} - 4.7323\right) \tag{1.4.14}$$

for $2.4\times10^5 \leq Re_L \leq 2\times10^6$ with $Re_L$ being the Reynolds number with the undisturbed velocity $U_\infty$ and the chord length $L$ while, for greater $Re_L$, $C = 60$.

On the other hand, in the outer region the eddy viscosity is given by:

$$\left(\nu_t\right)_o = \alpha U\delta\gamma_{tr}\gamma. \tag{1.4.15}$$

Here $\alpha = 0.0168$ while $\gamma$ is an intermittency factor for the outer region expressed as:

$$\gamma = \left[1 + 5.5\left(\frac{y}{\delta}\right)^6\right]^{-1}. \tag{1.4.16}$$

The switching distance $y_c$ is defined as the point where $\left(\nu_t\right)_i$ and $\left(\nu_t\right)_o$ are equal.

## 1.5 Falkner-Skan Transformation

As already seen in section 1.3 boundary-layer thickness increases with increasing downstream distance for both laminar and turbulent flows. Thus transformed coordinates employing similarity variables are advantageous for the solution of boundary-layer equations since they can reduce and even eliminate the growth of transformed boundary-layer thickness. In this work the Falkner-Skan transformation was used. In this transformation the dimensionless similarity variable $\eta$ and the dimensionless stream function $f\left(x,\eta\right)$ are defined by[5]:

$$\eta=\sqrt{\frac{U}{\nu x}}y,\qquad f\left(x,\eta\right)=\frac{\psi\left(x,y\right)}{\sqrt{U\nu x}}\tag{1.5.1}$$

where $\psi\left(x,y\right)$ is the dimensional stream function. Considering also that

$$\xi=\frac{x}{L},\qquad w=\frac{U}{U_\infty},\qquad \tau=\frac{tU_\infty}{L}\tag{1.5.2}$$

and prime denoting the differentiation with respect to $\eta$, we can rewrite the boundary-layer momentum equation as:

$$(bf'')'+\frac{m+1}{2}ff''+m\left[1-\left(f'\right)^2\right]+m_3\left(1-f'\right)-\frac{1}{2}m_3f''=\xi\left(\frac{1}{w}\frac{\partial f'}{\partial\tau}+f'\frac{\partial f'}{\partial\xi}-f''\frac{\partial f}{\partial\xi}\right).\tag{1.5.3}$$

In the preceding equation $b$ is the viscous term, while $m$ and $m_3$ are dimensionless pressure gradient parameters and they are defined as:

$$b=1+\frac{\nu_t}{\nu},\qquad m=\frac{\xi}{w}\frac{\partial w}{\partial\xi},\qquad m_3=\frac{\xi}{w^2}\frac{\partial w}{\partial\tau}.\tag{1.5.4}$$

The velocity components through the boundary-layer $u$ and $v$ are related to the dimensionless stream function $f\left(\xi,\eta\right)$ by:

$$u=Uf',\qquad v=-\sqrt{U\nu x}\left[\frac{f}{\sqrt{Ux}}\frac{d}{dx}\sqrt{Ux}+\frac{\partial f}{\partial x}+f'\frac{\partial\eta}{\partial x}\right].\tag{1.5.5}$$

The transformed boundary conditions become:

$$\eta=0:\quad f=f'=0;\qquad \eta=\eta_e:\quad f'=1.\tag{1.5.6}$$

# Chapter 2

# Numerical Method

In the following chapter the numerical solution of the boundary-layer equations is presented. The coordinate system is shown in Fig. 2.0.1. The airfoil is divided by the leading edge in two plates having different distributions of velocity external to boundary-layer. The $x$ coordinate is set to be always parallel to the wall, while the $y$-axis is always perpendicular to it.

## 2.1 Computational Grid

After the blade is divided in two fictional plates and the stream-wise coordinate is set, the Falkner-Skan transformation is applied, as defined by Eq. 1.5.2. The computational grid is defined in nondimentional variables and the results are then transformed back to real variables.

The advantage of this strategy is shown in Fig. 2.1.1, where a typical Falkner-Skan

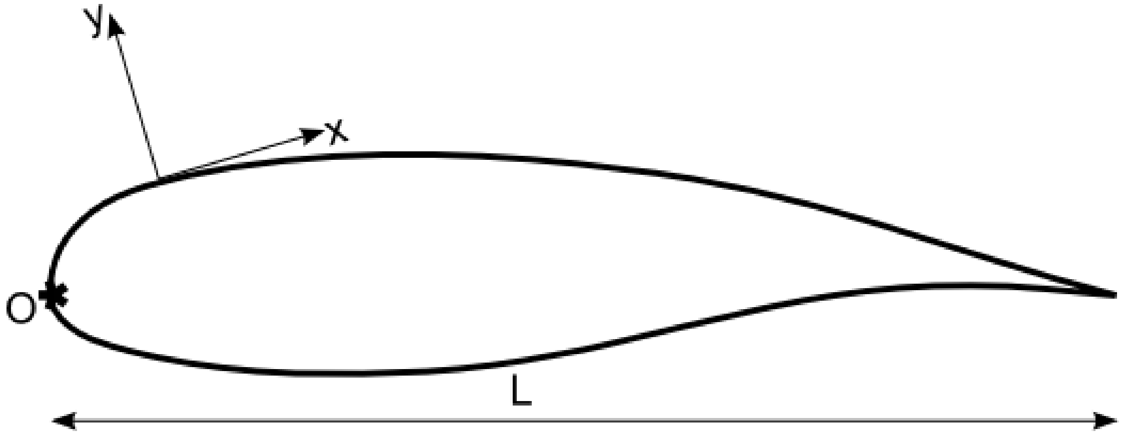

Figure 2.0.1: Coordinate system adopted

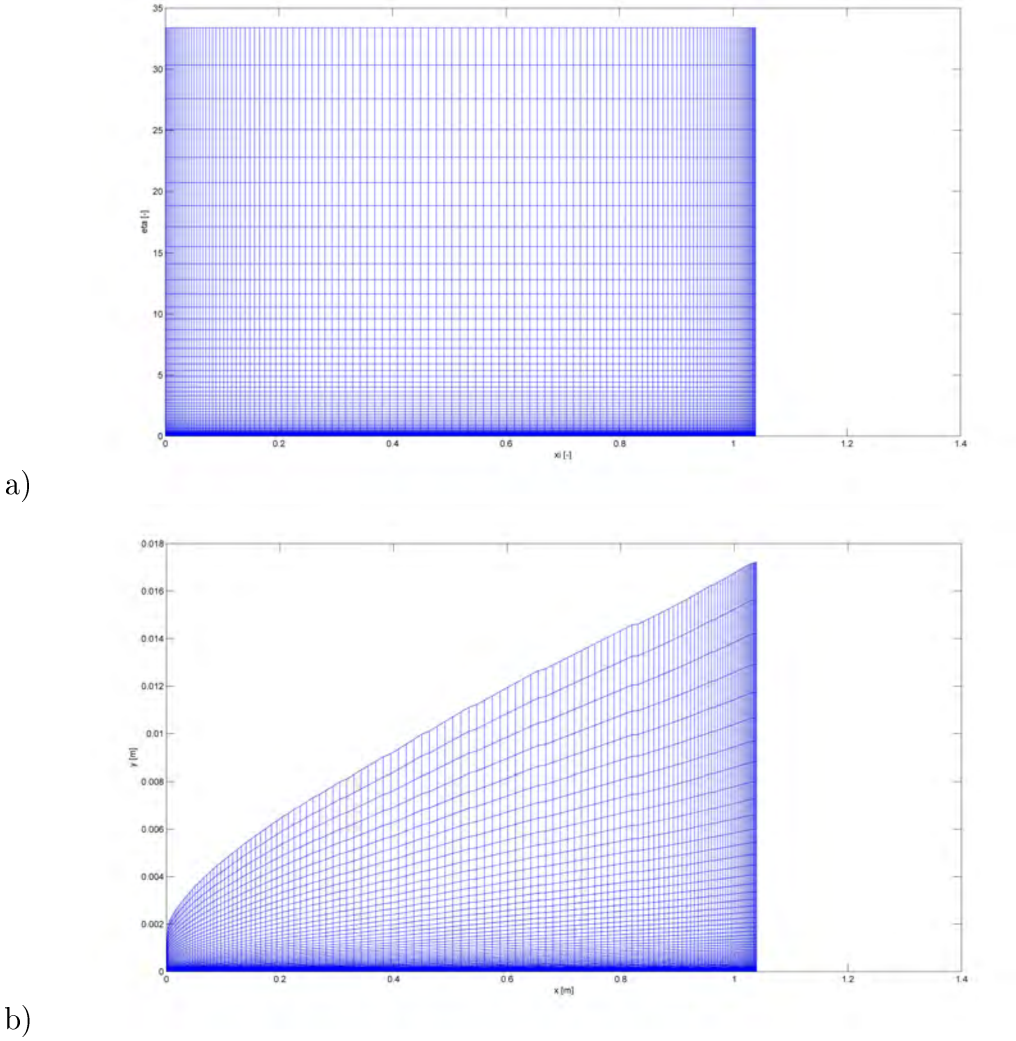

Figure 2.1.1: Comparison between transformed variables grid a) and real variables grid b)

grid is shown together with the actual grid. Dealing with transformed variables allows to define a rectangular grid which is actually a growing grid in real variables scaled by Eq. 1.5.1. The advantage to work on a rectangular grid it's amplified by the reduction of boundary-layer growth due to Falkner-Skan transformation, as already stated in section 1.5.

For what concerns stream-wise direction the adopted grid spacing is the same used by the potential flow solver while in wall-normal direction the spacing grid is defined as:

$$\eta_0 = 0, \tag{2.1.1a}$$

$$\eta_j = \eta_{j-1} + h_j \qquad for\ j = 1, 2, ..., J. \tag{2.1.1b}$$

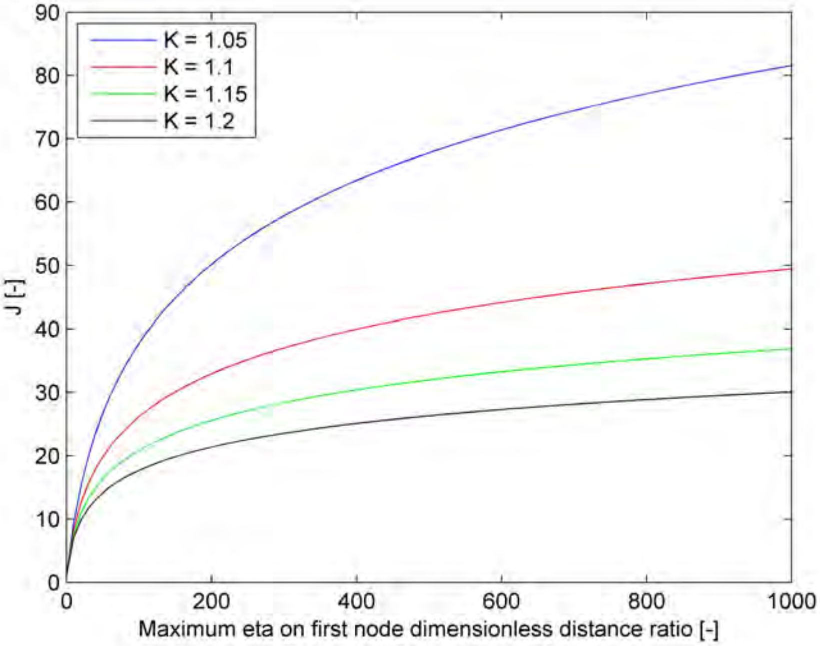

Figure 2.1.2: Dependence of $J$ by $\frac{\eta_{max}}{h_1}$ and $K$

In wall-normal direction a very efficient grid spacing is introduced that becomes finer while approaching the wall. This ensures a good accuracy of the derivatives of $f$, which change their value dramatically near the wall. The ratio of spacings between two subsequent intervals is constant, so that $h_j = Kh_{j-1}$, and it is called variable grid parameter. The distance to the $j$-th line is given by:

$$\eta_j = h_1 \frac{K^j - 1}{K - 1} \qquad for\ j = 1, 2, ..., J \tag{2.1.2}$$

where $h_1$ is the distance between the wall and the first grid point away from it. The total number of grid points in the wall-normal direction can be determined as

$$J = \frac{\ln\left[1 + (K-1)\frac{\eta_{max}}{h_1}\right]}{\ln K} + 1. \tag{2.1.3}$$

The influence of $K$ and $\frac{\eta_{max}}{h_1}$ on the total number of nodes in the direction perpendicular to the wall is shown in Fig. 2.1.2. In particular it is worth to notice that a higher variable grid parameter brings to a reduction of grid points, since it means a higher "growth rate" of nodes spacing.

Cebeci [5] suggests to set $K = 1.1$ and $h_1 = 0.01$, while the maximum value of transformed variable normal to the wall, $\eta_{max}$, can be fixed by the user.

The stagnation point, which divides the profile in two plates, is defined as the middle point between the two nodes of the potential method that show the lowest velocities.

## 2.2 Numerical Solution

The boundary-layer equations are solved at first in the steady case, to provide a solution for t = 0, and then unsteady. For both steady and unsteady equations the solution is provided by using the Keller box method, which is a finite-difference method.

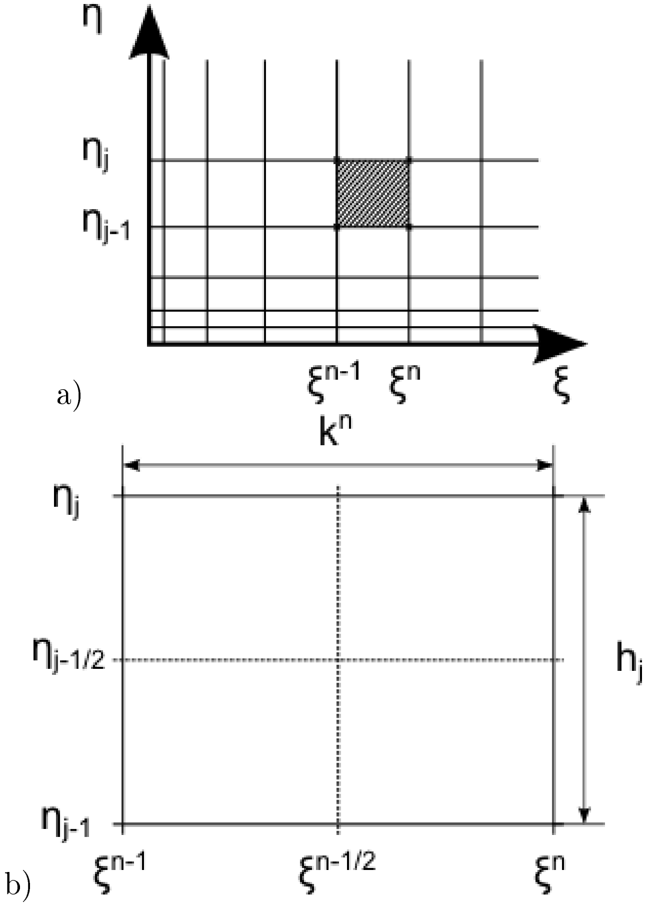

Figure 2.2.1: a) Rectangle for steady Keller box method b) Center scheme

### 2.2.1 Steady Solution

In order to solve the steady boundary-layer momentum equation with the Keller box method is useful to reduce the third order differential Eq. 1.5.3 to a system of three first order differential equations:

$$\frac{\partial f}{\partial \eta} = f' = u, \tag{2.2.1a}$$

$$\frac{\partial^2 f}{\partial \eta^2} = f'' = v, \tag{2.2.1b}$$

$$(bv)' + \frac{m+1}{2} f v + m\left(1-u^2\right) = \xi \left[\frac{\partial}{\partial \xi}\left(\frac{u^2}{2}\right) - v\frac{\partial f}{\partial \xi}\right]. \tag{2.2.1c}$$

Where $\frac{\partial}{\partial \xi}\left(\frac{u^2}{2}\right) = u\frac{\partial u}{\partial \xi}$.

The discretization of steady Keller box method is shown in Fig. 2.2.1. Eq. 2.2.1a and 2.2.1b are centered at the $n$-th position, which is the middle point of the right side of the sketch, while Eq. 2.2.1c is evaluated at the center of the rectangle.

So that the equations become:

$$\frac{f_j^n - f_{j-1}^n}{h_j} = \frac{u_j^n + u_{j-1}^n}{2} \equiv u_{j-\frac{1}{2}}^n, \tag{2.2.2a}$$

$$\frac{u_j^n - u_{j-1}^n}{h_j} = \frac{v_j^n + v_{j-1}^n}{2} \equiv v_{j-\frac{1}{2}}^n, \tag{2.2.2b}$$

$$\frac{1}{2}\left[\frac{(bv)_n^j - (bv)_{n-1}^j}{h_j} + \frac{(bv)_n^{j-1} - (bv)_{n-1}^{j-1}}{h_j}\right] + \frac{m^{n-\frac{1}{2}}+1}{2} f_{j-\frac{1}{2}}^{n-\frac{1}{2}} v_{j-\frac{1}{2}}^{n-\frac{1}{2}} + m^{n-\frac{1}{2}}\left[1-\left(u_{j-\frac{1}{2}}^{n-\frac{1}{2}}\right)^2\right] =$$

$$= \xi^{n-\frac{1}{2}}\left[FLARE\frac{\left(u_{j-\frac{1}{2}}^{n}\right)^2 - \left(u_{j-\frac{1}{2}}^{n-1}\right)^2}{2k_n} - v_{j-\frac{1}{2}}^{n-\frac{1}{2}}\frac{f_{j-\frac{1}{2}}^{n} - f_{j-\frac{1}{2}}^{n-1}}{k_n}\right]. \tag{2.2.2c}$$

Where $k^n = \xi^n - \xi^{n-1}$ while the $FLARE$ parameter refers to the Flügge-Lotz Reyhner approximation [7] and it's taken as unity when $u_j \geq 0$ and as zero whenever $u_j < 0$. The adoption of Flügge-Lotz Reyhner approximation is necessary to prevent calculation instabilities due to possible back-flow regions in the boundary-layer by dropping the $u$ stream-wise dependent term.

Eq. 2.2.2c can be rearranged to put in evidence known and unknown terms where $f_j^{n-1}$, $u_j^{n-1}$ and $v_j^{n-1}$ are supposed to be known for $0 < j < J$:

$$\frac{(bv)_j^n - (bv)_{j-1}^n}{h_j} + \alpha_1 f_{j-\frac{1}{2}}^n v_{j-\frac{1}{2}}^n - \alpha_2\left(u_{j-\frac{1}{2}}^n\right)^2 + \alpha^n\left(v_{j-\frac{1}{2}}^{n-1} f_{j-\frac{1}{2}}^n - f_{j-\frac{1}{2}}^{n-1} v_{j-\frac{1}{2}}^n\right) = R_{j-\frac{1}{2}}^{n-1}. \tag{2.2.3}$$

Where:

$$\alpha^n = \frac{\xi^{n-\frac{1}{2}}}{k_n}, \tag{2.2.4a}$$

$$\alpha_1 = 1 + \frac{m^{n-\frac{1}{2}}}{2} + \alpha^n, \tag{2.2.4b}$$

$$\alpha_2 = m^{n-\frac{1}{2}} + FLARE\alpha^n, \tag{2.2.4c}$$

$$R^{n-1}_{j-\frac{1}{2}} = -L^{n-1}_{j-\frac{1}{2}} + \alpha^n \left[ -FLARE \left( u^{n-1}_{j-\frac{1}{2}} \right)^2 + v^{n-1}_{j-\frac{1}{2}} f^{n-1}_{j-\frac{1}{2}} \right], \tag{2.2.4d}$$

$$L^{n-1}_{j-\frac{1}{2}} = \frac{(bv)^{n-1}_j - (bv)^{n-1}_{j-1}}{h_j} + \left( 1 + \frac{m^{n-\frac{1}{2}}}{2} \right) f^{n-1}_{j-\frac{1}{2}} + 2m^{n-\frac{1}{2}} \left[ 1 - \frac{\left( u^{n-1}_{j-\frac{1}{2}} \right)^2}{2} \right]. \tag{2.2.4e}$$

In these equations the boundary conditions become:

$$f^n_0 = u^n_0 = 0, \tag{2.2.5a}$$

$$u^n_J = 1. \tag{2.2.5b}$$

Eqs. 2.2.2 and 2.2.5 are a system of $3J+3$ nonlinear equations in $3J+3$ unknowns $\left(f^n_j, u^n_j, v^n_j\right)$ with $0 < j < J$ and Newton's method is applied to iteratively solve this system. Thus, $f$, $u$ and $v$ are approximated as:

$$f^{n,(r+1)}_j = f^{n,(r)}_j + \delta f^{n,(r)}_j, \qquad u^{n,(r+1)}_j = u^{n,(r)}_j + \delta u^{n,(r)}_j, \qquad v^{n,(r+1)}_j = v^{n,(r)}_j + \delta v^{n,(r)}_j. \tag{2.2.6}$$

Where $r$ is the iteration number and the initial values $r = 0$ are assumed equal to those at the $\xi^{n-1}$ station. From now on the superscript $n$ for the unknowns will be dropped for sake of simplicity.

Inserting the right-hand sides of the last three expressions in Eqs. 2.2.2 and dropping $\delta f^r_j$, $\delta u^r_j$ and $\delta v^r_j$ quadratic terms the following linear system is obtained:

$$\frac{f^r_j + \delta f^r_j - f^r_{j-1} - \delta f^r_{j-1}}{h_j} = \frac{u^r_j + \delta u^r_j + u^r_{j-1} + \delta u^r_{j-1}}{2}, \tag{2.2.7a}$$

$$\frac{u^r_j + \delta u^r_j - u^r_{j-1} - \delta u^r_{j-1}}{h_j} = \frac{v^r_j + \delta v^r_j + v^r_{j-1} + \delta v^r_{j-1}}{2}, \tag{2.2.7b}$$

$$
\begin{aligned}
&\frac{(bv)_j^r-(bv)_{j-1}^r}{h_j}+\frac{m^{n-\frac{1}{2}}+1}{2}f_{j-\frac{1}{2}}^r v_{j-\frac{1}{2}}^r-m^{n-\frac{1}{2}}\left(u_{j-\frac{1}{2}}^r\right)^2-\\
&\qquad-\frac{\xi^{n-\frac{1}{2}}}{k_n}\left[\left(u_{j-\frac{1}{2}}^r\right)^2-f_{j-\frac{1}{2}}^r v_{j-\frac{1}{2}}^r-f_{j-\frac{1}{2}}^r v_{j-\frac{1}{2}}^{n-1}+f_{j-\frac{1}{2}}^{n-1}v_{j-\frac{1}{2}}^r\right]+\frac{\delta v_j^r-\delta v_{j-1}^r}{h_j}+\\
&+\frac{1}{2}\frac{m^{n-\frac{1}{2}}+1}{2}\left(f_{j-\frac{1}{2}}^r\delta v_j^r+f_{j-\frac{1}{2}}^r\delta v_{j-1}^r+v_{j-\frac{1}{2}}^r\delta f_j^r+v_{j-\frac{1}{2}}^r\delta f_{j-1}^r\right)-m^{n-\frac{1}{2}}\left(u_{j-\frac{1}{2}}^r\delta u_j^r+u_{j-\frac{1}{2}}^r\delta u_{j-1}^r\right)-\\
&\quad-\frac{\xi^{n-\frac{1}{2}}}{k_n}\Bigg[u_{j-\frac{1}{2}}^r\delta u_j^r+u_{j-\frac{1}{2}}^r\delta u_{j-1}^r-\frac{1}{2}\Big(f_{j-\frac{1}{2}}^r\delta v_j^r+f_{j-\frac{1}{2}}^r\delta v_{j-1}^r+v_{j-\frac{1}{2}}^r\delta f_j^r+v_{j-\frac{1}{2}}^r\delta f_{j-1}^r+\\
&\qquad\qquad+v_{j-\frac{1}{2}}^{n-1}\delta f_j^r+v_{1-\frac{1}{2}}^{n-1}\delta f_{j-1}^r-f_{j-\frac{1}{2}}^{n-1}\delta v_j^r-f_{j-\frac{1}{2}}^{n-1}\delta v_{j-1}^r\Big)\Bigg]=R_{j-\frac{1}{2}}^{n-1}\ . \qquad (2.2.7c)
\end{aligned}
$$

Which can be summarized as:

$$\delta f_j^r-\delta f_{j-1}^r-\frac{h_j}{2}\left(\delta u_j^r+\delta u_{j-1}^r\right)=\left(r_1\right)_j, \qquad (2.2.8a)$$

$$\delta u_j^r-\delta u_{j-1}^r-\frac{h_j}{2}\left(\delta v_j^r+\delta v_{j-1}^r\right)=\left(r_3\right)_j, \qquad (2.2.8b)$$

$$\left(s_1\right)_j\delta v_j^r+\left(s_2\right)_j\delta v_{j-1}^r+\left(s_3\right)_j\delta f_j^r+\left(s_4\right)_j\delta f_{j-1}^r+\left(s_5\right)_j\delta u_j^r+\left(s_6\right)_j\delta u_{j-1}^r=\left(r_2\right)_j. \qquad (2.2.8c)$$

Where

$$\left(r_1\right)_j=-\left(f_j^r-f_{j-1}^r\right)+h_j u_{j-\frac{1}{2}}^r, \qquad (2.2.9a)$$

$$\left(r_3\right)_j=-\left(u_j^r-u_{j-1}^r\right)+h_j v_{j-\frac{1}{2}}^r, \qquad (2.2.9b)$$

$$\left(r_2\right)_j=R_{j-\frac{1}{2}}^{n-1}-\left[\frac{(bv)_j^r-(bv)_{j-1}^r}{h_j}+\alpha_1 f_{j-\frac{1}{2}}^r v_{j-\frac{1}{2}}^r-\alpha_2\left(u_{j-\frac{1}{2}}^r\right)^2+\alpha_2\left(f_{j-\frac{1}{2}}^r v_{j-\frac{1}{2}}^{n-1}-f_{j-\frac{1}{2}}^{n-1}v_{j-\frac{1}{2}}^r\right)\right] \qquad (2.2.9c)$$

and

$$\left(s_1\right)_j=\frac{1}{h_j}+\frac{\alpha_1}{2}f_{j-\frac{1}{2}}^r-\frac{\alpha^n}{2}f_{j-\frac{1}{2}}^{n-1}, \qquad (2.2.10a)$$

$$\left(s_2\right)_j=-\frac{1}{h_j}+\frac{\alpha_1}{2}f_{j-\frac{1}{2}}^r-\frac{\alpha^n}{2}f_{j-\frac{1}{2}}^{n-1}, \qquad (2.2.10b)$$

$$\left(s_3\right)_j=\frac{\alpha_1}{2}v_{j-\frac{1}{2}}^r+\frac{\alpha^n}{2}v_{j-\frac{1}{2}}^{n-1}, \qquad (2.2.10c)$$

$$\left(s_4\right)_j=\frac{\alpha_1}{2}v_{j-\frac{1}{2}}^r+\frac{\alpha^n}{2}v_{j-\frac{1}{2}}^{n-1}, \qquad (2.2.10d)$$

$$\left(s_5\right)_j=-\alpha_2 u_{j-\frac{1}{2}}^r, \qquad (2.2.10e)$$

$$\left(s_6\right)_j=-\alpha_2 u_{j-\frac{1}{2}}^r. \qquad (2.2.10f)$$

This new system needs three new boundary conditions, they are:

$$\delta f_0^r = \delta u_0^r = \delta u_J^r = 0. \tag{2.2.11}$$

The problem can be expressed in matrix-vector form

$$A\overrightarrow{\delta} = \overrightarrow{r} \tag{2.2.12}$$

Where the coefficients matrix $A$ shows a block tridiagonal structure. In detail Eq. (2.2.12) is:

$$\begin{bmatrix} A_0 & C_0 & & & & & \\ B_1 & A_1 & C_1 & & & & \\ & \cdot & \cdot & \cdot & & & \\ & & \cdot & \cdot & \cdot & & \\ & & B_j & A_j & C_j & & \\ & & & \cdot & \cdot & \cdot & \\ & & & & \cdot & \cdot & \cdot \\ & & & & B_{J-1} & A_{J-1} & C_{J-1} \\ & & & & & B_J & A_J \end{bmatrix} \begin{bmatrix} \overrightarrow{\delta_0} \\ \overrightarrow{\delta_1} \\ \cdot \\ \cdot \\ \overrightarrow{\delta_j} \\ \cdot \\ \cdot \\ \overrightarrow{\delta_{J-1}} \\ \overrightarrow{\delta_J} \end{bmatrix} = \begin{bmatrix} \overrightarrow{r_0} \\ \overrightarrow{r_1} \\ \cdot \\ \cdot \\ \overrightarrow{r_j} \\ \cdot \\ \cdot \\ \overrightarrow{r_{J-1}} \\ \overrightarrow{r_J} \end{bmatrix}. \tag{2.2.13}$$

The three-dimensional block vectors $\overrightarrow{\delta_j}$ and $\overrightarrow{r_j}$ are:

$$\overrightarrow{\delta_j} = \begin{bmatrix} \delta f_j \\ \delta u_j \\ \delta v_j \end{bmatrix}, \qquad \overrightarrow{r_j} = \begin{bmatrix} (r_1)_j \\ (r_2)_j \\ (r_3)_j \end{bmatrix}, \qquad 0 \leq j \leq J \tag{2.2.14}$$

while the $3 \times 3$ matrices $A_j$, $B_j$ and $C_j$ are defined by:

$$A_0 = \begin{bmatrix} 1 & 0 & 0 \\ 0 & 1 & 0 \\ 0 & -1 & -\frac{h_1}{2} \end{bmatrix}, \tag{2.2.15a}$$

$$A_j = \begin{bmatrix} 1 & -\frac{h_j}{2} & 0 \\ (s_3)_j & (s_5)_j & (s_1)_j \\ 0 & -1 & -\frac{h_{j+1}}{2} \end{bmatrix} \quad 1 \leq j \leq J-1 \qquad A_J = \begin{bmatrix} -1 & -\frac{h_J}{2} & 0 \\ (s_3)_J & (s_5)_J & (s_1)_J \\ 0 & 1 & 0 \end{bmatrix}, \tag{2.2.15b}$$

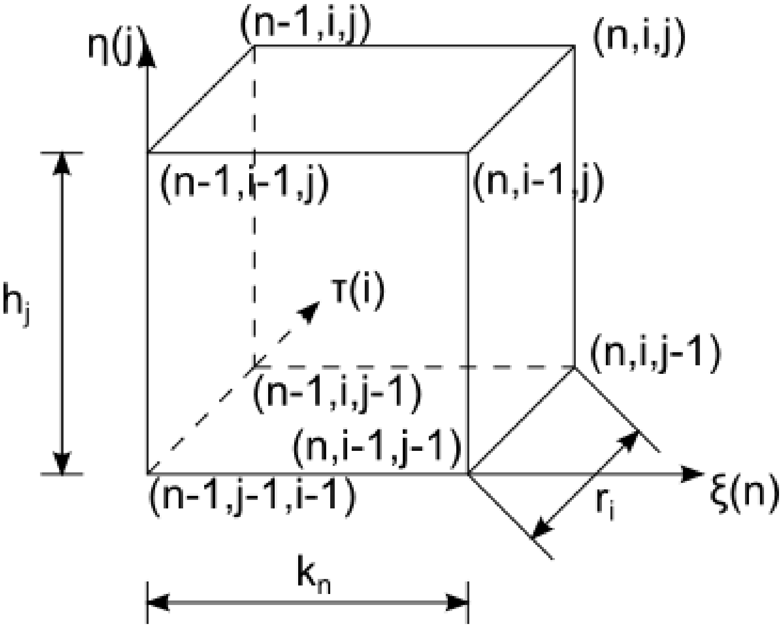

Figure 2.2.2: Keller box cube for the difference equations for two-dimensional unsteady flows

$$B_j = \begin{bmatrix} -1 & -\frac{h_j}{2} & 0 \\ (s_4)_j & (s_6)_j & (s_2)_j \\ 0 & 0 & -\frac{h_{j+1}}{2} \end{bmatrix} \quad 1 \leq j \leq J \qquad C_j = \begin{bmatrix} 0 & 0 & 0 \\ 0 & 0 & 0 \\ 0 & 1 & -\frac{h_{j+1}}{2} \end{bmatrix} \quad 0 \leq j \leq J-1. \tag{2.2.15c}$$

This way to arrange the system of equations prevents matrix $A_0$ from being singular. It's also worth to note that the first, second and last row in Eq. (2.2.13) correspond to the boundary conditions (2.2.11), this brings to $(r_1)_0 = (r_2)_0 = (r_3)_J = 0$ to ensure that the boundary conditions are fulfilled. After solution is converged the whole system is shifted to the next $\xi$ station until, eventually, boundary-layer separation occurs and no converge is achieved.

### 2.2.2 Unsteady solution

The two-dimensional unsteady flow with no separation has many similarities with three-dimensional cross-flow steady problem since time can be associated with the direction of a main stream with unit velocity component.

The discretization of Keller box method in this case, considering what has just been said about similarities between two and three-dimensional flow, is shown in Fig. 2.2.2. In the discretized net cube $\tau$ is the non-dimensional time variable defined by Eq. (1.5.2). Looking at this figure it is also clear the reason why the Keller method is also called the "box" method.

In Fig. 2.2.2 the unknowns are only the $(n, i, j)$ and $(n, i, j-1)$ values, this means that initial conditions are necessary both in the $(\xi, \eta)$ and $(\tau, \eta)$ planes. Since the aim of this work isn't to investigate the starting of motion, the initial conditions in the $(\xi, \eta)$ plane are obtained by solving the steady-state equations with the instantaneous external velocity at $t = 0$ using the procedure described in the preceding subsection. For what concerns the $(\tau, \eta)$ plane a quasi-steady approach is applied, it implies that for the first $\xi$ node after the stagnation point it is possible to use the same values of the preceding time-step. The assumption of quasi-steady flow in the vicinity of the stagnation point is legit for unsteady flows with low frequency.

To solve Eq. (1.5.3) it's again necessary to reduce it to a first-order system by introducing the new variables $u(\xi, \eta, \tau)$ and $v(\xi, \eta, \tau)$:

$$f' = u, \tag{2.2.16a}$$

$$f'' = u' = v, \tag{2.2.16b}$$

$$(bv)' + \frac{m+1}{2} f v + m\left(1 - u^2\right) + m_3 (1-u) - \frac{m_3}{2} v = \xi \left[ \frac{1}{w} \frac{\partial u}{\partial \tau} + \frac{\partial}{\partial \xi}\left(\frac{u^2}{2}\right) - v \frac{\partial f}{\partial \xi} \right]. \tag{2.2.16c}$$

Again the first two equations are averaged about the midpoint between the two unknowns $\left(\xi^n, \tau^i, \eta_{j-\frac{1}{2}}\right)$:

$$\frac{f_j^{n,i} - f_{j-1}^{n,i}}{h_j} = \frac{u_j^{n,i} + u_{j-1}^{n,i}}{2} = u_{j-\frac{1}{2}}^{n,i}, \tag{2.2.17a}$$

$$\frac{u_j^{n,i} - u_{j-1}^{n,i}}{h_j} = \frac{v_j^{n,i} - v_{j-1}^{n,i}}{2} = v_{j-\frac{1}{2}}^{n,i}. \tag{2.2.17b}$$

On the other side Eq. (2.2.16c) is approximated centering all quantities at the center of the cube $\left(\xi^{n-\frac{1}{2}}, \tau^{i-\frac{1}{2}}, \eta_{j-\frac{1}{2}}\right)$ defining:

$$\bar{q}_j = q_j^{n-\frac{1}{2}, i-\frac{1}{2}} = \frac{1}{4}\left(q_j^{n,i} + q_j^{n,i-1} + q_j^{n-1,i} + q_j^{n-1,i-1}\right) = \frac{1}{4}\left(q_j^{n,i} + q_j^{234}\right), \tag{2.2.18a}$$

$$\bar{q}_{j-\frac{1}{2}} = \frac{1}{2}\left(\bar{q}_j + \bar{q}_{j-1}\right) = \frac{1}{4}\left(q_{j-\frac{1}{2}}^{n,i} + q_{j-\frac{1}{2}}^{234}\right). \tag{2.2.18b}$$

Where $q_j^{234} = q_j^{n,i-1} + q_j^{n-1,i} + q_j^{n-1,i-1}$ is the sum of $q_j$ values at three of the four corners of the $\eta_j$ face of the box.

With this notation the finite-difference approximated momentum equation is:

$$\frac{\left(\bar{bv}\right)_j - \left(\bar{bv}\right)_{j-1}}{h_j} + \frac{1}{2}\left(\bar{m}+1\right)\bar{f}_{j-\frac{1}{2}}\bar{v}_{j-\frac{1}{2}} + \bar{m}\left[1 - \left(\bar{u}_{j-\frac{1}{2}}\right)^2 + \bar{m}_3\left(1 - \bar{u}_{j-\frac{1}{2}}\right) - \frac{\bar{m}_3}{2}\bar{v}_{j-\frac{1}{2}}\right] =$$
$$= \xi^{n-\frac{1}{2}}\left[\frac{1}{\bar{w}}\frac{\bar{u}^i_{j-\frac{1}{2}} - \bar{u}^{i-1}_{j-\frac{1}{2}}}{r_i} + \frac{\left(\bar{u}^n_{j-\frac{1}{2}}\right)^2 - \left(\bar{u}^{n-1}_{j-\frac{1}{2}}\right)^2}{2k_n} - \bar{v}_{j-\frac{1}{2}}\frac{\bar{f}^n_{j-\frac{1}{2}} - \bar{f}^{n-1}_{j-\frac{1}{2}}}{k_n}\right] \quad (2.2.19)$$

where

$$\bar{q}^n_{j-\frac{1}{2}} = q^{n,i-\frac{1}{2}}_{j-\frac{1}{2}} = \frac{1}{4}\left(q^{n,i}_j + q^{n,i-1}_j + q^{n,i}_{j-1} + q^{n,i-1}_{j-1}\right) = \frac{1}{2}\left(q^{n,i}_{j-\frac{1}{2}} + q^{n,i-1}_{j-\frac{1}{2}}\right), \quad (2.2.20a)$$

$$\bar{q}^i_{j-\frac{1}{2}} = q^{n-\frac{1}{2},i}_{j-\frac{1}{2}} = \frac{1}{4}\left(q^{n,i}_j + q^{n-1,i}_j + q^{n,i}_{j-1} + q^{n-1,i}_{j-1}\right) = \frac{1}{2}\left(q^{n,i}_{j-\frac{1}{2}} + q^{n-1,i}_{j-\frac{1}{2}}\right), \quad (2.2.20b)$$

$$\bar{m} = m^{n-\frac{1}{2},i-\frac{1}{2}} = \frac{1}{4}\left(m^{n,i} + m^{234}\right), \quad (2.2.20c)$$

$$\bar{m}_3 = m_3^{n-\frac{1}{2},i-\frac{1}{2}} = \frac{1}{4}\left(m_3^{n,i} + m_3^{234}\right), \quad (2.2.20d)$$

$$\bar{w} = w^{n-\frac{1}{2},i-\frac{1}{2}} = \frac{1}{4}\left(w^{n,i} + w^{234}\right). \quad (2.2.20e)$$

Considering Eqs. (2.2.18) and (2.2.20) and rearranging to highlight known and unknown terms Eq. (2.2.19) can be written in a summarized form similar to Eq. (2.2.3) for steady flow:

$$\frac{(bv)^{n,i}_j - (bv)^{n,i}_{j-1}}{h_j} + \left(\frac{\alpha_1}{4} + \frac{\alpha^n}{2}\right) f^{n,i}_{1-\frac{1}{2}} v^{n,i}_{1-\frac{1}{2}} - \alpha^2\left(u^{n,i}_{j-\frac{1}{2}}\right)^2 - \left(\alpha_3 + \frac{\bar{m}}{2}u^{234}_{j-\frac{1}{2}} - \frac{\xi^{n-\frac{1}{2}}}{k_n}u^{n,i-1}_{j-\frac{1}{2}}\right)u^{n,i}_{j-\frac{1}{2}} +$$
$$+ \left(\frac{\alpha_1}{4}f^{234}_{j-\frac{1}{2}} - \alpha_4\right)v^{n,i}_{j-\frac{1}{2}} + \left(\frac{\alpha_1}{4} + \frac{\alpha^n}{2}\right)v^{234}_{j-\frac{1}{2}}f^{n,i}_{j-\frac{1}{2}} = -\beta_1 \quad (2.2.21)$$

where $\alpha^n$ is given by Eq. (2.2.4a) and

$$\alpha_1 = \frac{1+\bar{m}}{2}, \quad (2.2.22a)$$

$$\alpha_2 = \frac{\bar{m}}{4} + \frac{\alpha^n}{2}, \quad (2.2.22b)$$

$$\alpha_3 = \bar{m}_3 + 2\frac{\xi^{n-\frac{1}{2}}}{\bar{w}r_i}, \quad (2.2.22c)$$

$$\alpha_4 = \frac{\bar{m}_3}{2} - \frac{\alpha^n}{2}\left(f^{n,i-1}_{j-\frac{1}{2}} - 2\bar{f}^{n-1}_{j-\frac{1}{2}}\right), \quad (2.2.22d)$$

$$\beta_1 = \frac{(bv)_j^{234} - (bv)_{j-1}^{234}}{h_j} + \frac{\alpha_1}{4} f_{j-\frac{1}{2}}^{234} v_{j-\frac{1}{2}}^{234} + \frac{\bar{m}}{4}\left[1 - \left(u_{j-\frac{1}{2}}^{234}\right)^2\right] + \bar{m}_3\left(1 - u_{j-\frac{1}{2}}^{234} - v_{j-\frac{1}{2}}^{234}\right) -$$
$$- \alpha^n \left[\frac{k_n}{4\bar{w}r_i}\left(8u_{j-\frac{1}{2}}^{n-1,i} - \bar{u}_{j-\frac{1}{2}}^{i-1}\right) + \frac{1}{2}\left(u_{j-\frac{1}{2}}^{n,i-1}\right)^2 - 2\left(\bar{u}_{j-\frac{1}{2}}^{n-1}\right)^2 - \frac{1}{2} v_{j-\frac{1}{2}}^{234} f_{j-\frac{1}{2}}^{n,i-1} + v_{j-\frac{1}{2}}^{234} \bar{f}_{j-\frac{1}{2}}^{n-1}\right]. \tag{2.2.22e}$$

The boundary conditions for the unsteady flow are similar to the steady ones where the superscript $i$ is added to take into account the time variable, this brings to:

$$f_0^{n,i} = u_0^{n,i} = 0, \tag{2.2.23a}$$

$$u_J^{n,i} = 1. \tag{2.2.23b}$$

The system of equations is again linearized applying Newton's method. If equations and unknowns are written in the same order of the steady flow the linearized equations for Eqs. (2.2.17) become identical to Eqs. (2.2.8a) and (2.2.8b). On the other hand linearized Eq. (2.2.21) is identical to Eq. (2.2.8c) with different coefficients, which are:

$$(r_2)_j = -\left\{4\left[\frac{(\bar{bv})_j^r - (\bar{bv})_j^r}{h_j} + \alpha_1 \bar{f}_{j-\frac{1}{2}}^r \bar{v}_{j-\frac{1}{2}}^r + \bar{m}\left(1 - \left(\bar{u}_{j-\frac{1}{2}}^r\right)^2\right)\right] + 2\bar{m}_3\left[\bar{v}_{j-\frac{1}{2}}^r + 2\left(1 - \bar{u}_{j-\frac{1}{2}}^r\right)\right] -\right.$$
$$\left. -2\alpha^n\left[\left(\bar{u}_{j-\frac{1}{2}}^{n,(r)}\right)^2 - \left(\bar{u}_{j-\frac{1}{2}}^{n-1,(r)}\right)^2 - 2\bar{u}_{j-\frac{1}{2}}\left(\bar{f}_{j-\frac{1}{2}}^{n,(r)} - \bar{f}_{j-\frac{1}{2}}^{n-1,(r)}\right)\right] - 4\frac{\xi^{n-\frac{1}{2}}}{\bar{w}r_i}\left(\bar{u}_{j-\frac{1}{2}}^{i,(r)} - \bar{u}_{j-\frac{1}{2}}^{i-1,(r)}\right)\right\}, \tag{2.2.24a}$$

$$(s_1)_j = \frac{b_j^r}{h_j} + \frac{\alpha_1}{2}\bar{f}_{j-\frac{1}{2}}^r + \frac{\bar{m}_3}{4} + \frac{\alpha^n}{2}\left(\bar{f}_{j-\frac{1}{2}}^{n,(r)} - \bar{f}_{j-\frac{1}{2}}^{n-1,(r)}\right), \tag{2.2.24b}$$

$$(s_2)_j = -\frac{b_{j-1}^r}{h_j} + \frac{\alpha_1}{2}\bar{f}_{j-\frac{1}{2}}^r + \frac{\bar{m}_3}{4} + \frac{\alpha^n}{2}\left(\bar{f}_{j-\frac{1}{2}}^{n,(r)} - \bar{f}_{j-\frac{1}{2}}^{n-1,(r)}\right), \tag{2.2.24c}$$

$$(s_3)_j = (\alpha_1 + \alpha^n)\,\bar{v}_{j-\frac{1}{2}}^r, \tag{2.2.24d}$$

$$(s_4)_j = (\alpha_1 + \alpha^n)\,\bar{v}_{j-\frac{1}{2}}^r, \tag{2.2.24e}$$

$$(s_5)_j = -\bar{m}\bar{u}_{j-\frac{1}{2}}^r - \alpha^n \bar{u}_{j-\frac{1}{2}}^{n,(r)} - \frac{\alpha_3}{2}, \tag{2.2.24f}$$

$$(s_6)_j = -\bar{m}\bar{u}_{j-\frac{1}{2}}^r - \alpha^n \bar{u}_{j-\frac{1}{2}}^{n,(r)} - \frac{\alpha_3}{2}. \tag{2.2.24g}$$

The matrix-vectors formulation is the same for the steady case and so are boundary conditions.

When convergence is achieved the whole system is shifted to the next $\xi$ node until both the upper and lower fictional plates are completely solved for the present time step, then the all process is repeated for the next one.

After solution has converged for all $\xi$ and $\tau$ stations velocity profiles are computed using Eqs. (1.5.5). With these results it is possible to calculate boundary-layer characteristics such as boundary-layer thickness and displacement thickness which are used for the viscous-inviscid interaction method.

# Chapter 3

# Results and Discussion

In this section the results obtained with the method developed in this work will be compared with some analytical models and CFD simulations. At first were runned two simulations of flow over a flat plate (a fully laminar and a fully turbulent one) to have a first validation of the method and the turbulence model in the most simple case possible. Then, in order to test the method when pressure gradients occur, a highly cambered profile with great thickness variations was simulated and compared with CFD results. Finally the last step have been to validate the complete code with an unsteady simulation.

## 3.1 Flat Plate

The most simple test case for a numerical method such as the one described here is a steady flow over a flat plate (i. e. with no pressure gradient over it). Nevertheless this simple situation can highlight, as it will be shown, some important features and, eventually, flaws of the present method.

At first a fully laminar flow with $U = 5\,\mathrm{m/s}$ over a flat plate 5 meters long was simulated and compared with the Pohlhausen model described in subsection 1.3.1. The results show a perfect matching between the two displacement thicknesses an a small difference for what concerns boundary-layer thickness (Fig. 3.1.1).

The explanation of the difference between boundary-layer thicknesses, which is small but spreading along the plate, could be that for the Keller box method the $\delta_{99}$ is considered (i. e. at which distance from the wall $u = 0.99U$) while for the Pohlhausen model BL thickness represents $\delta_{100}$ ($u = U$). What has just been said is confirmed by the analysis of the velocity profiles shown in Fig. 3.1.2a) and enlarged in Fig. 3.1.2b). It is clearly visible that the two velocity profiles match completely, and this leads to

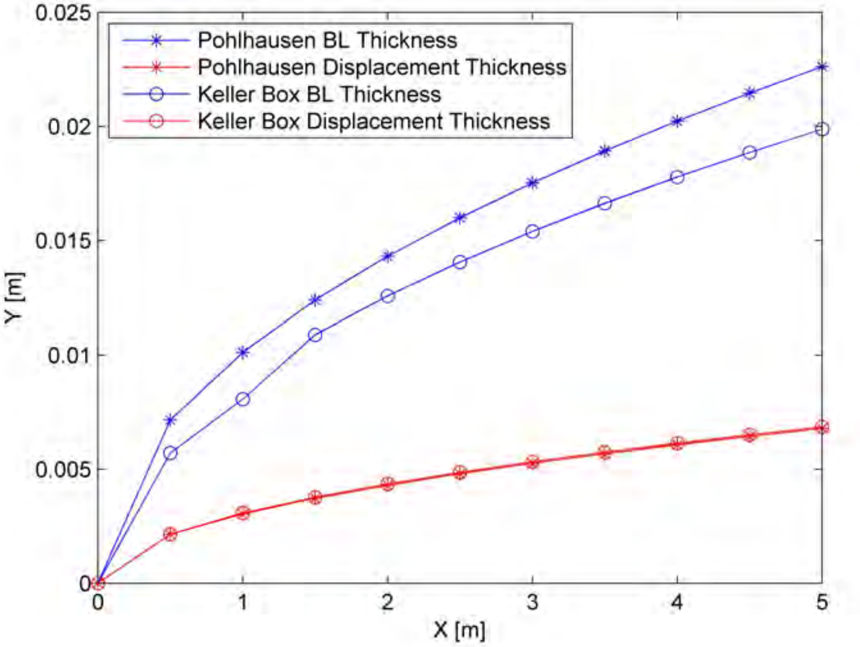

Figure 3.1.1: Comparison between Pohlhausen (star) and Keller box (circle) boundary-layer thickness (blue) and displacement thickness (red) over a flat plate 5 meters long with fully laminar flow

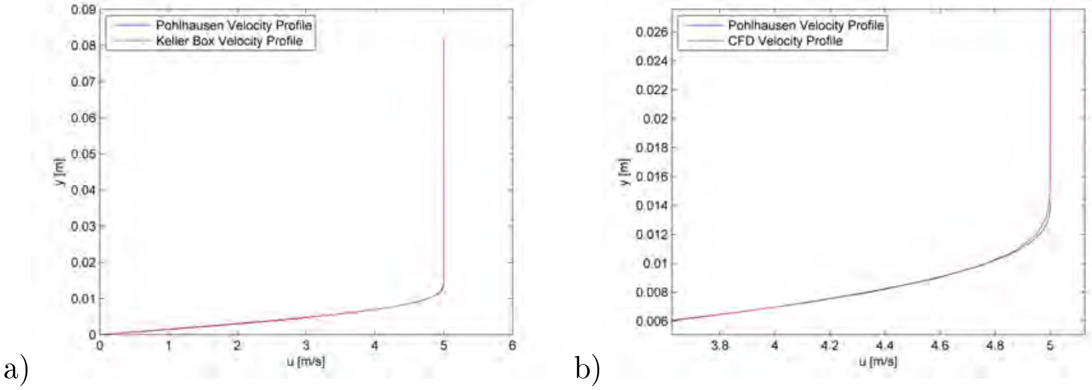

Figure 3.1.2: Comparison between velocity profiles obtained by Pohlhausen (blue) and Keller box (red) method on a flat plate 5 meters long at $x = 2\,\mathrm{m}$ with fully laminar flow a) and enlargement of the edge of boundary-layer b)

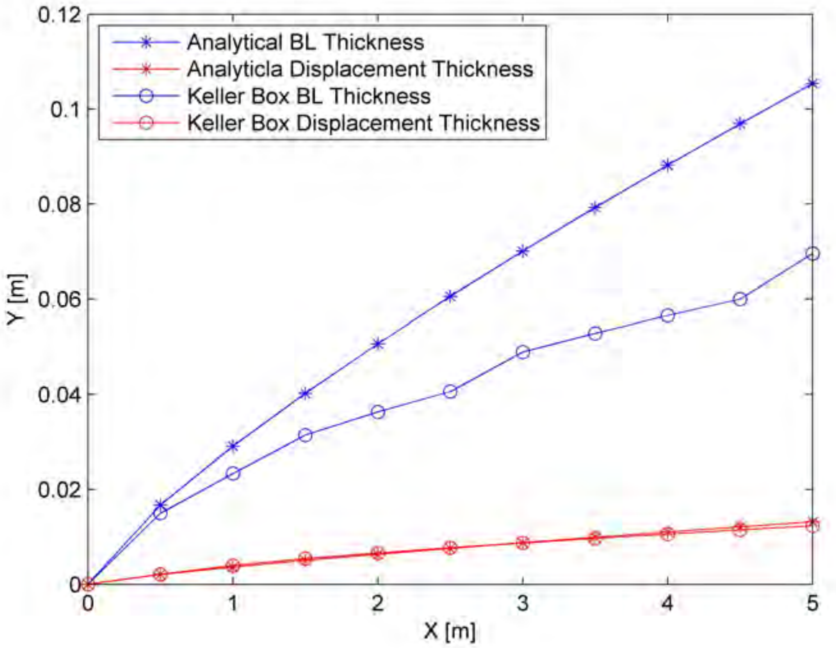

Figure 3.1.3: Comparison between Pohlhausen (star) and Keller box (circle) boundary-layer thickness (blue) and displacement thickness (red) over a flat plate 5 meters long with fully turbulent flow

the only conclusion that the difference in Fig. 3.1.1 is due to a different definition of boundary-layer thickness for the two methods.

In order to test the turbulence model described in subsection 1.4.1 a fully turbulent flat plate was simulated (all the other parameters were identical to the previous simulation) and the results were compared with those obtained by the analytical model of subsection 1.3.2. Boundary-layer and displacement thickness computed with both the two methods are plotted in Fig. 3.1.3. Here again we have a perfect accordance for what concerns displacement thickness, while a spreading difference between boundary-layer thicknesses can be noticed. The gap here by the way seems to be too large to be justified by the difference between $\delta_{99}$ and $\delta_{100}$, which is still present. Looking at the velocity profiles of Fig. 3.1.4 the reason of this bigger gap becomes obvious. The Keller box velocity profile indeed reaches the external velocity value before than the analytical model. This difference in velocity profile slopes is due to the turbulence model adopted. By the way, in order to make a good viscous-inviscid interaction method, the important parameter is the displacement thickness. $\delta_1$ indeed is the parameter which tells us how much the streamlines are displaced from the wall because of the boundary-layer (section 1.1) and the turbulence model described in subsection 1.4.1 makes it match perfectly.

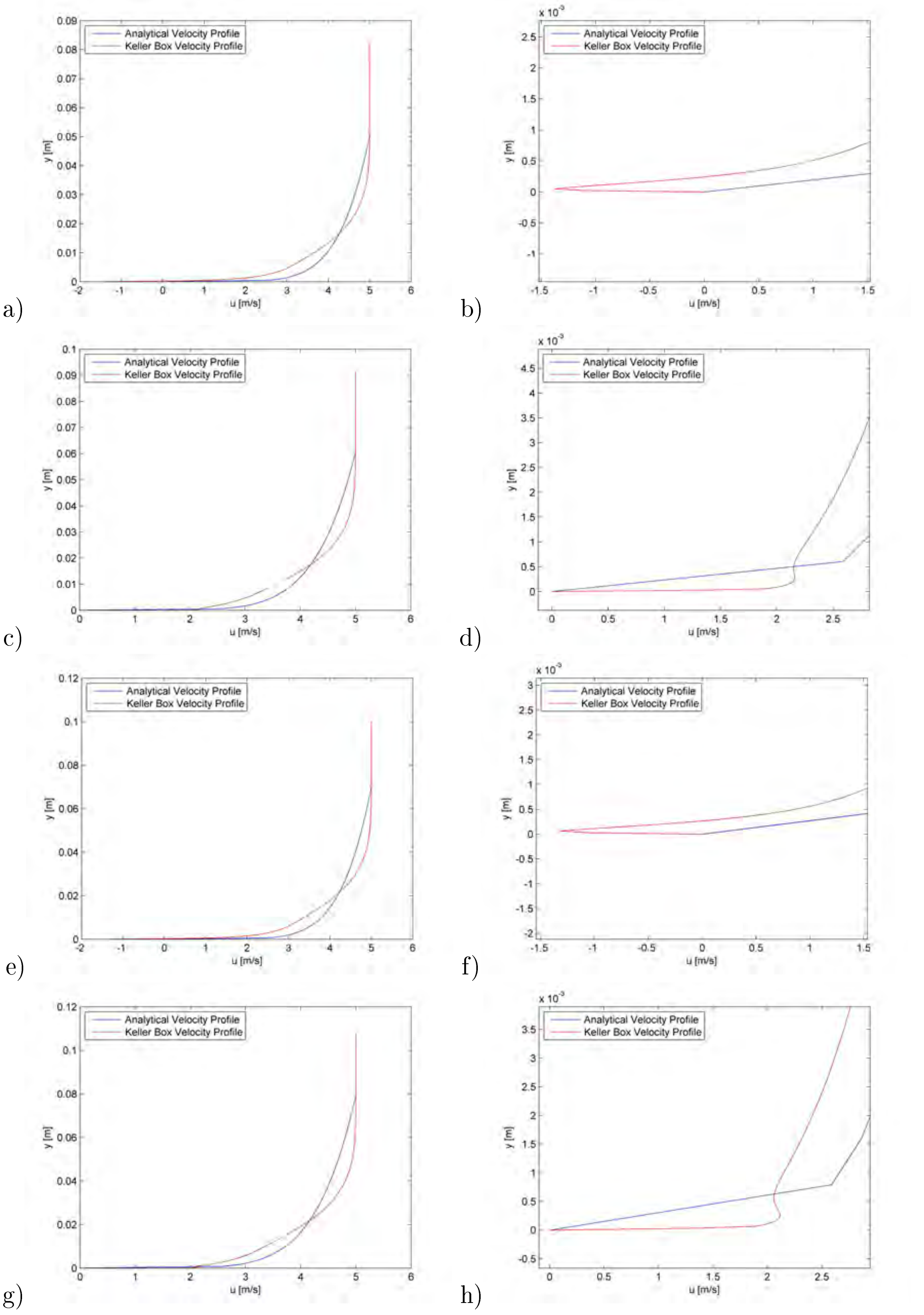

Figure 3.1.4: Comparison between velocity profiles obtained by analytical (blue) and Keller box (red) method on a flat plate 5 meters long and enlargement of the region closest to the wall at $x = 2\,\mathrm{m}$ a) b), $x = 2.5\,\mathrm{m}$ c) d), $x = 3\,\mathrm{m}$ e) f) and $x = 3.5\,\mathrm{m}$ g) h) with fully turbulent flow.

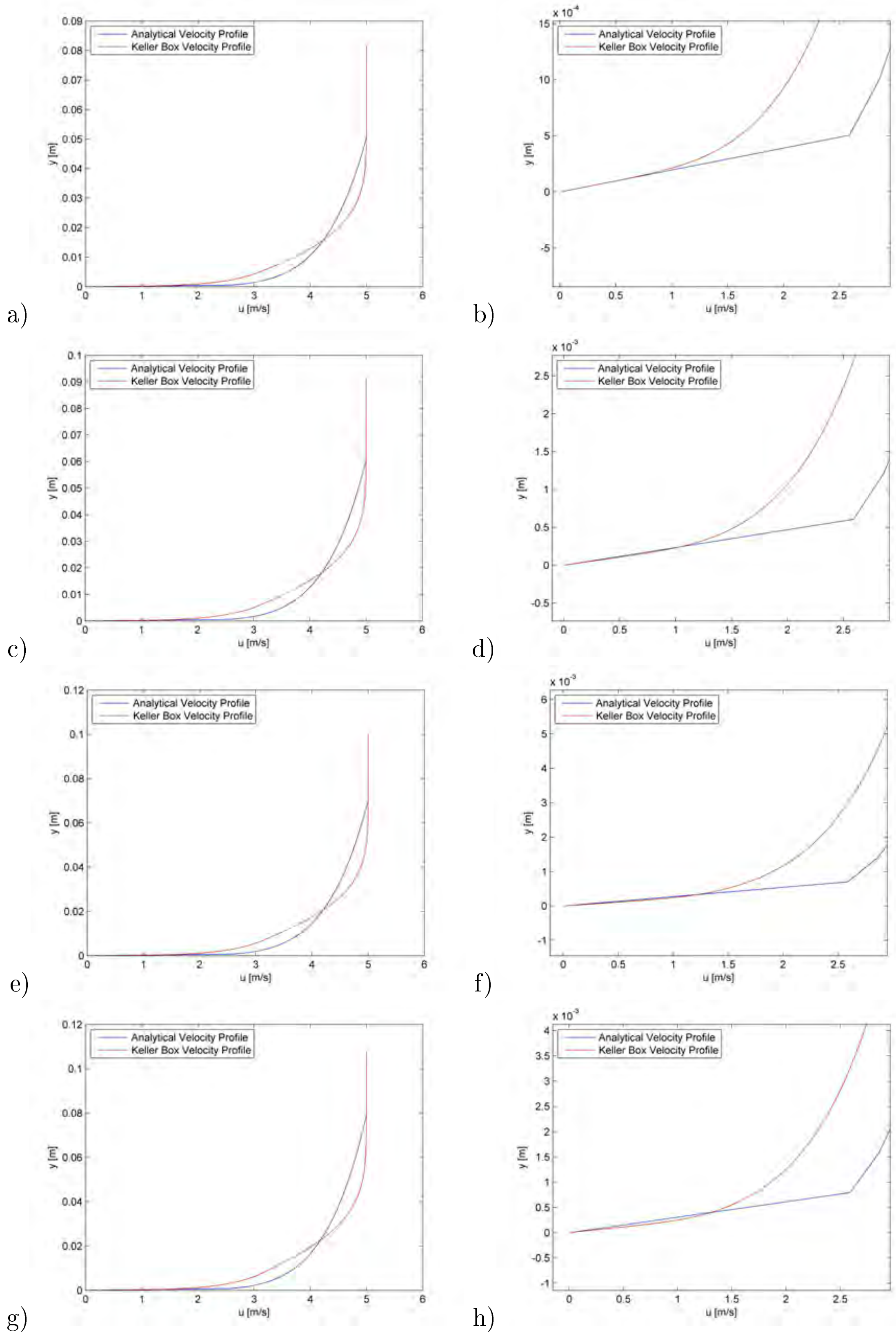

Figure 3.1.5: Comparison between velocity profiles obtained by analytical (blue) and Keller box (red) method on a flat plate 5 meters long and enlargement of the region closest to the wall at $x = 2\,\mathrm{m}$ a) b), $x = 2.5\,\mathrm{m}$ c) d), $x = 3\,\mathrm{m}$ e) f) and $x = 3.5\,\mathrm{m}$ g) h) with fully turbulent flow after the filtering correction was applied.

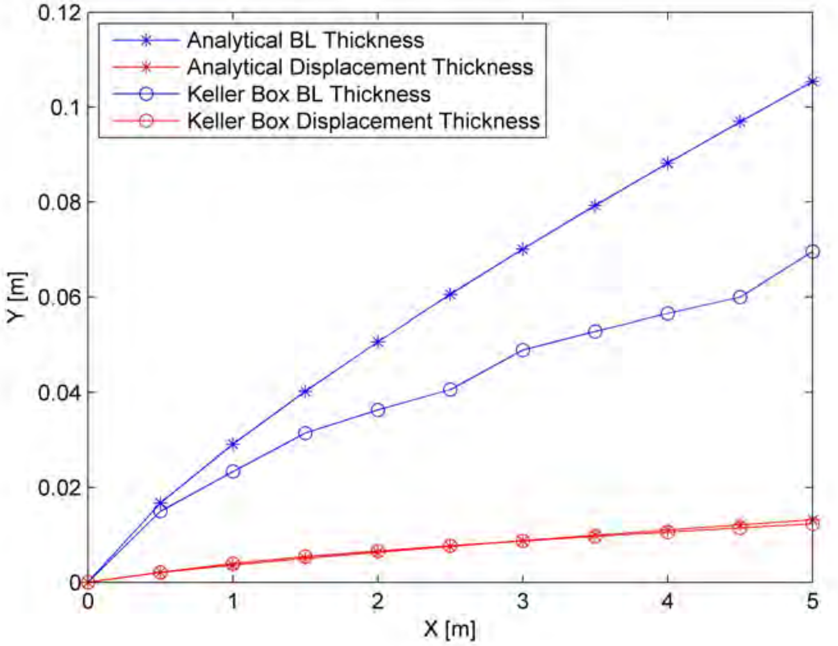

Figure 3.1.6: Comparison between analytical (star) and Keller box (circle) boundary-layer thickness (blue) and displacement thickness (red) over a flat plate with fully turbulent flow after correction was applied

Looking at Fig. 3.1.4 an important flaw of this method can be noticed. In Figs. 3.1.4a), b) and 3.1.4e) and f) there's a small area with highly negative $u$ velocities, while in Figs. 3.1.4c), d) and 3.1.4g) and h) there are two points of inflection of $u$. This kind of behavior is almost impossible on a flat plate and, looking at all the velocity profiles, it can be noticed that profiles with backflow regions and with points of inflection alternate each other every 2 $\xi$ nodes. These last considerations highlight the possibility that this behavior is just an high order numerical instability. To fix it the following correction is applied which acts like a low-pass filter and it doesn't affect the solution accuracy if the $\xi$ stations are close enough each other:

$$x^n = 0.25x^{n-1} + 0.5x^n + 0.25x^{n+1} \qquad 2 < n < N-1, \tag{3.1.1a}$$

$$x_J = -0.25x^{N-2} + 0.5x^{N-1} + 0.75x^N \qquad n = N. \tag{3.1.1b}$$

Where $x$ is one among $f$, $u$ and $v$ and $N$ is the total number of nodes in the streamwise direction. Applying this filtering formulas the new velocity profiles become those shown in Fig. 3.1.5, where both the backflow areas and points of inflection have disappeared. Finally corrected Keller box and analytical boundary-layer characteristic thicknesses are compared in Fig. 3.1.6 and, as it was already predictable looking at the new velocity profiles, the filtering correction doesn't affect the solution accuracy and the two $\delta_1$ still match perfectly each other.

## 3.2 Steady Results

In order to investigate the behavior of Keller box method when pressure gradients occur the simulation of a cambered and thick NLF-0416 airfoil 1 m long with steady flow at zero angle of attack was performed (Figs. 3.2.1 and 3.2.2). The reference temperature and Mach number were 293.15 K and 0.1 respectively and the flow Reynolds number was $4.0 \exp{+06}$ while the transition point was set at $X = 0.1L$, where $X$ denotes the horizontal global Cartesian coordinate, whose origin is set at the profile leading edge. From now on the results of the method developed in this work are compared with those obtained by 2-D CFD simulations carried out with the DLR-TAU code and using the Spalart-Allmaras 1 eq. turbulence model. The mesh was generated by "Pointwise", a commercial CFD mesh generation software, it has 255 nodes over the surface of the NLF-0416 profile and the far field distance is equal to 20 chord lengths. On the other side for the Keller box method $\eta_{max}$ was set at 100, resulting in 74 nodes in wall-normal direction for every $\xi$ node, which means 18870 total grid points.

Fig. 3.2.1 shows a good matching between CFD and Keller box boundary-layer thickness for what concerns the blade suction side, while on the pressure side (Fig. 3.2.2) the two behavior are very different after the first half of chord length.

Both the suction and pressure side CFD results show a peak at the leading edge. Taking a look at the velocity profiles through the boundary-layer close to the stagnation point (such as the one in Fig. 3.2.3) it's clear that the peak is due to a bad interpretation of the boundary-layer by the CFD. The actual boundary-layer in Fig. 3.2.3 in fact ends at the point of inflection at $u \approx 7\,\mathrm{m/s}$ (which is the true external velocity for that node) and its thickness is of the same order of magnitude of the one calculated by the Keller box method, although with the wrong $U$.

In Figs. 3.2.1 and 3.2.2 both boundary-layer thicknesses and the NLF-0416 profile are shown. This is useful to understand the reason of the boundary-layer behavior just looking at the preceding figures, such as positive and negative accelerations due to variations of profile camber line and thickness.

Results show a perfect matching between Keller box method and CFD both on pressure and suction side for laminar flow, and this is confirmed by the laminar velocity profiles shown in Fig. 3.2.4.

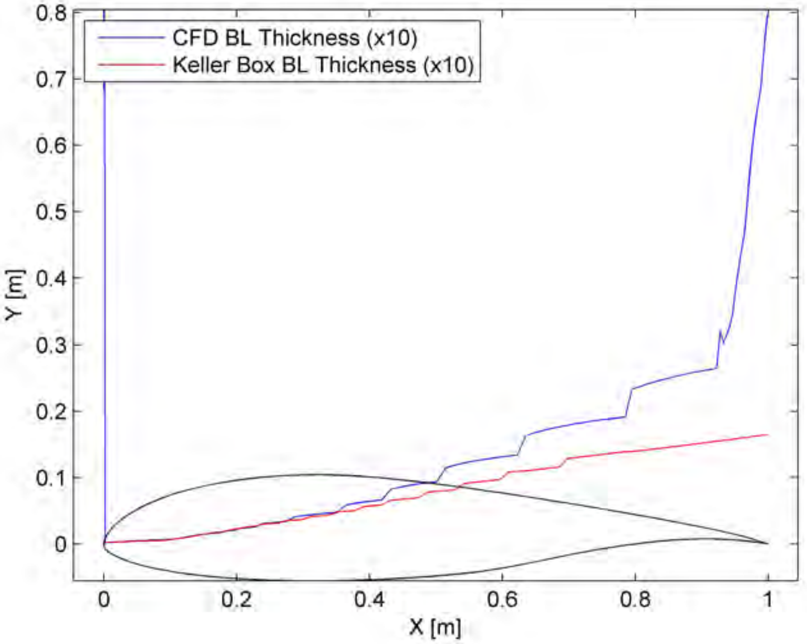

Figure 3.2.1: Comparison between CFD (blue) and Keller box (red) boundary-layer thickness on the suction side of a NLF-0416 profile with $\alpha = 0$

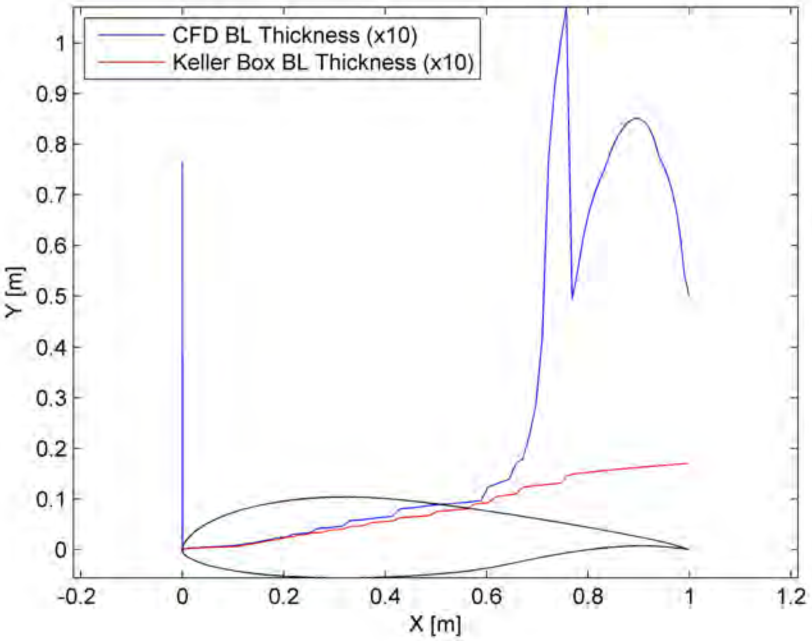

Figure 3.2.2: Comparison between CFD (blue) and Keller box (red) boundary-layer thickness on the pressure side of a NLF-0416 profile with $\alpha = 0$

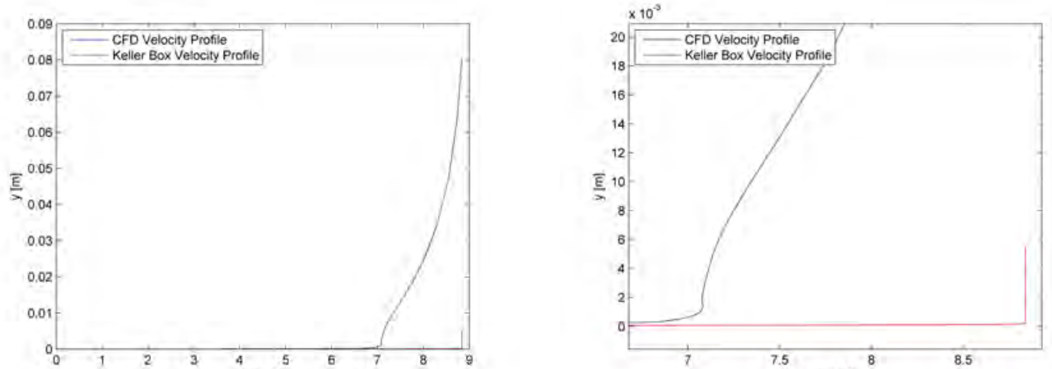

a) b)

Figure 3.2.3: Comparison between velocity profiles obtained by CFD (blue) and Keller box (red) method on the suction side of a NLF-0416 profile at $X = 5.03 \exp -04\,\mathrm{m}$ a) and enlargement of the point of inflection b)

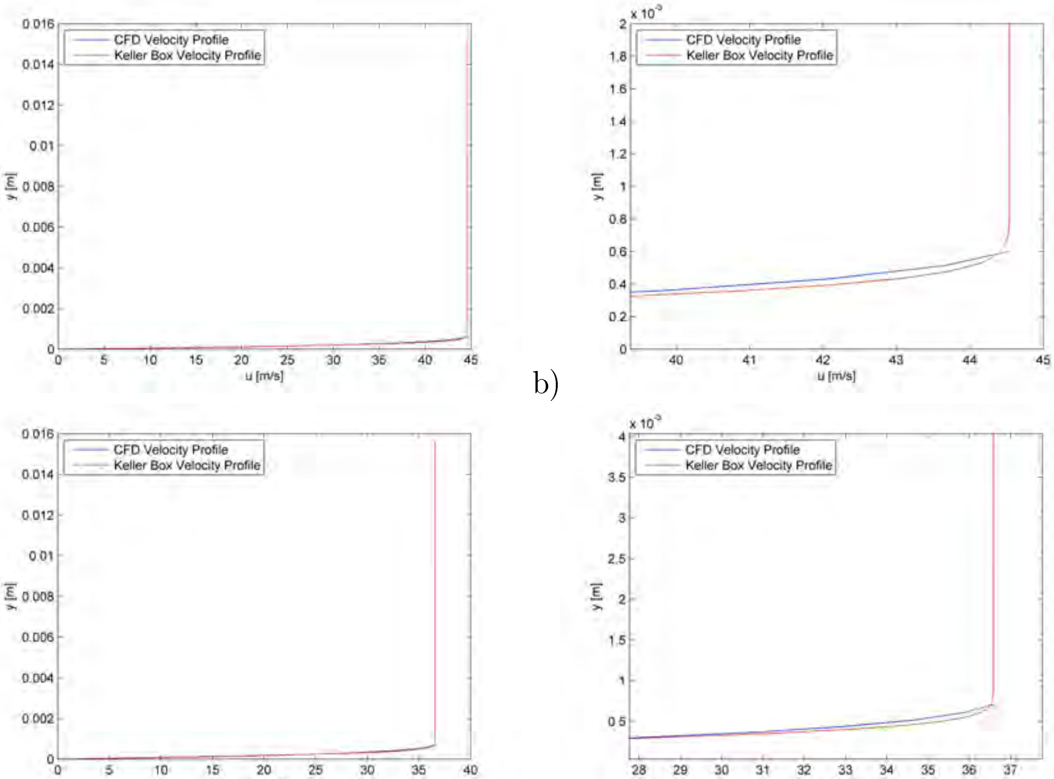

a) b)

c) d)

Figure 3.2.4: Comparison between velocity profiles obtained by CFD (blue) and Keller box (red) method on the suction side of a NLF-0416 profile at $X = 0.0828\,\mathrm{m}$ a) and on the pressure side at $X = 0.0816\,\mathrm{m}$ c) and enlargement of the edge of the boundary-layer b), d)

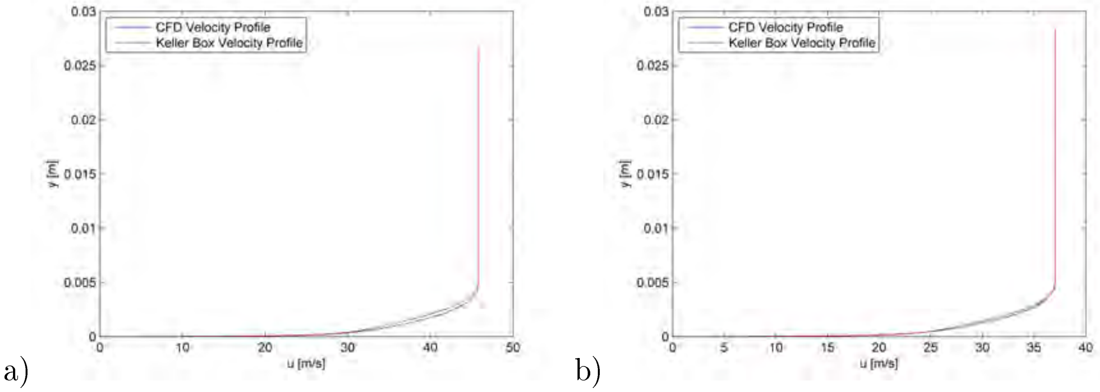

Figure 3.2.5: Comparison between velocity profiles obtained by CFD (blue) and Keller box (red) method on the suction side of a NLF-0416 profile at $X = 0.3118\,\mathrm{m}$ a) and on the pressure side at $X = 0.3031\,\mathrm{m}$ b)

Also after laminar-turbulent transition occurs, boundary-layer thickness calculated by CFD coincides with that obtained using the BL method developed in this work, until maximum profile thickness is reached; again velocity profiles support this statement (Fig. 3.2.5).

In adverse pressure flow conditions (after the maximum profile thickness) results show very different behaviors between suction and pressure side.

On the suction side the boundary-layer thickness shows the same trend as that obtained by the Keller box method and that calculated by CFD. Nonetheless in Fig. 3.2.1 it is possible to notice an increasing gap which spreads even more after $X = 0.9\,\mathrm{m}$. If we have a look at the calculated velocity profiles (Fig. 3.2.6) we see that the reason of the increasing difference of boundary-layer thickness between CFD and the method analysed in this study is the same seen also in section 3.1. Because of the slope of velocity profile through the boundary-layer due to the turbulence model Keller box method reaches the potential velocity value before than the CFD. On the other hand displacement thickness, since it's an integral parameter, will show smaller differences between CFD and Keller box method. Calculating $\delta_1$ for example at $X = 0.9502\,\mathrm{m}$ the results are $\delta_1 = 0.0043\,\mathrm{m}$ for the CFD and $\delta_1 = 0.0036\,\mathrm{m}$ for the method developed in this work, which are really close to each other, especially compared to the boundary-layer thickness whose values, for the same $\xi$ node, are $\delta = 0.037691\,\mathrm{m}$ for the CFD and $\delta = 0.0192\,\mathrm{m}$ for Keller box method. Then, after $X = 0.95\,\mathrm{m}$, the velocity profiles through the BL calculated by the CFD and the method developed in this study start to be completely separated, as can be seen in Fig. 3.2.7, and not even the displacement thicknesses match any more.

For what concerns the pressure side Fig. 3.2.2 shows two peaks of the CFD boundary-

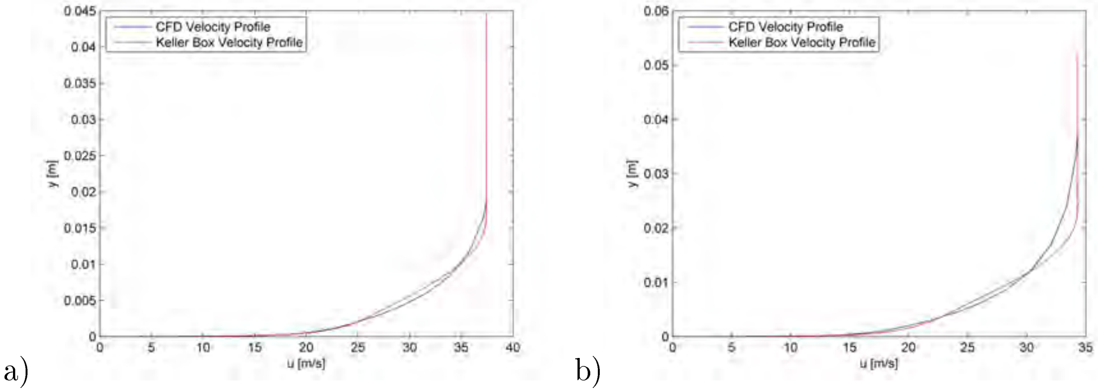

Figure 3.2.6: Comparison between velocity profiles obtained by CFD (blue) and Keller box (red) method on the suction side of a NLF-0416 profile at $X = 0.7538\,\mathrm{m}$ a) and at $X = 0.9502\,\mathrm{m}$ b)

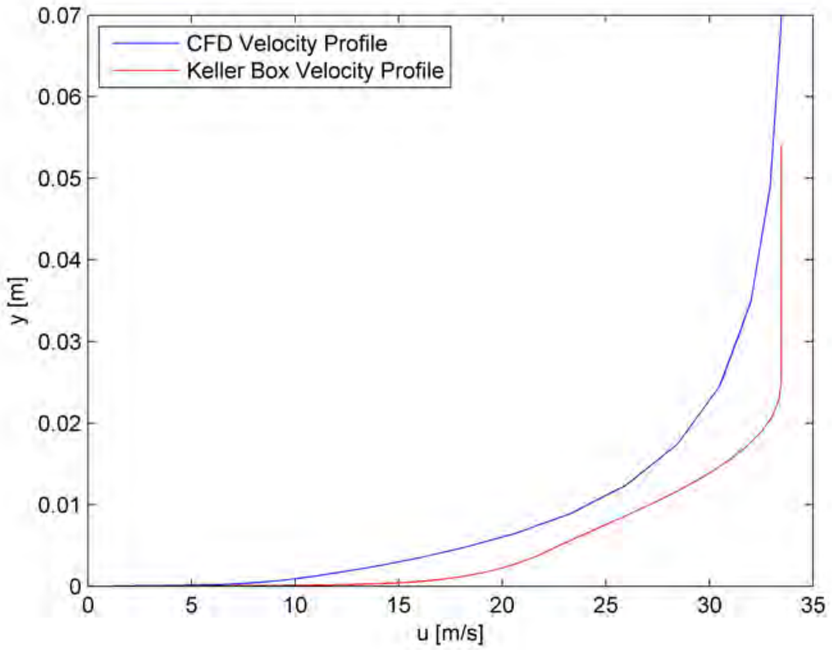

Figure 3.2.7: Comparison between velocity profiles obtained by CFD (blue) and Keller box (red) method on the suction side of a NLF-0416 profile at $X = 0.99\,\mathrm{m}$

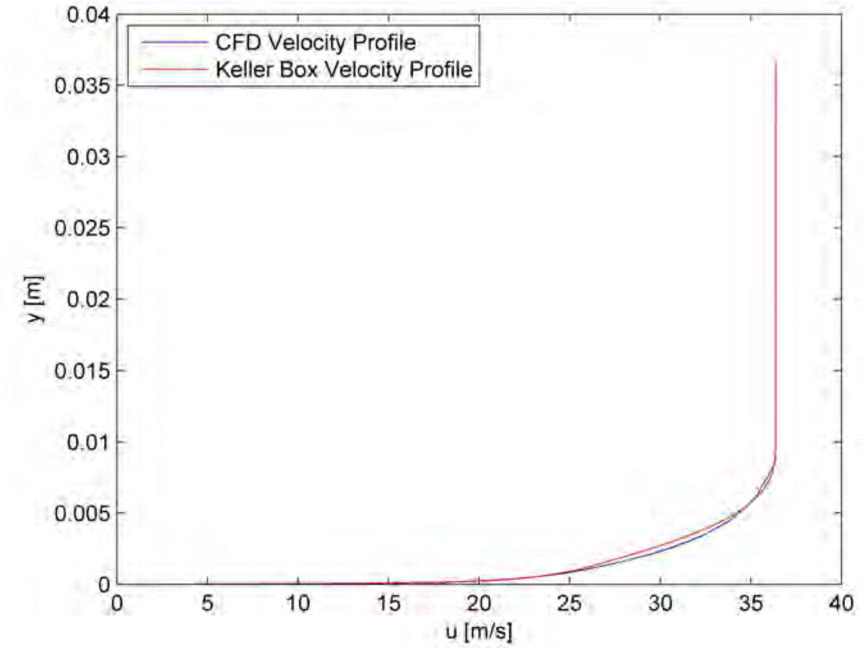

Figure 3.2.8: Comparison between velocity profiles obtained by CFD (blue) and Keller box (red) method on the pressure side of a NLF-0416 profile at $X = 0.5019\,\mathrm{m}$

layer thickness, one at $X \approx 0.7\,\mathrm{m}$ and the second at $X \approx 0.9\,\mathrm{m}$. From the observation of velocity profiles comes out that, after the maximum profile thickness, at first the relative behavior between CFD and Keller box velocities through the boundary-layer is absolutely similar to that already seen on the suction side (Fig 3.2.8). However after $X \approx 0.67\,\mathrm{m}$ the two velocity profiles (CFD and Keller box) completely separate each other and never come close again, as can be observed in Fig. 3.2.9.

Paying attention at Fig. 3.2.9a) it can be observed that after $y \approx 0.03\,\mathrm{m}$ the velocity profile reaches an almost vertical asymptote. This means that, again, the main reason of the difference between CFD and Keller box results on the pressure side after $X \approx 0.7\,\mathrm{m}$ could be a bad interpretation of the boundary-layer by the CFD post-processor. In order to eliminate this CFD boundary-layer thickness peak and those at the leading edge it's necessary to investigate all the badly interpreted velocity profiles and find the actual BL thickness and potential velocity on those points. Then the new $U$ values have to be given as a new input for the Keller box method, a new simulation has to be performed and the results must be compared with the corrected CFD boundary-layer thickness. At the end of this process a good match between results calculated by CFD and by the method described in this study should be achieved, at least until $X \approx 0.8\,\mathrm{m}$.

Figs. 3.2.7 and 3.2.9b), in fact, don't show any vertical asymptote, and the reason

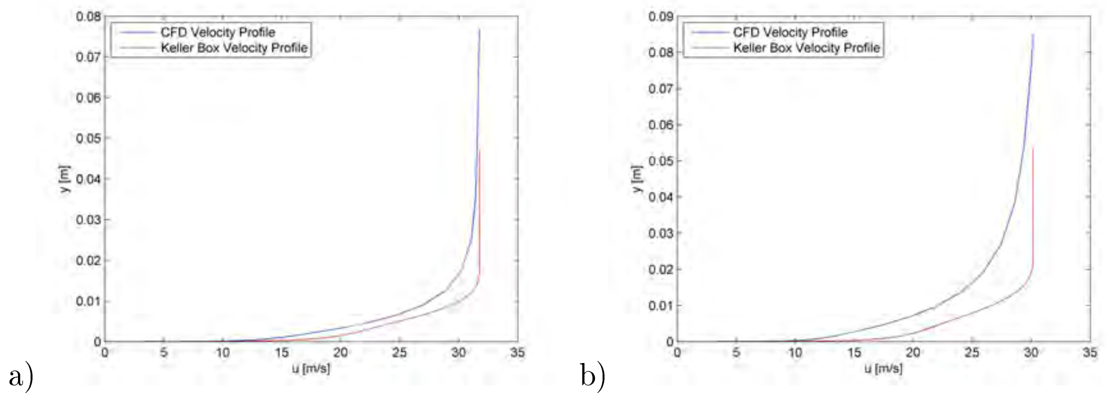

Figure 3.2.9: Comparison between velocity profiles obtained by CFD (blue) and Keller box (red) method on the pressure side of a NLF-0416 profile at $X = 0.7215\,\mathrm{m}$ a) and at $X = 0.8975\,\mathrm{m}$ b)

of this discrepancy between CFD and Keller box boundary-layer thickness could be the presence of the wake, which was not modeled in this work.

## 3.3 Unsteady Results

At last a complete unsteady simulation has been carried out. In this occasion was chosen a symmetrical NACA-0012 airfoil with still 1 m chord length. The flow conditions were the same adopted for the steady simulation described in the previous section, except for the angle of attack $\alpha$, which changes over time as $\alpha = 0° + 2° \sin(\omega t)$, where $k = \frac{\omega L}{U_\infty} = 0.1$. The simulated time interval is $T = 5.4918\,\mathrm{s}$ divided in 8 time steps which are different between upper and lower side of profile and don't have fixed duration. For the CFD simulation turbulence model and mesh generation criteria were the same adopted for the steady test-case, resulting in a pseudo-2D grid which contains 49120 grid points and 24192 hexahedra, with 252 nodes over the profile. The Keller box grid has the same setting of the steady simulation, which means 74 nodes in wall-normal direction at every $\xi$ station and 18648 total grid points.

Fig. 3.3.1 shows the development of both CFD and Keller box boundary-layer thickness (multiplied per 10) over time, together with NACA-0012 blade, for the profile upper side, while Fig. 3.3.2 it's about the lower side.

CFD results show peaks both close to the front stagnation point and after $X \approx 0.8\,\mathrm{m}$ although, looking at Figs. 3.3.1 and 3.3.2, the stagnation point peak is visible only at certain time steps for upper and lower sides. The reason of this behavior lies in the pitching motion performed by the blade, which implies that the stagnation point in

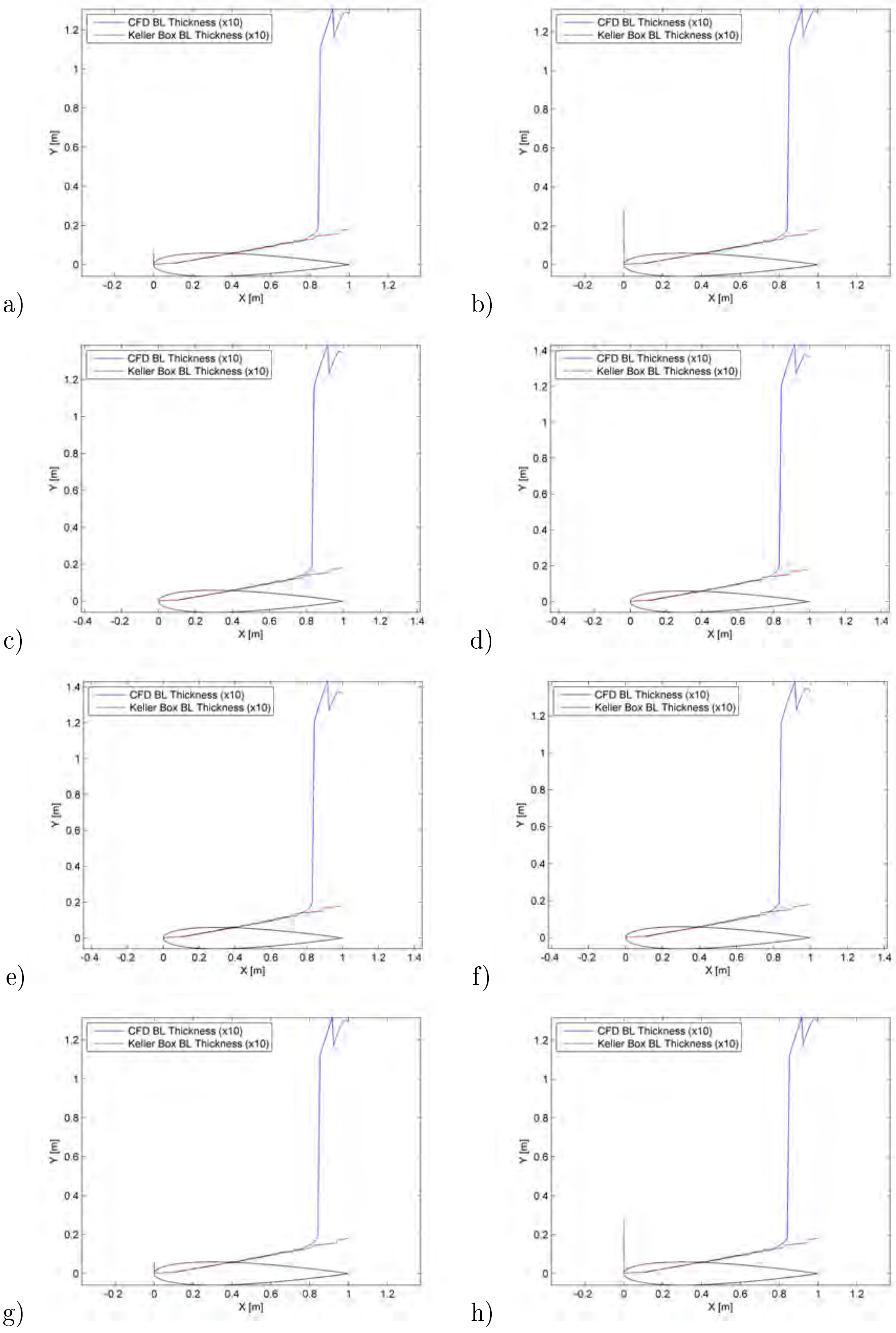

Figure 3.3.1: Comparison between CFD (blue) and Keller box (red) boundary-layer thickness on the upper side of NACA-0012 profile for $t = 0\,\mathrm{s}$ a), $t = 3.6612\,\mathrm{s}$ b), $t = 3.8442\,\mathrm{s}$ c), $t = 4.0273\,\mathrm{s}$ d), $t = 4.2103\,\mathrm{s}$ e), $t = 4.3934\,\mathrm{s}$ f), $t = 4.5765\,\mathrm{s}$ g) and $t = 5.4918\,\mathrm{s}$ h)

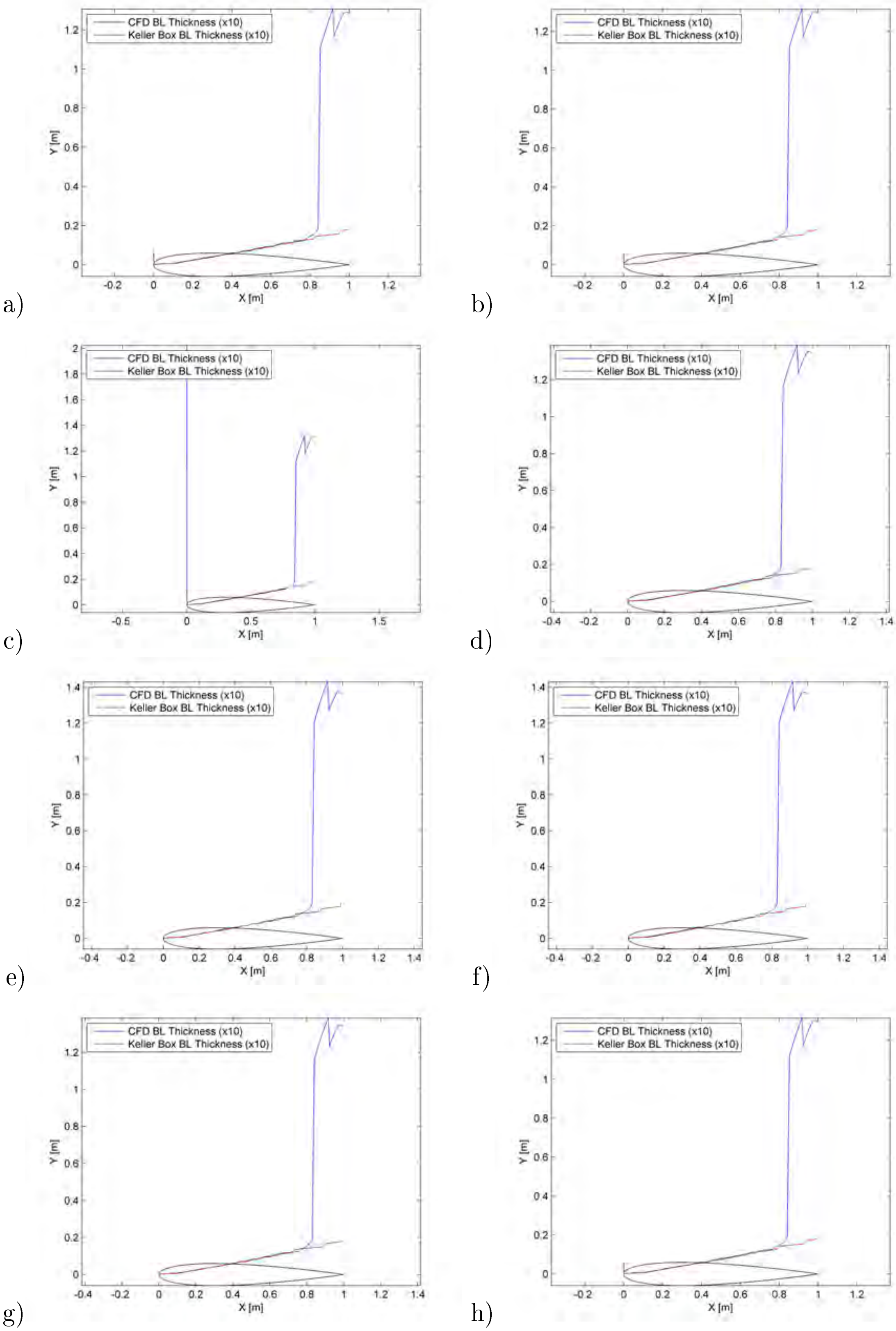

a) b) c) d) e) f) g) h)

Figure 3.3.2: Comparison between CFD (blue) and Keller box (red) boundary-layer thickness on the lower side of NACA-0012 profile for $t = 0\,\mathrm{s}$ a), $t = 3.6612\,\mathrm{s}$ b), $t = 4.5765\,\mathrm{s}$ c), $t = 4.7595\,\mathrm{s}$ d), $t = 4.9426\,\mathrm{s}$ e), $t = 5.1256\,\mathrm{s}$ f), $t = 5.3087\,\mathrm{s}$ g) and $t = 5.4918\,\mathrm{s}$ h)

some cases is located on the upper side and in some other cases is on the lower side. Only when $\alpha \approx 0°$ the front stagnation point coincides with the profile leading edge and there's a peak both on the upper and lower side.

The reason of this peak is, again, a bad interpretation of the boundary-layer by the CFD post-processor. Fig. 3.3.3, for example, shows the velocity profile through the boundary-layer on the upper side of NACA-0012 close to the stagnation point at $t = 3.6612\,\mathrm{s}$. It's easy to notice that the boundary-layer actually ends, as already seen for the NLF-0416, at the point of inflection at $u \approx 1.3\,\mathrm{m/s}$. Again, it's possible to notice that the actual boundary-layer thickness is of the same order of magnitude as the one calculated by Keller box method, although with a wrong external velocity.

After the leading edge Figs. 3.3.1 and 3.3.2 show perfect matching between results obtained by CFD and the method developed in this work, both for upper and lower side, laminar and turbulent flow and at every time step. This last statement has been confirmed by the velocity profiles analysis as shown, for example, in Fig. 3.3.4 for the laminar flow and in Fig. 3.3.5 for the turbulent regime.

After $X \approx 0.8\,\mathrm{m}$ CFD boundary-layer thickness shows an abrupt growth with a peculiar shape, with two maximums, which is almost the same for upper and lower side and constant over time. Looking at velocity profiles through the boundary-layer the reason of this second "double peak" appears to be, again, the wrong interpretation of boundary-layer by the CFD. Looking at Fig. 3.3.6 it's possible to see how velocity reaches a relative maximum at $y \approx 0.02\,\mathrm{m}$, which is the actual end of boundary-layer. After the relative minimum located at $X \approx 0.92\,\mathrm{m}$ $u$ shows a quite different behavior, as can be seen in Fig. 3.3.7, where the velocity through the BL calculated by the CFD reaches an almost vertical slope before the computed boundary-layer thickness. Here the actual BL edge is located where the vertical slope is achieved (in Fig. 3.3.7, for example, at $y \approx 0.04\,\mathrm{m}$).

In order to eliminate CFD boundary-layer thickness peaks the method already described in section 3.2 should be applied. Thus, the badly interpreted velocity profiles should be analysed in order to find the actual BL thickness and potential velocity and perform an updated Keller box simulation. Results of this new simulation should then be compared with the corrected CFD boundary-layer thickness. At the end of this process a perfect match between results calculated by CFD and by the method described in this study should be achieved.

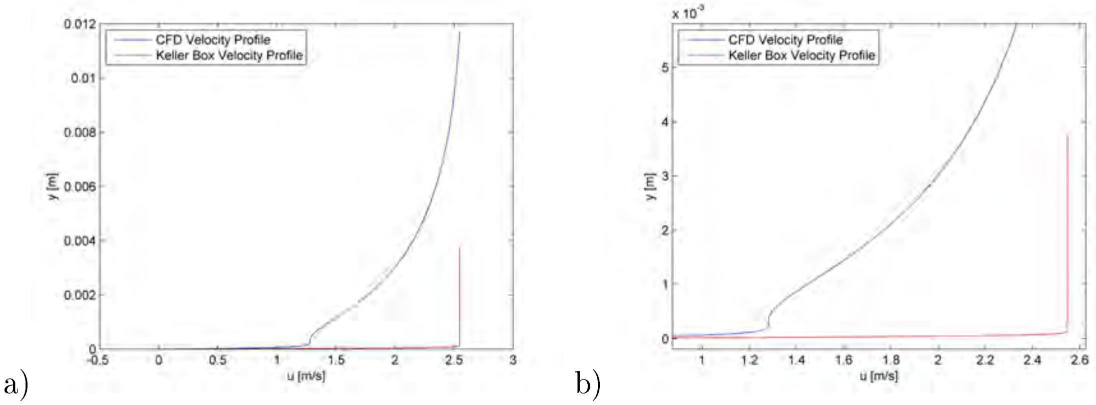

Figure 3.3.3: Comparison between velocity profiles obtained by CFD (blue) and Keller box (red) method on the upper side of NACA-0012 profile at $X = 2.7\exp-05\,\mathrm{m}$ and $t = 3.6612\,\mathrm{s}$ a) and enlargement of the point of inflection b)

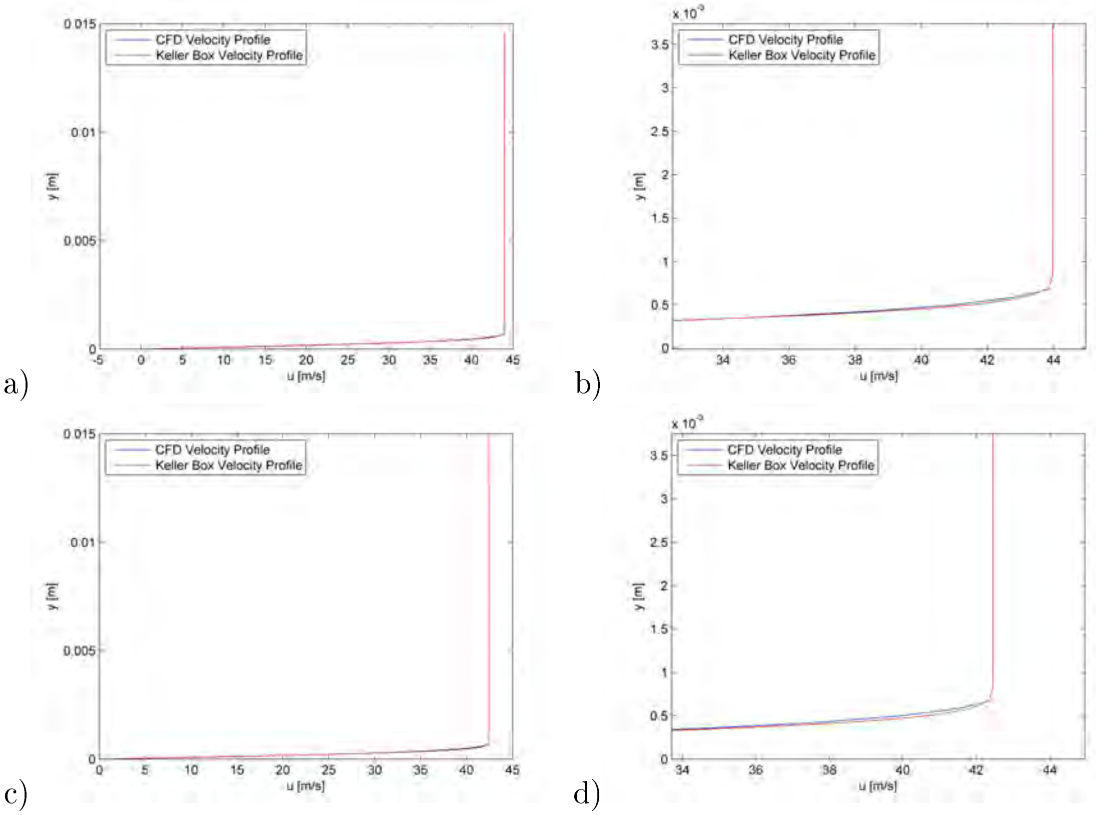

Figure 3.3.4: Comparison between velocity profiles obtained by CFD (blue) and Keller box (red) method at $X = 0.0839\,\mathrm{m}$ on the upper side of NACA-0012 profile at $t = 4.0273\,\mathrm{s}$ a) and on the lower side at $t = 4.7595\,\mathrm{s}$ c) and enlargement of the end of the boundary-layer b), d)

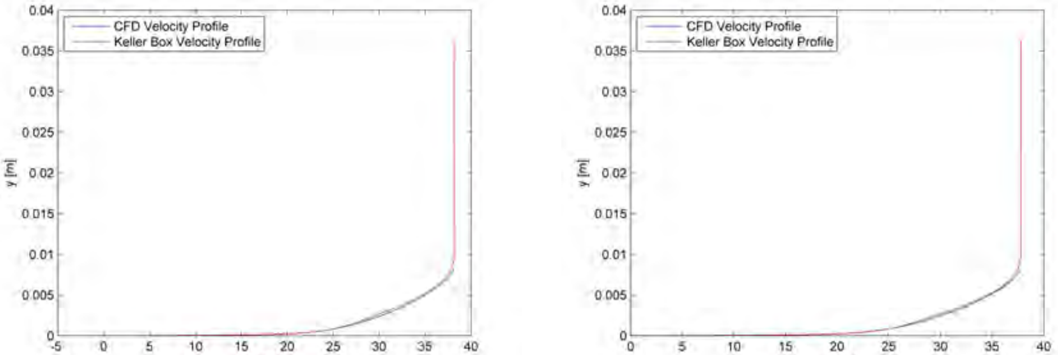

a) b)

Figure 3.3.5: Comparison between velocity profiles obtained by CFD (blue) and Keller box (red) method at $X = 0.5121\,\mathrm{m}$ on the upper side of NACA-0012 profile at $t = 4.0273\,\mathrm{s}$ a) and on the lower side at $t = 4.7595\,\mathrm{s}$ b)

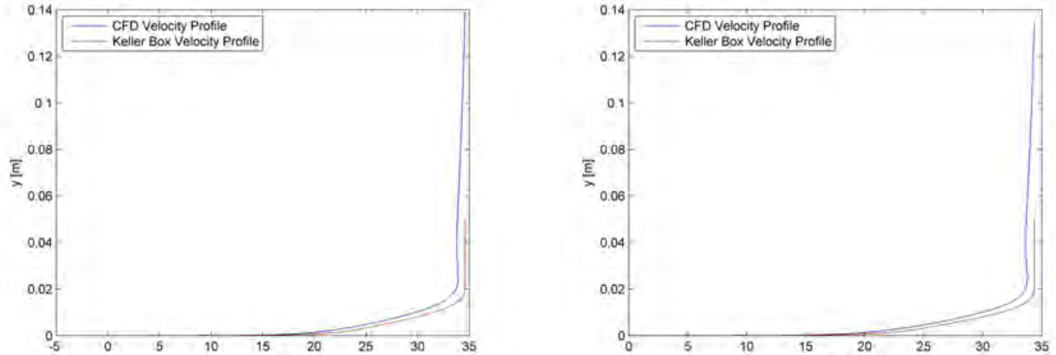

a) b)

Figure 3.3.6: Comparison between velocity profiles obtained by CFD (blue) and Keller box (red) method at $X = 0.9005\,\mathrm{m}$ on the upper side of NACA-0012 profile at $t = 4.0273\,\mathrm{s}$ a) and on the lower side at $t = 4.7595\,\mathrm{s}$ b)

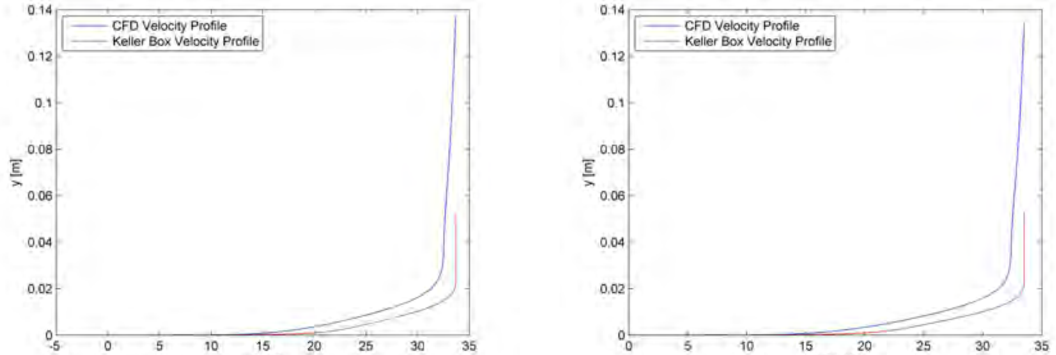

a) b)

Figure 3.3.7: Comparison between velocity profiles obtained by CFD (blue) and Keller box (red) method at $X = 0.9716\,\mathrm{m}$ on the upper side of NACA-0012 profile at $t = 4.0273\,\mathrm{s}$ a) and on the lower side at $t = 4.7595\,\mathrm{s}$ b)

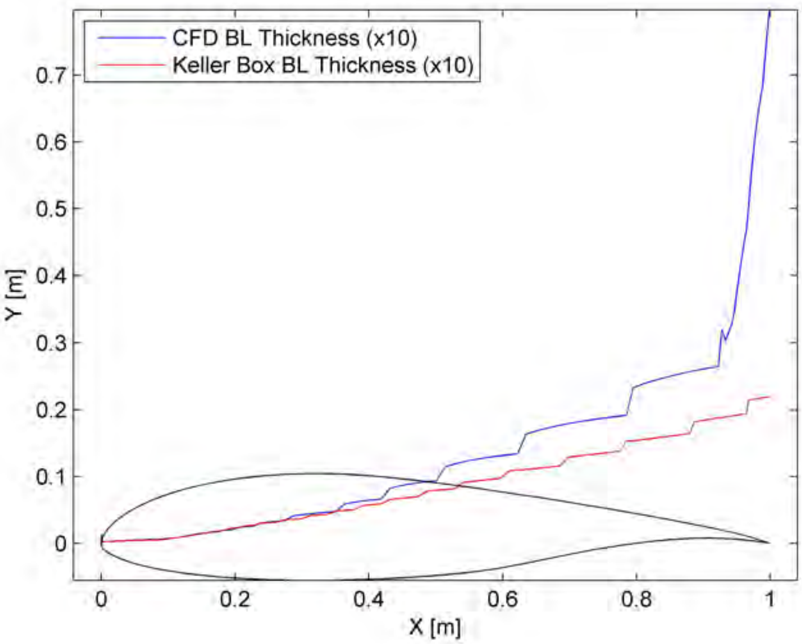

Figure 3.4.1: Comparison between corrected CFD and Keller box boundary-layer thickness on the suction side of a NLF-0416 profile with $\alpha = 0$

## 3.4 Corrected Results

In this section the correction suggested in the two previous paragraphs is applied to the steady simulation of NLF-0416 profile and NACA-0012 at $t = 0\,\mathrm{s}$. The correction wasn't applied to all the unsteady data since the similarities among the boundary-layer distributions of different time steps make it reasonable to think that considerations carried out on steady simulation can be extended to the unsteady case.

In the corrected NLF-0416 results, which are visible in Figs. 3.4.1 - 3.4.2, there isn't any anomaly near the leading edge, and the first peak on the pressure side, located between $X = 0.7\,\mathrm{m}$ and $X = 0.8\,\mathrm{m}$, has been even out.

Although the CFD boundary-layer thickness close to the stagnation point present, after the correction, values which are almost identical to those obtained by the method discussed in this thesis, the analysis of velocity profiles show that perfect match has not been reached yet (Fig. 3.4.3). This last difference, since it occurs only in a very small number of nodes, could be caused by the limited capacity of the CFD to properly simulate the boundary-layer.

On the other hand the pressure side peak of CFD BL thickness located at $X \approx 0.7\,\mathrm{m}$ has been corrected, but still the difference between Keller box results and control data

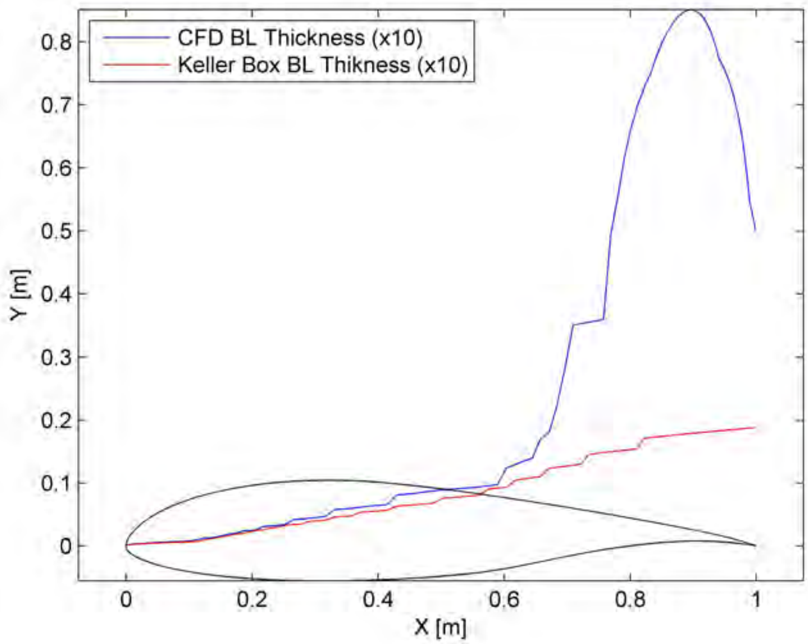

Figure 3.4.2: Comparison between corrected CFD and Keller box boundary-layer thickness on the pressure side of a NLF-0416 profile with $\alpha = 0$

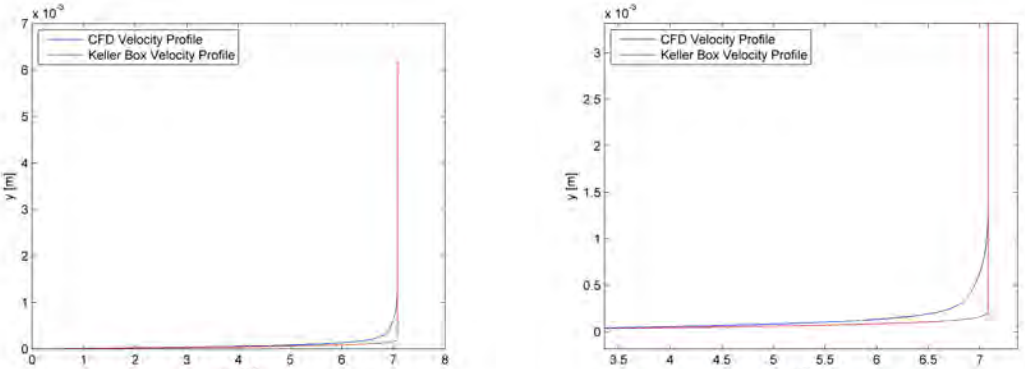

a) b)

Figure 3.4.3: Comparison between velocity profiles obtained by CFD (blue) and Keller box (red) method on the suction side of a NLF-0416 profile at $X = 5.03 \exp -04\,\mathrm{m}$ a) and enlargement of the boundary-layer edge b)

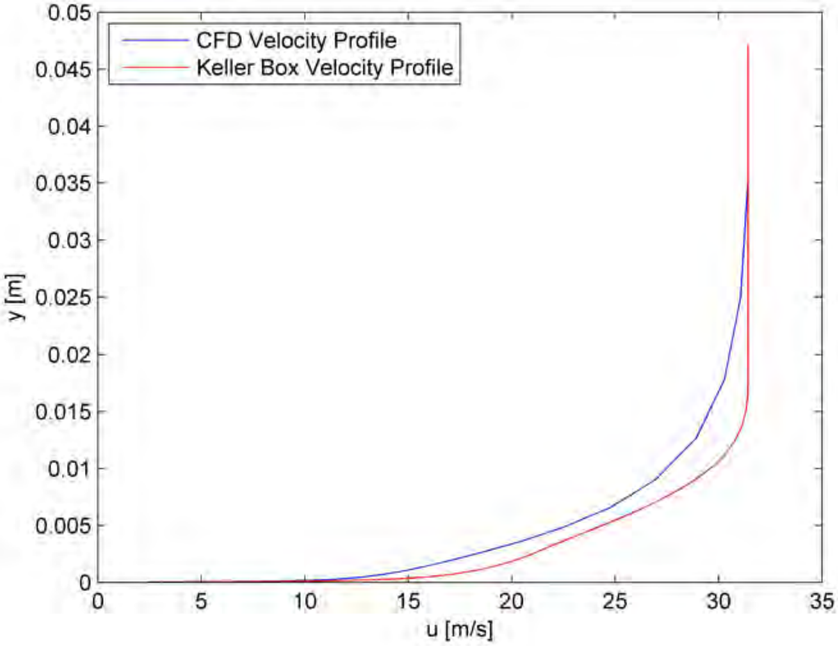

Figure 3.4.4: Comparison between corrected velocity profiles obtained by CFD (blue) and Keller box (red) method on the pressure side of a NLF-0416 profile at $X = 0.7215\,\mathrm{m}$

isn't negligible. The observation of Velocity profiles through the boundary-layer in that region, like the one shown in Fig. 3.4.4, suggests that the reason of this behavior could lay in the Cebeci-Smith turbulence model. This turbulence model indeed is not very suitable for flows with strong adverse pressure gradient[5], like the one which is present in that area.

The non-corrected regions are the last portion of chord length both on suction and pressure side. To better understand the actual situation in Fig. 3.4.5 both the CFD and Keller box boundary-layer thicknesses are plotted perpendicular to the NLF-0416 profile. Looking at Fig. 3.4.5, where the BL thickness is not multiplied by a 10 factor, it can be observed that the differences between CFD results and those obtained by the method discussed in this thesis are very small on the suction side up until the very last part of the profile, while on the pressure side the two patterns spread earlier and the gap between them is way bigger. These discrepancies could actually be caused by the under-capacity of the CFD, as already said, to perfectly simulate the boundary-layer behavior, especially near the trailing edge. This leads to some weird phenomena like the kind of bubble on the suction side in Fig. 3.4.5 where, although, no inverse flow is detected (Fig. 3.2.9), which means that is not a region of separated flow.

Corrected results for the boundary-layer thickness of NACA-0012 steady simulation

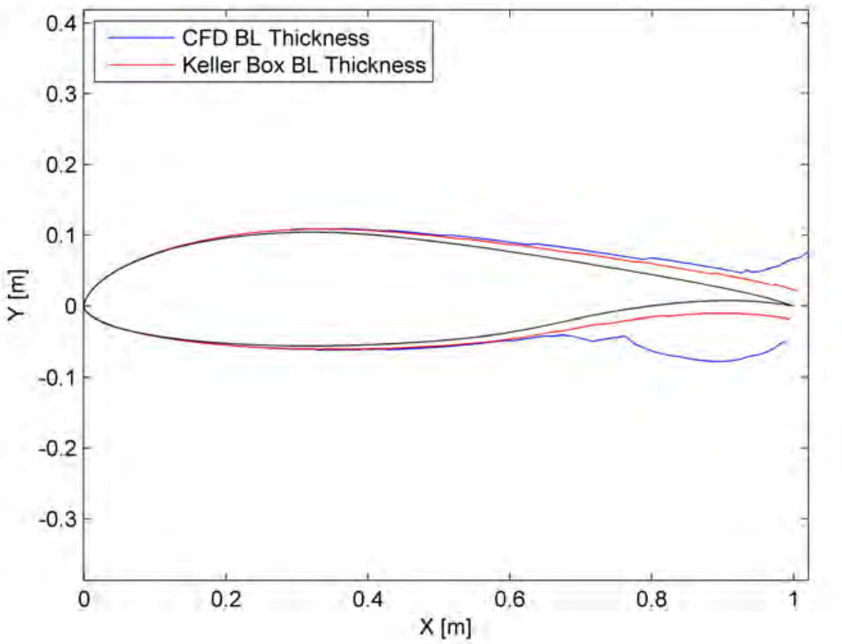

Figure 3.4.5: Actual distribution of corrected CFD (blue) and Keller box (red) boundary-layer thickness over a NLF-0416 profile at $\alpha = 0°$

are shown in Fig. 3.4.6, only one figure is necessary since the profile is symmetrical with no angle of attack, so the BL thickness distributions are identical between upper and lower side. Again, the leading edge peak have disappeared , while near the trailing edge the abrupt growth of boundary-layer thickness has been smoothed out and reduced.

In Fig. 3.4.7 velocity profiles near the leading edge ($X = 2.7 \exp -05\,\mathrm{m}$) resulting from both CFD and Keller box simulation are plotted, with an enlargement of the end of the boundary-layer. It can be noticed that the two profiles match very well each other after the correction.

Also on the last part of chord length we have a way better correspondence between CFD results and those obtained by the method here presented. In particular between $X \approx 0.8\,\mathrm{m}$ and $X \approx 0.9\,\mathrm{m}$ velocity profiles obtained by the two different methods are really similar, as can be seen in Fig. 3.4.8 at $X = 0.9005\,\mathrm{m}$, even though there's already a non-negligible difference in boundary-layer thickness. After $X \approx 0.9\,\mathrm{m}$ the slope of CFD boundary-layer thickness increases. This can be detected also in the velocity profiles calculated by CFD which, in this last region, result to be more separated from those calculated using the numerical procedure described in this thesis. Fig. 3.4.9 shows explicitly what has just been said for the velocity profiles on the upper side at $X = 0.9716\,\mathrm{m}$.

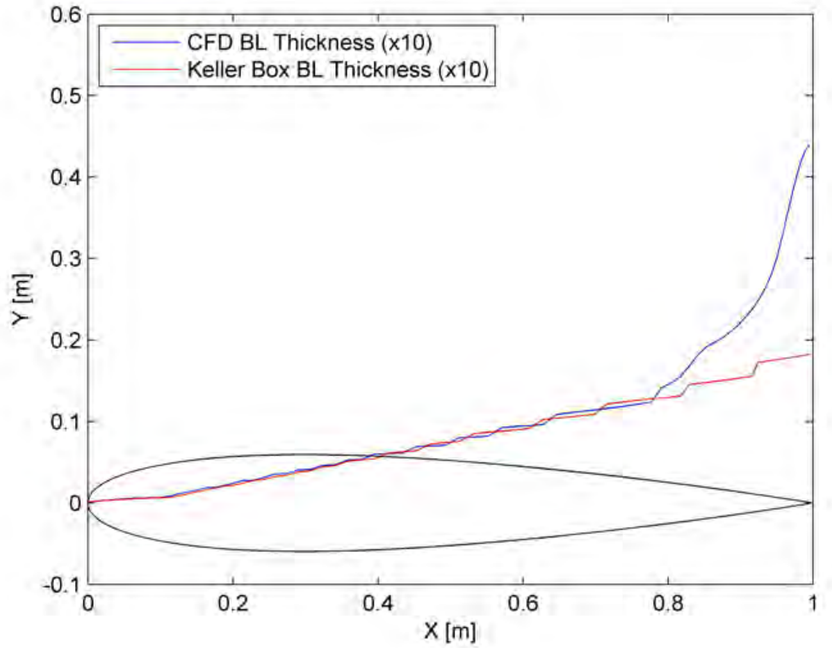

Figure 3.4.6: Comparison between CFD (blue) and Keller box (red) boundary-layer thickness on NACA-0012 profile with $\alpha = 0°$

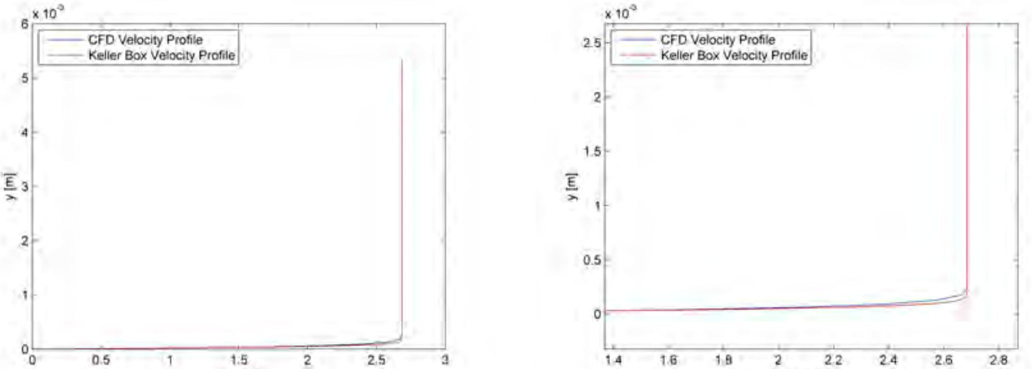

a) b)

Figure 3.4.7: Comparison between velocity profiles obtained by CFD (blue) and Keller box (red) method on the upper side of NACA-0012 profile at $X = 2.7\exp{-05}\,\mathrm{m}$ with $\alpha = 0°$ a) and enlargement of the boundary-layer edge b)

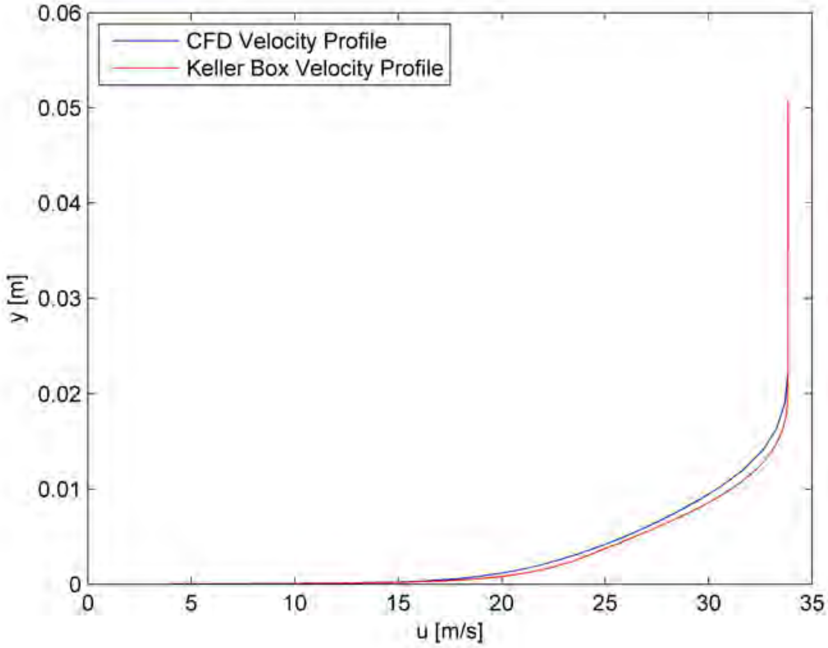

Figure 3.4.8: Comparison between corrected velocity profiles obtained by CFD (blue) and Keller box (red) method on the upper side of a NACA-0012 profile at $X = 0.9005\,\mathrm{m}$

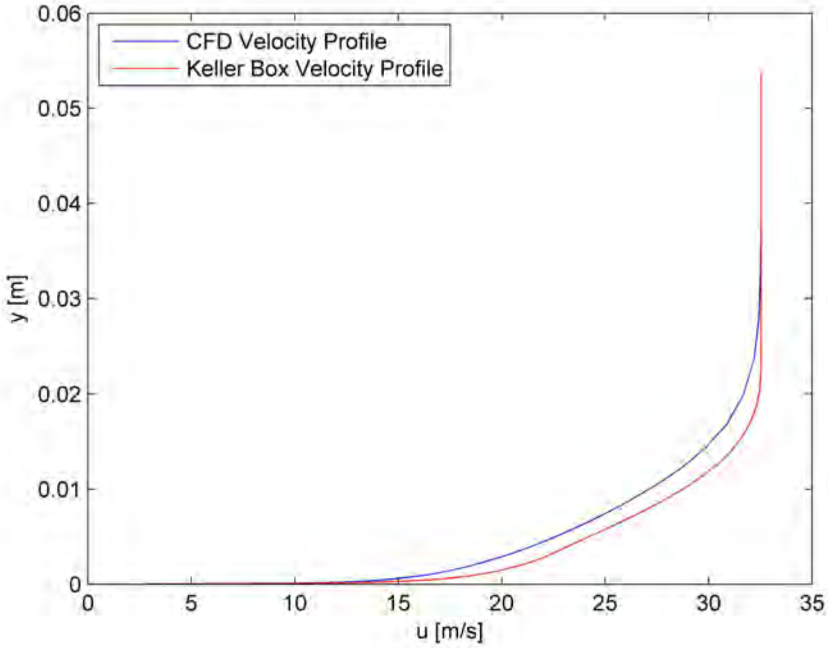

Figure 3.4.9: Comparison between corrected velocity profiles obtained by CFD (blue) and Keller box (red) method on the upper side of a NACA-0012 profile at $X = 0.9716\,\mathrm{m}$

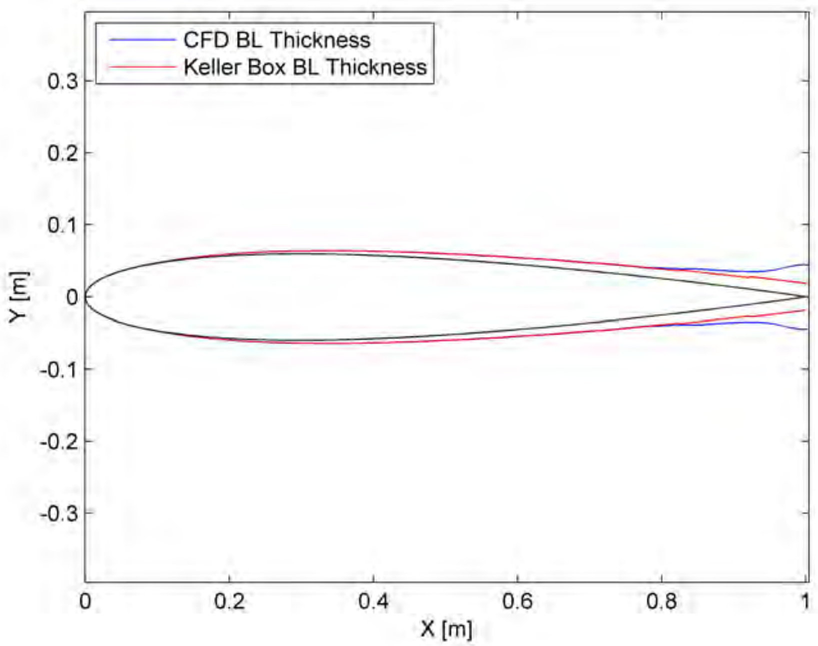

Figure 3.4.10: Actual distribution of corrected CFD (blue) and Keller box (red) boundary-layer thickness over a NACA-0012 profile at $\alpha = 0°$

Again, the actual boundary-layer thickness (not multiplied by 10) is added to the profile in Fig. 3.4.10. Looking at this last figure the hypothesis of a poor capacity of the CFD to model the actual behavior of boundary-layer at the end of the profile in strengthened. Indeed the enlargement of BL thickness shown after $X \approx 0.9\,\mathrm{m}$ it's difficult to explain without separation, which is not the case since, like for the NLF-0416 profile, there isn't any flow reversal.

The only way to understand whether CFD or Keller box results are more accurate is to compare them with experimental evidences. Since boundary-layer thickness affects friction drag, a good solution is to use the large extend of published drag coefficient values, such as those provided by Abbott et al.[8], where drag coefficient $c_d$ is defined by:

$$c_d = \frac{D}{\frac{1}{2}\rho L U_\infty^2}. \tag{3.4.1}$$

Where $D$ is the drag force on the airfoil calculated by integrating $\tau_0$, defined by Eq. (1.1.2), over the profile. Since the position of laminar-turbulent transition plays a key role in drag calculation (section 1.3) it's important to determine where it occurs in real flow. Fortunately transition point location doesn't affect very much the external flow. This means that, for a first comparison, it should be possible to use the old

CFD velocity distribution and perform a Keller box simulation with TP set according to experimental results. According to refs. [9, 10] a good approximation is to set the TP at $X = 0.225L$ which gives $c_d = 0.0059$ while the experimental value is[8] $c_d = 0.006$, showing a perfect match between experimental data and Keller box results. With the laminar-turbulent transition point set at $X = 0.1L$ CFD gives $c_d = 0.0057$ while the result computed by the present method is $c_d = 0.0067$. Considering that the CFD $c_d$ is already lower than the experimental value, and performing a new simulation with TP set further would make the computed drag coefficient decrease, it's clear that the numerical method presented in this thesis gives way better results for the NACA-0012 than a Spalart-Allmaras RANS simulation. The main reason of the difference between CFD and Keller box drag coefficients is the enlargement of CFD boundary-layer thickness, which brings to smaller velocity gradients near the wall and lower shear stress.

For what concerns NLF-0416 profile the real transition point location was found to be[11] $X = 0.39L$ for the upper side and $X = 0.51L$ for the lower side. With this set up the drag coefficient calculated by the method presented here is $c_p = 0.0043$ while the experimental value is[11] $c_p = 0.0056$. This discrepancy could be explained by the under-capacity of the Cebeci-Smith turbulence model to deal with adverse pressure gradients, which are stronger here than on NACA-0012. In fact in this case the accuracy of drag prediction of Keller box method is comparable to the one shown by the CFD, since with TP at $X = 0.1L$ the latter method gives $c_p = 0.0068$ while the result of the former one is $c_p = 0.0069$. Nevertheless, considering the NACA-0012 results, it seems legit to state that the actual behavior of boundary-layer thickness is more similar to the one shown by the Keller box simulations but, on the other side, better results for what concerns drag prediction (which is related to velocity profiles simulation capability) can be achieved by adopting a more sophisticated turbulence model.

What has just been said shows that, for sure, the main reason of the differences between CFD and Keller box BL thickness is the poor capacity of the RANS simulations to properly model the boundary-layer.

# Conclusions and Outlook

In this work a method to solve unsteady boundary-layer equations was developed.

After having introduced the concept of boundary-layer and whose governing equations some simple but reliable boundary-layer analytical models for flat plates were presented.

In Order to solve more complex flow fields it is necessary to solve the direct boundary-layer equations, which are partial differential equations. A finite difference method was developed to solve these equations. At first the Falkner-Skan coordinates transformation was applied. This transformation introduce a variation of dimensionless spacing in wall-normal direction which reduces or even eliminates the transformed boundary-layer growth, allowing us to adopt a rectangular transformed grid and resulting in a numerical advantage. Then a dimensionless stream function $f\left(x,\eta\right)$ was introduced and the boundary-layer momentum equation had to be solved for it. Considering also the dimensionless stream function derivatives, $u$ and $v$, the third order momentum differential equation was reduced to a system of three first order differential equations. The Cebeci-Smith zero equations turbulence model was applied, which is based on empirical functions for inner and outer region of turbulent boundary-layer. This model has the main advantage to not introduce any new equation to the system, and to be thought precisely for boundary-layer determination. A numerical solver was implemented, based on the Keller box discretization, for both steady and unsteady flows. The steady code results were used as starting conditions of the unsteady code in the $(x,y)$ plane. In the $(x,t)$ plane the velocity profile at the previous time step of the $\xi$ node corresponding to the present stagnation point was adopted as starting condition. A good issue for further developments would be to implement a more sophisticated way to model the starting velocity profile, taking into account for example the $\frac{\partial U}{\partial t}$ derivative.

Results for turbulent flat plate showed a small instability in the computation of the first point after the wall in wall-normal direction. This instability was so small that its presence didn't even affect boundary-layer and displacement thickness values, by the way it has been eliminated by a low-pass filtering function.

Steady and unsteady flow with pressure gradients test cases showed very good accordance between CFD results and those obtained by the present method for more than two-thirds of chord length, a part from some very sharp peaks at the leading edge. Then, at different point for different pressure distributions, abrupt changes of CFD computed boundary-layer thickness occurred. Leading edge peaks, those located on the suction side of NLF-0416 and after $X = 0.8\,\mathrm{m}$ of NACA-0012, were all caused by a bad interpretation of the boundary-layer by the CFD post processor. Thus, the velocity profiles through the BL computed by CFD which showed any anomaly in the steady simulation of both NLF-0416 and NACA-0012 were analysed and both the boundary-layer thickness and the external velocity were corrected. Even though the results were corrected in order to find the actual external velocity and BL thickness distribution, there were still non-negligible discrepancies between CFD and Keller box results. In order to understand which one between results obtained by CFD and by the present method are more accurate new Keller box simulations were performed for both NACA-0012 and NLF-0416 setting the laminar-turbulent transition point in accordance with experimental data[9, 10, 11], drag coefficient was calculated and compared with values found in literature[8, 11]. NACA-0012 results show perfect matching between experiments and Keller box numerical data, while CFD drag coefficient for TP at $X = 0.1L$ is way much smaller than the one calculated by the method discussed here. This suggests that the simulations carried out by the method developed in this thesis are more accurate for what concerns behavior of boundary-layer thickness. On the other hand NLF-0416 drag coefficient data showed that, in this case, drag prediction capability of Keller box method is similar to the one achieved by the Spalart-Allmaras CFD simulation, leading to an under-estimation of the drag. This last issue suggests the adoption of a more sophisticated turbulence model than the Cebeci-Smith, which can't simulate properly regions with adverse pressure gradient.

For further developments, after a new turbulence model will be implemented, the new results should be validated by comparison with way more sophisticated (and time consuming) CFD simulations or experimental results for what concerns boundary-layer thickness behavior. Simple Spalart-Allmaras RANS simulations indeed showed to be not enough reliable for validation purposes. The ideal solution would be, of course, to carry out an experimental campaign where both laminar-turbulent transition location and boundary-layer thickness are measured, but this approach would be even more expensive and time consuming than using DNS simulations.

In this work the code needs the information where the turbulence model should be used, which means setting the transition point. In the present calculation the transition point was set manually in accordance to the CFD reference data or experimental results. In order to reduce this arbitrariness, and to refine the method, prediction of transition point should be included and a transition model should be implemented.

The main strength of the boundary-layer method developed in this work is its quickness, coupled with a good reliability. There wasn't any simulation which lasted more than 15/20 seconds, not even the unsteady ones, and they all gave, as already said, results which are better than those obtained by Spalart-Allmaras RANS simulations. On the other hand the main flaw of this method is that it can't handle separated flows, since in these conditions it's no more able to reach convergence. By the way, since the main target of this work was to find a quick method to model attached boundary-layers, its impossibility to deal with separated flows it's not so important. On the contrary, the characteristic of the present method to not achieve convergence after flow separation could be a good way to precisely predict it by detecting where solution is no more reached, new test cases should be carried out to verify this possibility.

Thus, the boundary-layer method here discussed seems to be, if coupled with a good inviscid method, a good starting point for the development of a quick, reliable method useful for preliminary design analysis.

# Nomenclature

| | |
|---|---|
| $\alpha$ | Constant in Cebeci-Smith turbulence model for outer boundary-layer region $\alpha = 0.0168$ in Chapter 1, angle of attack in Chapter 3 and Conclusions and Outlook |
| $\alpha^n$ | Constant of discretized boundary-layer equation |
| $\alpha_1$ | Coefficient for Pohlhausen method in Chapter 1, constant of discretized boundary-layer equation in Chapter 2 |
| $\alpha_2$ | Coefficient for Pohlhausen method in Chapter 1, constant of discretized boundary-layer equation in Chapter 2 |
| $\bar{f}$ | Averaged Falkner-Skan dimensionless stream function in unseady discretized boundary-layer equation |
| $\bar{q}$ | Averaged variable of unsteady boundary-layer equation |
| $\bar{u}$ | Averaged first derivative of Falkner-Skan dimensionless stream function in unseady discretized boundary-layer equation |
| $\bar{v}$ | Averaged second derivative of Falkner-Skan dimensionless stream function in unseady discretized boundary-layer equation |
| $\beta_1$ | Coefficient for Pohlhausen method |
| $\delta f$ | Iterate of Falkner-Skan dimensionless stream funtion |
| $\delta u$ | Iterate of first derivative of Falkner-Skan dimensionless stram function |
| $\delta v$ | Iterate of second derivative of Falkner-Skan dimensionless stream function |
| $\delta$ | Boundary-layer thickness |
| $\delta_1$ | Displacement thickness |
| $\delta_2$ | Momentum thickness |

| | |
|---|---|
| $\delta_{100}$ | Distance in wall-normal direction where velocity parallel to the wall reaches 100% of external velocity |
| $\delta_{99}$ | Distance in wall-normal direction where velocity parallel to the wall reaches 99% of external velocity |
| $\eta$ | Laminar flow wall-normal dimensionless coordinate in section 1.3, Falkner-Skan dimensionless coordinate in wall-normal direction in section 1.5 and Chapters 2 and 3 |
| $\eta_e$ | Falkner-Skan dimensionless wall-normal coordinate value at the edge of boundary-layer |
| $\eta_{max}$ | Maximum value of dimensionless coordinate in wall-normal direction |
| $\gamma$ | Intermittency factor for boundary-layer oute region in Cebeci-Smith turbulence model |
| $\gamma_{tr}$ | Intermittency factor for transition in Cebeci-Smith turbulence model |
| $\Lambda$ | Shape factor for Pohlhausen method |
| $(\nu_t)_i$ | Eddy viscosity of inner boundary-layer region |
| $(\nu_t)_o$ | Eddy viscosity of outer boundary-layer region |
| $(r_j)$ | Coefficient of right-hand side of discretized boundary-layer equation with $j = 1, 2, 3$ |
| $(s_j)$ | Coefficient of discretized boundary-layer equation with $j = 1, 2, 3, 4, 5, 6$ |
| $\mathbf{f}$ | Body forces per volume |
| $\mathbf{v}$ | Velocity vector |
| $\mu$ | Viscosity |
| $\nu$ | Kinetic viscosity |
| $\nu_t$ | Eddy viscosity |
| $\omega$ | Angolar velocity |
| $\overline{u}$ | Mean streamwise velocity component |

| | |
|---|---|
| $\overline{v}$ | Mean wall-normal velocity component |
| $\overrightarrow{\delta}$ | Iterates vector |
| $\overrightarrow{r}$ | Known terms vector |
| $\psi$ | Dimensional stream function |
| $\rho$ | Density |
| $\tau$ | Shear stress in section 1.3, dimensionless time variable in section 1.5 and Chapter 2 |
| $\tau_0$ | Shearing stress due to friction |
| $\widetilde{u}$ | Unsteady mean streamwise velocity component |
| $\widetilde{v}$ | Unsteady mean wall-normal velocity component |
| $\widetilde{z}$ | Width-parallel coordinate |
| $\xi$ | Dimensionless coordinate in streamwise direction |
| $A$ | Constant damping length for Cebeci-Smith turbulence model in Chapter 1, coefficients matrix of Keller box method in Chapter 2 |
| $A_j$ | $3 \times 3$ block matrix of coefficients for boundary-layer calculation with $0 \leq j \leq J$ |
| $b$ | Width of the flat plate in section 1.3, viscous term in transformed boundary-layer momentum equation in section 1.5 and in Chapter 2 |
| $B_j$ | $3 \times 3$ block matrix of coefficients for boundary-layer calculation with $1 \leq j \leq J$ |
| $C$ | Constant in intermittency factor for transition in Cebeci-Smith turbulence model |
| $C_j$ | $3 \times 3$ block matrix of coefficients for boundary-layer calculation with $0 \leq j \leq J-1$ |
| $D$ | Skin friction |
| $f$ | Laminar flow similarity function in section 1.3, Falkner-Skan dimensionless stream function in section 1.5 and Chapters 2 and 3 |
| $FLARE$ | Flügge-Lotz Reyhner approximation parameter |
| $G$ | Constant in intermittency factor for transition in Cebeci-Smith turbulence model |

| | |
|---|---|
| $h$ | Distance between plates of Couette flow |
| $h_1$ | Dimensionless space interval between the wall and the first node in wall-normal direction |
| $h_j$ | Dimensionless space inteval in wall-normal direction with $j = 1, 2, ..., J$ |
| $i$ | Time step |
| $J$ | Total number of grid points in wall-normal direction |
| $j$ | Grid position in wall-normal direction with $j = 0, 1, 2, ..., J$ and $j = 0$ at the wall |
| $K$ | Shape factor for Pohlhausen method in Chapter 1, variable grid parameter in Chapter 2 |
| $k$ | Constant in turbulence viscosity for inner region $k = 0.4$ in Chapter 1, dimensionless reduced frequency in Chapter 3 |
| $k_n$ | Grid spacing in streamwise direction between two grid points at $n$ and $n - 1$ |
| $L$ | Characteristic length in section 1.2, total length in section 1.3, chord length in sections 1.4, 1.5 and Chapters 2 and 3 |
| $l$ | Mixing length |
| $m$ | Dimensionless pressure gradient coefficient in transformed boundary-layer equation |
| $m_3$ | Dimensionless pressure gradient coefficient in transformed boundary-layer equation |
| $N$ | Constant in damping length for Cebeci-Smith turbulence model |
| $n$ | Grid position in streamwise direction |
| $p$ | Pressure |
| $p^+$ | Dimensionless pressure in Cebeci-Smith turbulence model |
| $q$ | General variable of unsteady boundary-layer equation |
| $q_j^{234}$ | Sum of $q_j$ values at three of the four corners of the $\eta_j$ of the box |
| $r$ | Iteration number |

| | |
|---|---|
| $R^{n-1}_{j-\frac{1}{2}}$ | Constant including all terms o previous position in stramwise direction of discretized boundary-layer equation |
| $r_i$ | Dimensionless time interval between $i$ and $i-1$ time steps |
| $Re$ | Reynolds number |
| $Re_L$ | Reynolds number with free-stram velocity $U_\infty$ and chord length $L$ |
| $Re_{x_{tr}}$ | Reynolds number at transition point |
| $T$ | Time averaging interval |
| $t$ | Time coordinate |
| $U$ | Velocity at the boundary-layer edge |
| $u$ | Velocity through the boundary-layer in streamwise direction in Chapters 1 and 3, first derivative of Falkner-Skan dimensionless stream function $f$ in Chapter 2 |
| $u'$ | Turbulent fluctuation of streamwise velocity component |
| $U_\infty$ | Free stream velocity |
| $u_\tau$ | Friction velocity |
| $v$ | Velocity through the boundary-layer in wall-normal direction in Chapter 1, second derivative of Falkner-Skan dimensionless stream function $f$ in Chapter 2 |
| $v'$ | Turbulent fluctuation of wall-normal velocity component |
| $w$ | Dimensionless velocity at boundary-layer edge |
| $X$ | Global horizontal cartesian coordinate |
| $x$ | Streamwise coordinate |
| $x_{tr}$ | Streamwise coordinate where laminar-turbulent transition starts |
| $Y$ | Global vertical cartesian coordinate |
| $y$ | Wall-normal coordinate |
| $y_c$ | Wall-normal distance where the outer region for turbulent viscosity starts |
| BL | Boundary-Layer |

| | |
|---|---|
| CFD | Computational Fluid Dynamics |
| DNS | Direct Numerical Solution |
| RANS | Reynolds Averaged Navier Stokes |
| TP | Transition Point |

# List of Figures

# Bibliography

[1] Schlichting, M., *Boundary-Layer Theory. Seventh Edition.* Tr. by Kestin J., McGraw-Hill Book Company, New York, 1979

[2] Batchelor, G., *Introduction to Fluid Mechanics.* Press Syndicate of the University of Cambridge, Cambridge, 2000

[3] Pohlhausen, K., *Zur näherungsweisen Integration der Differentialgleichung der laminaren Reibungsschicht.* ZAMM 1, pp. 252-268, 1921

[4] Schlichting, M. and Gersten, K., *boundary-layer Theory. 8th Revised and Enlarged Edition.* Tr. by Mayes K., Springer, Berlin, 2000

[5] Cebeci, T., *An Engineering Approach to the Calculation of Aerodynamic Flows.* Horizons Publishing Inc., Long Beach, 1999

[6] Cebeci, T. and Smith, A. M. O., *Analysis of Turbulent boundary-layers.* Academic Press, New York, 1974

[7] Reyhner, T.A. and Flügge-Lotz, I., *The Interaction of a Shock Wave with a Laminar boundary-layer.* Int. J. Non-Linear Mech., Vol. 3, No. 2, pp. 173-199, 1968

[8] Abbott, I. H. and von Doenhoff, A. E., *Theory of Wing Sections. Including a Summary of Airfoil Data.* Dover Publications, Inc., New York, 1959

[9] Silverstein, A. and Becker, J. V., *Determination of Boundary-Layer Transition on Three Symmetrical Airfoils in the N. A. C. A. Full-Scale Wind Tunnel.* NACA Rep No. 637, 1939

[10] Becker, J. V., *Boundary-Layer Transition on the N.A.C.A. 0012 and 23012 Airfoils in the 8-Foot High-Speed Wind Tunnel.* Wartime Report, 1940

[11] Somers, M., *Design and Experimental Results for a Natural-Laminar-Flow Airfoil for General Aviation Applications.* NASA Technical Paper 1861, 1981